TABLE OF CONTENTS

EDITORIAL

The **Laboratory of Ion Beam Physics** (LIP) has now demonstrated that it can successful operate within the framework of its new organizational structure of being directly embedded into ETH. The strong support from the ETH Department of Physics (D-PHYS) and our board of trustees (D-ERDW, Eawag, Empa, PSI) has enabled us to again make significant progress within our fields of research.

Our position as a national and international center for accelerator mass spectrometry (AMS) and for the materials sciences based on ion beam technology has been consolidated. The sophisticated instrumentation is well suited for the mission of the laboratory. A continuous upgrade and modernization program will safeguard those instrumental capabilities. Our focus is to conduct fundamental research in ion beam technologies, instrumental developments and applications of ion beam technologies. In addition, we provide service for external users and contribute significantly to the educational program of ETH.

This annual report summarizes the activities of the past year, both our own and those within the network of external research groups we are collaborating with. It indicates the importance of ion beam technologies for accelerator mass spectrometry as well as for the research activities in the materials sciences. We are very grateful to our partners for their willingness to contribute so strongly to this report.

This is also the place to acknowledge the excellent work of the scientific and the technical staff of the laboratory to the success of the laboratory. In 2010, the equivalent of 24.4 full time positions was filled, which is close to last year's. This shows that our financing model has turned out to be robust and flexible, thanks also to the base funding from D-PHYS and our partners. Last year, on the other hand, we were able to cover 50% of all expenses from funds generated by the activities of our laboratory. The contribution from supplying AMS and detector instrumentation to external collaborators has gained importance for the financing of the technical LIP staff.

We thank all our external partners for their ongoing support. It is our desire to further develop the ion beam technologies and to make possible a more widespread use of these powerful techniques.

Hans-Arno Synal, Peter W. Kubik

THE TANDEM AMS FACILITY

Operation of the 6 MV TANDEM accelerator

SCAN-SIMS application

Accelerator-SIMS for analysis of cosmic dust

OPERATION OF THE 6 MV TANDEM ACCELERATOR

Beam time statistics and future upgrade plans

Scientific and technical staff, Laboratory of Ion Beam Physics

2010 was a year of very efficient operation for the 6 MV EN TANDEM accelerator facility. More than 93% of the 2380 hours of operation were spent on measurements, experiments and beam or equipment tests. Less than 7% were required to maintain or condition the accelerator (Fig. 1). This is due to the nice performance of our last charging belt.

Routine AMS measurements of the two radionuclides ^{10}Be and ^{36}Cl took up about 1500 hours, while the beam time for the material sciences has significantly increased to more than 600 hours (Fig. 2). In particular, measurements to develop the new microprobe system and experiments in connection with the microbeam ion source have contributed to this increase.

Fig. 1: *View of the inside the EN TANDEM accelerator. For maintenance work the terminal shell has been taken off and the potential rings have been moved aside in order to make room for the cleaning of the column.*

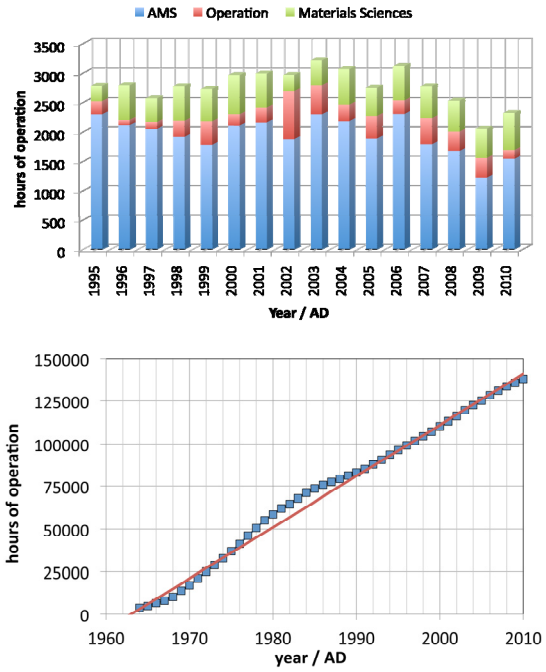

Fig. 2: *Time statistics of the TANDEM accelerator operation subdivided into AMS, materials sciences, service and maintenance activities (above). Total cumulative operation time exceeded 140'000 hours in 2010 (below).*

Preparations for the replacement of the charging system have begun. A Pelletron upgrade kit has been ordered from National Electrostatics Corp., USA in June 2010 with the delivery of the components expected for mid 2011. Major modifications of the accelerator control system will be necessary for the exchange of the charging system. Here, our focus is on developments to enable unattended operation of the accelerator in the future.

It is also planned to install a new MICADAS type ion source at the injector 90° port of the TANDEM. The old Cs gun type sputter source, which had been in operation mainly for the radiocarbon measurements at the Tandem, has already been dismantled.

SCAN-SIMS APPLICATION

A computer program to optimize accelerator settings

S. Bühlmann, R. Pfenninger, D. Güttler

AMS for stable isotopes (SuperSims) covers a wide range of elements. The tuning of each isotopic beam requires an element-specific attentive adjustment of the ion optical components in the beam-line of the TANDEM accelerator. To facilitate the time consuming tuning of electrostatic deflectors (ESA), analyzing magnets and electrostatic lenses and steerers, a computer program (*ScanSims)* was developed. *ScanSims* allows the scanning of parameters like the electrical potential or the magnetic field strength and reads the resulting ion current measured with a pico-amperemeter. This assists the experimenter in finding the optimal settings.

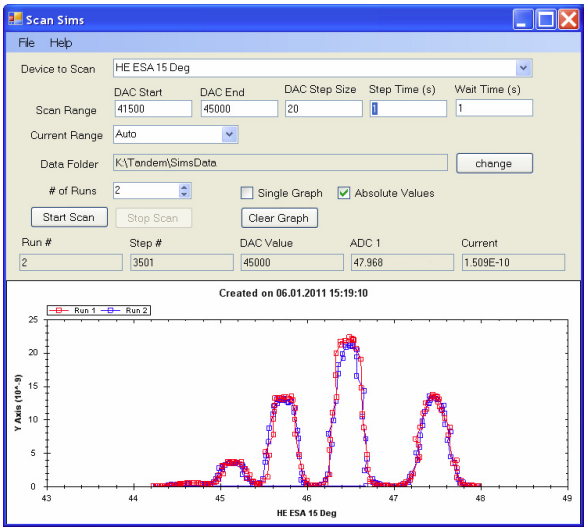

Fig. 1: *ScanSims application showing an ESA scan of a ^{36}Cl beam in different charge states.*

The application has been written for the TANDEM AMS system but can be incorporated into our other accelerator systems as well. It was developed using the Microsoft C# programming language. To communicate with the individual instruments, a TCP/IP link is established to the *Panda* [1] application, which controls all beam-line components.

To start a specific scan, a beam-line component has to be selected from the list and the minimum as well as the maximum DAC value must be specified. Figs. 1 and 2 show some examples of scans performed. For slowly changing components like magnets a waiting time can be specified to start a measurement only after stable conditions have been reached.

One or more runs can be executed within each scan. For each run the ion beam current is shown as a curve in the plot area. To produce those graphics the Open Source library ZedGraph [2] is used.

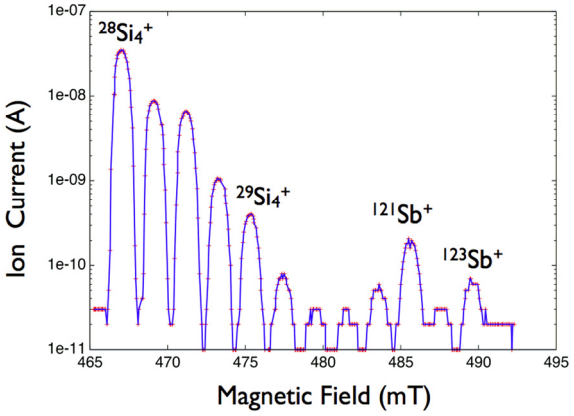

Fig. 2: *Graphical representation of a ScanSims mass scan during a SuperSims measurement.*

The generated graphic can be stored in various image formats. For a detailed analysis of the curves, the graphic can be enlarged or reduced. After each scan, the measured values are automatically exported and saved for further use.

[1] R. Pfenninger and S. Bühlmann, Ion Beam Physics Annual Report (2009) 9
[2] http://www.zedgraph.org

ACCELERATOR-SIMS FOR ANALYSIS OF COSMIC DUST

Measurement of isotopic ratios with a combined SIMS-AMS technique

D. Güttler, C. Vockenhuber, M. Döbeli, H.-A. Synal

Stardust, which is formed in the remnants of star explosions and Supernovae (SN), can be found as microscopic grains in meteorites. These grains survived interstellar travel as well as the formation of our solar system and possess isotopic compositions different from those of the solar system. The investigation of presolar grains can provide information on the pathways of nucleosynthesis in different stars and SN.

Within the framework of the new European program "EuroGENESIS" the Laboratory of Ion Beam Physics is tasked to demonstrate the applicability of Accelerator-SIMS (SIMS = secondary ion mass spectrometry) for isotopic measurements of rare earth and heavier elements (up to uranium) in presolar grains.

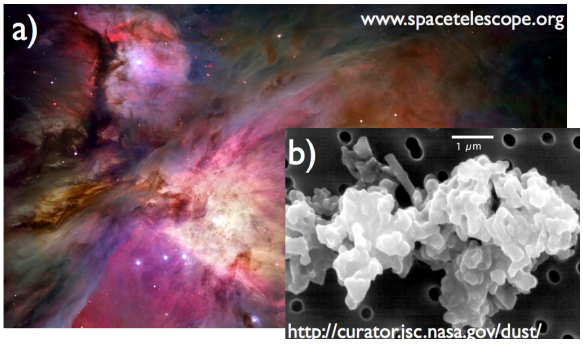

Fig. 1: *a) Star formation in interstellar dust clouds, b) dust particle extracted from a meteorite.*

At ETHZ, a SIMS sputter source is attached to the 6 MV TANDEM accelerator to combine the SIMS and AMS techniques. The mass filtered Cs beam of the SIMS ion gun as well as the clean environment of the SIMS sputter chamber minimizes contamination during analysis allowing the detection of trace elements at the 10^{-12} concentration level.

In 2010, Accelerator-SIMS test experiments have been made for the quasi-simultaneous detection of isotopes in a position sensitive gas ionization detector. Fig. 2a shows the results for an antimony analysis, from which the isotopic ratio $^{121}Sb/^{123}Sb$ can be derived. Furthermore the separation of isobars was successfully tested. As an example of trace analysis the separation of the isobars ^{54}Fe and ^{54}Cr is shown in Fig. 2b.

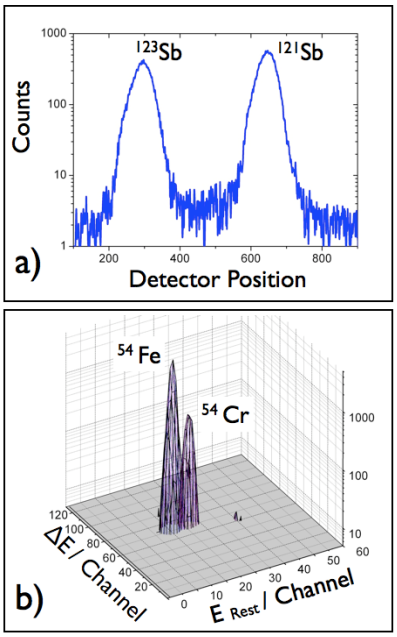

Fig. 2: *a) Position spectrum of ^{121}Sb and ^{123}Sb, b) separation of isobars ^{54}Fe and ^{54}Cr in the gas ionization detector.*

First tests have affirmed our capabilities for Accelerator-SIMS measurements to determine isotopic ratios of trace elements. However, improvements of detection limits and accuracy are still necessary. In particular, analysis of elements >140 amu will require e.g. modifications of the gas ionization detector. As a next step, also sample preparation and analysis of cosmic material will have to be investigated.

THE TANDY AMS FACILITY

Activities on the 0.6 MV TANDY AMS in 2010

Upgrade of the TANDY LE magnet

Comparison of TANDEM and TANDY measurements

AMS of ^{129}I at 300 kV

3+ molecules of actinide hydrides

ACTIVITIES ON THE 0.6 MV TANDY AMS IN 2010

Beam time and sample statistics

Scientific and technical staff, Laboratory of Ion Beam Physics

Over the past years, the 0.6 MV TANDY accelerator mass spectrometer (Fig. 1) has evolved into a robust and flexible device with full multi-isotope capabilities.

Fig. 1: *The compact 0.6 MV TANDY AMS.*

In 2010, the injection system was modified. The low energy magnet was equipped with new coils to increase the bending power, which now allows the measurement of actinides under favorable conditions. To further improve the multi-isotope capability of the setup a new pulsing system (TREK) was installed.

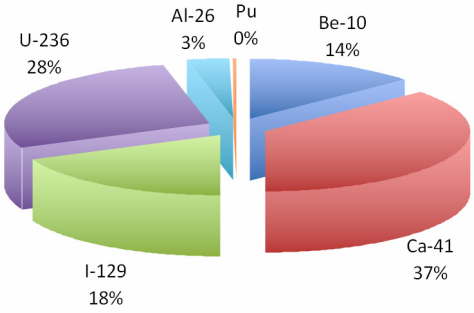

Fig. 2: *Relative distribution of the TANDY operation time based on type of radionuclide (^{10}Be, ^{41}Ca, ^{129}I: routine operation; ^{236}U, ^{26}Al, Pu-isotopes: developments).*

In the past year, the TANDY AMS operated for a total of about 1200 h. More than ⅔ of this time was allocated to routine AMS measurements (^{10}Be, ^{41}Ca, ^{129}I; Fig. 2) and ⅓ of the time was spent to test new instrumentation (e.g. gas detectors) or to develop and establish new radionuclides (^{236}U, ^{26}Al, Pu isotopes; Fig. 2). In that sense the low energy AMS system TANDY has developed from a multi-isotope prototype machine to a flexible device for routine AMS analyses of radionuclides over an exceptionally broad mass range.

More than 1000 samples were measured last year. The routinely measured radionuclides ^{129}I and ^{10}Be account for ⅔ of all samples (Fig. 3) although they use up only ⅓ of the total operation time. For the development of the new nuclide ^{236}U a bit more than ¼ of the total operation time was spent, but only 4% of all samples were ^{236}U samples. This demonstrates that besides being used for routine AMS operation the TANDY still provides enough room for developments. Although we expect that the routine AMS operation will increase in the coming years the TANDY will remain a powerful tool to explore the potential of low-energy AMS in the mass range far beyond ^{14}C.

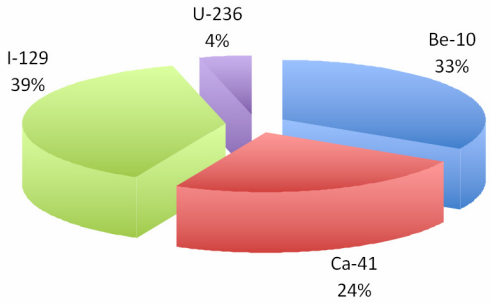

Fig. 3: *Relative distribution of the number of samples measured on the TANDY.*

UPGRADE OF THE TANDY LE-MAGNET

Optimizing the measurement capabilities for the actinides

C. Vockenhuber, M. Christl, J. Lachner, H.-A. Synal, R. Gruber, S. Bühlmann, R. Pfenninger

Measuring actinide ions in charge state 3+ on the high-energy side of the TANDY AMS system requires the magnets to be run close to their maximal field strength and the terminal voltage to be reduced from the usual 500 kV to about 300 kV. Because the masses are even higher at the low-energy (LE) side (e.g. 260 amu for $^{244}Pu^{16}O^-$), the source energy has to be reduced to ~24 keV even for the LE magnet field at its maximum of 680 mT. For optimal focusing into the stripper canal, the source potential should, however, be 1/10 of the terminal voltage.

The old fast-pulsing system allowed keeping the optimal source potential by reducing the energy of the ions in the LE magnetic field. The drawback was that different voltages could only be applied to the pulses A and B (for the abundant isotopes), but not to the baseline, if more than one rare isotope was to be counted.

To be more flexible we replaced the original pulsing system with a TREK 10/40A high voltage amplifier.

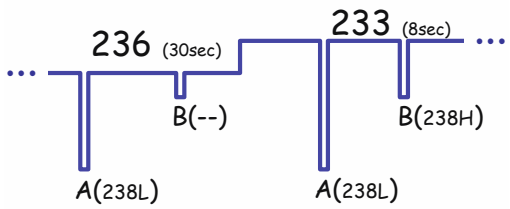

Fig. 1: *Schematic measurement sequence for U; the blue line represents the negative pulsing voltages. Pulses A and B are separated by 60 ms intervals.*

For example, the optimized measurement sequence for uranium ions has the following pulse settings (Fig. 1): (1) reduce the baseline to inject $^{236}U^{16}O^-$ into the accelerator and then measure $^{236}U^{3+}$ during 30 s in the detector, (2) measure $^{238}U^{16}O^-$ during pulse A in the LE cup (238L); no measurement during pulse B, (3) reset baseline to inject $^{233}U^{16}O^-$ (spike) into the accelerator and then measure $^{233}U^{3+}$ during 8 s in the detector, (4) measure $^{238}U^{16}O^-$ during pulse A in the LE Faraday cup, (5) inject $^{238}U^{16}O^-$ during pulse B into the accelerator and then measure $^{238}U^{3+}$ in the HE cup (238H). Settings (1) + (2) and (3) to (5), respectively, can be measured quasi simultaneously. Terminal voltage and the ESA have also to be changed between the settings for mass 236 and mass 233.

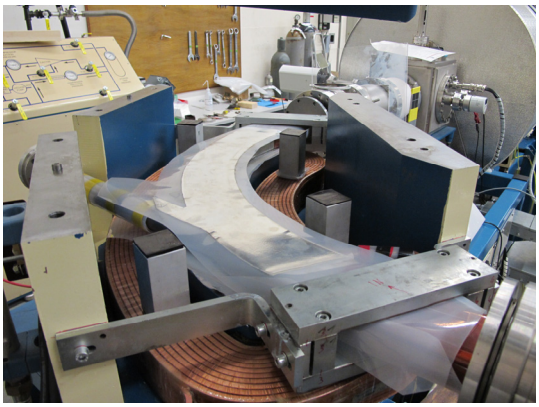

Fig. 2: *Installation of the new LE magnet coils (top yoke removed).*

Last year, the coils of the 20 year old LE magnet started to leak and needed to be replaced. With the new coils, manufactured with 10% more windings, the maximal magnetic field can be increased from 680 mT to 745 mT (Fig. 2). This allows now to bend the actinides at the full source energy needed for optimal transmission.

In addition to the changes made on the LE side, the Faraday cup mounts on the HE side have been simplified for complete positioning flexibility. A cup can now be placed close enough to the center beam line to measure $^{238}U^{3+}$ during the ^{233}U sequence.

These changes allow to measure actinides with minimal dead-time between isotope switching.

COMPARISON OF TANDEM AND TANDY MEASUREMENTS

^{10}Be results from EDML ice samples agree for both AMS systems

F. Steinhilber[1], J. Beer[1], S. Bollhalder[1], I. Brunner[1], M. Christl, P.W. Kubik

Routine ^{10}Be measurements can be made with the TANDY AMS system since the end of 2009. Here we compare ^{10}Be data from the EDML (EPICA, Dronning Maud Land, Antarctica) ice core [1] measured in 2010 using the TANDY with data measured previously using the TANDEM.

After drilling, the EDML ice core was shipped to the Alfred Wegener Institute in Bremerhaven, Germany where it was stored. From there we received thin slices of 1 m length. The ^{10}Be chemical sample preparation was performed at EAWAG in Dübendorf. The slices were first cut into 4 subsamples of 25 cm length and then melted in a microwave oven. ^{9}Be carrier (0.125 mg) was added before standard cation exchange technique was applied to extract beryllium. Sample preparation was the same for both AMS systems except that niobium was added to the BeO material for the TANDY samples and silver in the case of the TANDEM samples.

For this comparison we analyzed samples from two depth regions of the ice core from around 900 m and from about 1100 m depth. Subsamples 1 and 3 (i.e. 0-25 cm and 50-75 cm of the 1 m long ice slice) were measured with the TANDEM. The subsamples 2 and 4 (i.e. 25-50 cm and 75-100 cm) were analyzed with the TANDY (229 samples). ^{10}Be fluxes were calculated from the measured ^{10}Be concentrations using published snow accumulation rates [2].

Both the temporal behavior (Fig. 1) and the distributions of concentration and flux data (Fig. 2) are in good agreement for both AMS systems. The mean values and the variances of concentrations and fluxes are very similar. This agreement is confirmed by statistical tests (Wilcoxon rank sum test to analyze the mean values and the Ansari-Bradley test for the variances). These tests show that the null-hypotheses, namely that the mean values and the variances in the two datasets from TANDY and TANDEM are equal, cannot be rejected at the p=0.05 level. To summarize, the TANDY data is consistent with the data obtained with the TANDEM and has similar analytical errors.

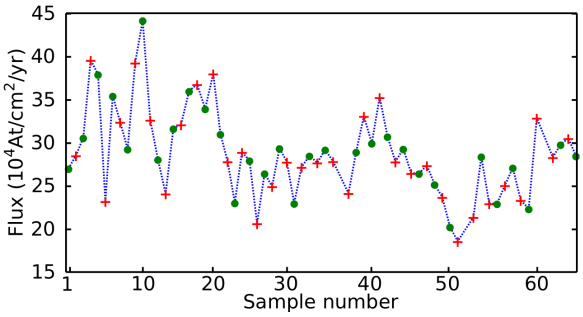

Fig. 1: *Example of agreement of ^{10}Be fluxes of successive samples measured with TANDEM (red crosses) and TANDY (green circles). Shown data are from the depth region around 900 m.*

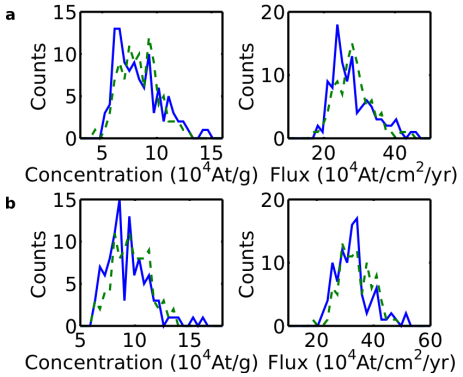

Fig. 2: *Distributions of ^{10}Be concentrations (left) and fluxes (right) measured with TANDEM (blue) and TANDY (green, dashed) for two different depth regions. Around 900 m (**a**), 1100 m (**b**).*

[1] EPICA Community Members, Nature 444 (2006) 195

[2] U. Ruth et al., Climate of the Past 3 (2007) 475

[1] *EAWAG, Dübendorf*

AMS OF ^{129}I AT 300 KV

Efficient detection of ^{129}I in charge state 2+ using He stripping

C. Vockenhuber, V. Alfimov

For the last five years we have routinely measured ^{129}I samples at our TANDY AMS facility using a terminal voltage of 500 kV. Initially charge state 4+ was used, but the measurements suffered from low transmission (about 4%) and interferences from $^{97}Mo^{3+}$ ions. Later we switched to charge state 3+ [1]. Using Ar as a stripper gas the transmission is about 8 %, which is the result of 10% stripping yield for 3+ and about 20 % scattering losses. This setup is adequate for more than 90% of the samples with ^{129}I/I ratios > $1x10^{-13}$. Some samples, however, show high counting rates from surviving molecules in charge state 1+ ($^{27}Al^{16}O^{+}$, same p/q as $^{129}I^{3+}$). Although interferences from p/q ambiguities can be identified in the ionization chamber using a ΔE-E_{res} measurement (Fig. 1a), at high counting rates events from pulse pile-up can mimic ^{129}I events, and at even higher counting rates these events can completely swamp the detector. The intensity of molecules can be reduced by increasing the stripper gas pressure but at the cost of a reduced transmission.

Mean charge states in He as a stripper gas instead of Ar are higher at low energies. This way the I^{3+} yield can be increased while at the same time scattering losses are reduced due to the scattering kinematics involved. The latter advantage allows now to use charge state 2+ which requires higher stripper densities to destroy interfering molecules. On the other hand, p/q interferences are reduced because the 1+ charge state would require a non-integer mass number (129/2 = 64.5). The specifications of the high-energy magnets limit the maximal TANDY terminal voltage for I^{2+} ions to 300 kV.

In a first test we demonstrated successful ^{129}I measurements at 300 kV using a He stripper density of 0.2 µg/cm^2. The transmission is close to 40%. Interfering 2+ molecules are sufficiently destroyed and in contrast to measurements in charge state 3+, no other peaks are visible in the ΔE-E_{res} spectrum, even for samples having exhibited 1+ and 2+ peaks (Fig. 1b). Thus only a simple energy measurement is sufficient for counting ^{129}I provided that a sufficient gas stripper pressure is used.

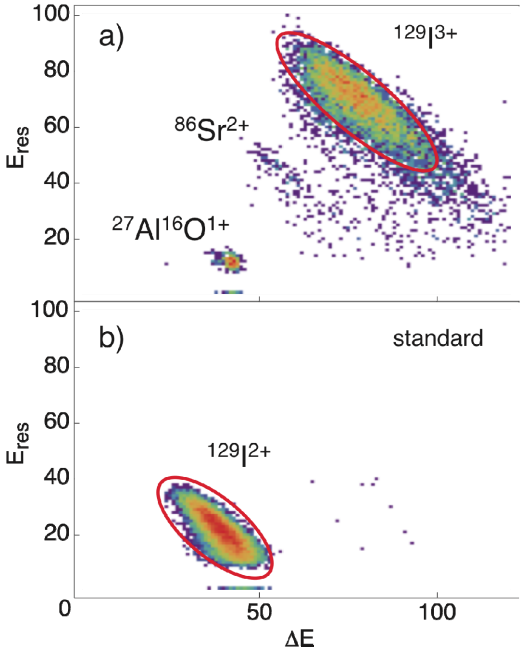

Fig. 1: *ΔE-E_{res} spectrum for a ^{129}I measurement: 3+ at 500 kV (a) and 2+ at 300 kV (b).*

The measured ^{129}I/I background was $1\text{-}2x10^{-13}$, which is slightly higher than previously obtained. This could have been caused by ^{129}I contamination during sample pressing or be due to scattered ^{127}I ions. Note that due to a different ion optical focusing of the 2+ ions, the selecting slits are not at the correct position for the used setup. More systematic background measurements are needed to determine the background level for I^{2+}.

[1] V. Alfimov and H.-A. Synal, Nucl. Instr. & Meth. B 268 (2010) 769

3+ MOLECULES OF ACTINIDE HYDRIDES

First evidence for ThH^{3+} and UH^{3+}

J. Lachner, M. Christl, C. Vockenhuber, H.-A. Synal

The main characteristic feature of an AMS system is its capability to eliminate the interference of atomic and molecular isobars. Molecular isobars can usually be destroyed by selecting ions in charge state 3+ or higher after the stripping process. During measurements of samples containing the abundant isotopes ^{232}Th, ^{235}U and ^{238}U, a stripper pressure dependent counting rate on the next higher mass, i.e. 233, 236 and 239, was observed. This dependence is typical for an incomplete destruction of molecules.

But other stripper pressure dependent processes like enhanced scattering in the stripper tube after the molecule breakup could not be ruled out as a source of such background due to the insufficient energy resolution of a gas ionization chamber at low ion energies. The installation of a time-of-flight detector (TOF) revealed that the scattered ^{235}U or ^{238}U can be efficiently suppressed with narrow slit settings on the high-energy side [1]. With open slit settings, both nuclides could pass through the spectrometer either with the same E/q (ESA) or the same p/q (magnets) as nuclide-236 and were identified with the TOF detector. However, a remaining background was detected that had to be of mass 236. Isobars like ^{236}Np and ^{236}Pu could be ruled out, because the counting rate depended on the stripper pressure. This left undestroyed molecules as the only possible explanation for the origin of the background. As the background occurred one mass unit above the mass of the abundant isotope, hydrogen molecules of Th and U were suspected.

The existence of a molecule $^{232}ThH^{3+}$ could indeed be verified. With the insertion of a thin carbon foil on the high-energy side of the mass spectrometer it was possible to break up the molecule (Fig. 1). The combination of ESA and the second high-energy magnet allowed the identification of the breakup-product ^{232}Th at a lower energy ($E_{break\text{-}up}$=232/233x$E_{molecule}$) and a lower momentum ($p_{break\text{-}up}$=232/233x$p_{molecule}$) corresponding to the fraction expected from the breakup of ^{232}ThH. It also showed the same stripper pressure dependent behavior as the molecular background.

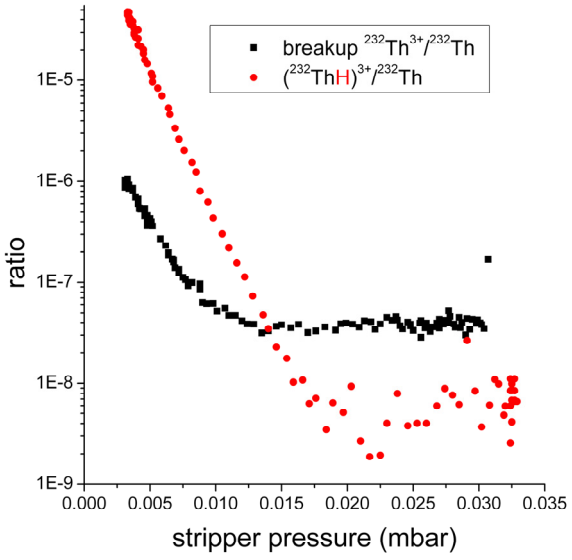

Fig. 1: *Exponential decrease of the counting rate on mass 233 relative to the ^{232}Th current after the first HE magnet as a function of Ar stripper gas pressure. With the inserted foil the background level is shifted upwards due to enhanced scattering. The exponential decrease of ^{232}Th from the breakup is visible only up to a stripper pressure of 0.01 mbar.*

[1] C. Vockenhuber et al., Nucl. Instr. & Meth. B, submitted

THE MICADAS AMS FACILITY

Radiocarbon measurements on MICADAS in 2010

Accomplishing the DatingMICADAS project

Design of the µCADAS system

Laser ablation AMS (LA-AMS)

Molecule suppression in AMS systems

Improving a gas ion source for ^{14}C AMS

RADIOCARBON MEASUREMENTS ON MICADAS IN 2010

Performance and sample statistics

Scientific and technical staff, Laboratory of Ion Beam Physics

In 2009, the MICADAS AMS system was upgraded with a new ion source. In 2010, this ion source has been optimized to take full advantage of the new configuration.

The measurement of solid samples is now routinely performed with ion currents of 40 – 50 µA C^-. This is an increase of 50% from the 30 µA with the old ion source. The new ion source could actually produce much higher currents, but so far we have not utilized this capability for two reasons: (1) the size of the ion beam after the source stays essentially unchanged up to 50 µA, but at higher currents we observe an increase in size resulting in a slightly reduced transmission through the accelerator, (2) the ion source runs more stably over a longer time (presently, an ion source revision is only required every 1 - 2 month).

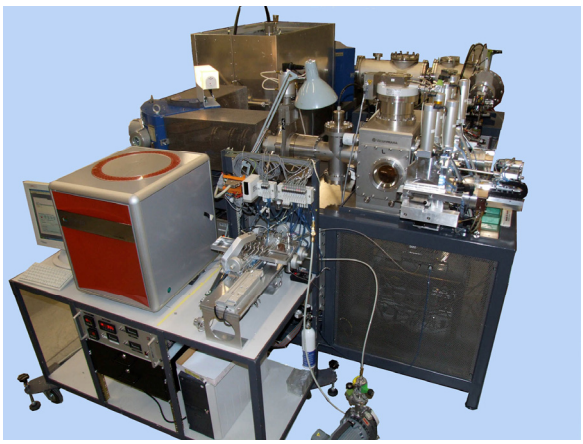

Fig. 1: *The MICADAS ion source with the gas interface and the cracker changer for the measurement of CO_2 in glass ampoules.*

The gas interface at the ion source was supplemented with a cracker changer last year (Fig. 1). It now allows measuring CO_2 gas contained in glass ampoules nearly automated, which reduces the workload significantly as most gas samples are presently contained in such glass ampoules.

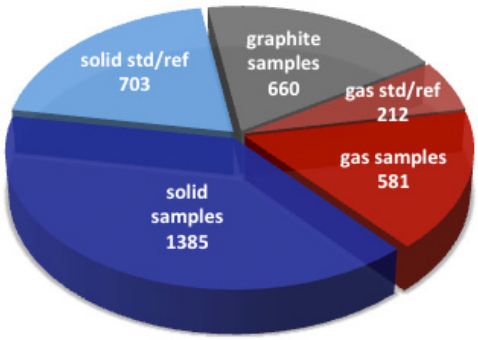

Fig. 2: *Samples and standards measured on the MICADAS prepared at ETH as solid graphite samples (blue) or received as graphite targets (gray). Samples in red were measured with the gas ion source.*

MICADAS was operating on 239 days last year with 2'819 hours (32 % of the year) spent on measuring samples. We have measured in total more than 3500 samples and standards (Fig. 2). While the number of in-house prepared samples increased by about 20 %, the number of measured gas samples and the graphite samples prepared externally nearly doubled.

The strong increase in the number of samples to be measured will require at higher ion current in the future. We therefore plan to test and improve the ion source so that it can run stably and reliably at somewhat higher currents from solid targets. The goal is to double the number of measured solid targets per day with sample cassette changes still being made only during regular working hours. This requires only a moderate increase of C^- current to 60 – 70 µA for 3 ‰ precision on modern samples which is standard in our laboratory.

ACCOMPLISHING THE DatingMICADAS PROJECT

Setting up the system at Klaus-Tschira-Laboratory, Mannheim

S. Bühlmann, R. Gruber, A. Herrmann, R. Pfenninger, C. Vockenhuber, S. Lindauer[1], B. Kromer[1]

The DatingMICADAS system was developed for the "Curt-Engelhorn-Zentrum für Archäometrie" in Mannheim (Germany). Due to delays during the construction of the building in Mannheim the system was hosted at ETHZ from spring 2009 until May 2010. It was fully integrated into the research and measurement program of our laboratory where it was routinely used for routine dating measurements and for experiments to further improve the AMS measurements technique. In particular, molecule dissociation cross-sections in a He stripper gas were investigated (see “Design of the µcadas system” in this report). For these tests, the system was partially reconfigured to match the requirements of the ion transport at energies below 150 keV.

Fig. 1: *Shipping of the DatingMICADAS components to the Reiss-Engelhorn-Museum on May 11, 2010.*

In early May 2010, the system was disassembled and packed into crates and boxes for shipment (Fig.1). The equipment arrived in Mannheim and LIP staff members began to install the instrument on May 17. Within one week the system was completely reassembled and first beam tests were performed (Fig. 2).

Fig. 2: *The DatingMICADAS system at its final destination at the Klaus-Tschira-Laboratory.*

Specification test were successfully completed and the new instrument was handed over to the Klaus-Tschira-Laboratory in June 2010. The system is now in routine operation and serves as a high performance radiocarbon dating instrument.

The fast and efficient commissioning of the system at its final location shows the robustness of the design concept. Having major components such as ion source, acceleration section, and high-energy mass spectrometer on separate support frames, which can be shipped as preassembled units, makes the realignment procedure of the instrument fairly easy. With power supplies, system control computer, and diagnostic instruments integrated into the three major support frames, only minimal effort is required to make the system operational again. In addition, it turned out to be relatively easy to reproduce the performance specifications reached at ETH during factory acceptance test.

[1] *Heidelberg Academy of Sciences, University of Heidelberg, Germany*

DESIGN OF THE µCADAS SYSTEM

Experimental setup for an acceleratorless "AMS"

M. Seiler, A. Herrmann, H.-A. Synal

Experiments have shown that both suppression of molecular isobars and high ion transmission can be achieved by using helium stripping [1]. To further investigate this technique of low energy AMS a new instrument was set up.

The ion source and the first magnetic filter element are the same as for a MICADAS type system. The main difference is the replacement of the high voltage section of the accelerator by a gas stripper on ground potential. Without the focusing effect of the accelerator the focal point of the ion beams moves closer to the magnet. The gas stripper is the same as the MICADAS stripper but it can be installed without electrical insulation. The stripper tube is placed such that the focal points of both mass spectrometers come to lie in the middle of the tube. The spectrometer after the stripper consists of a 90° magnet followed by a 90° electrostatic analyzer (ESA). As the beam energy is the same before and after the stripper, similar magnets can be used on both sides. The radii of the ESA and the magnets are 250 mm. The ion optics of these elements leads to a design more compact than that of the MICADAS (Fig. 1).

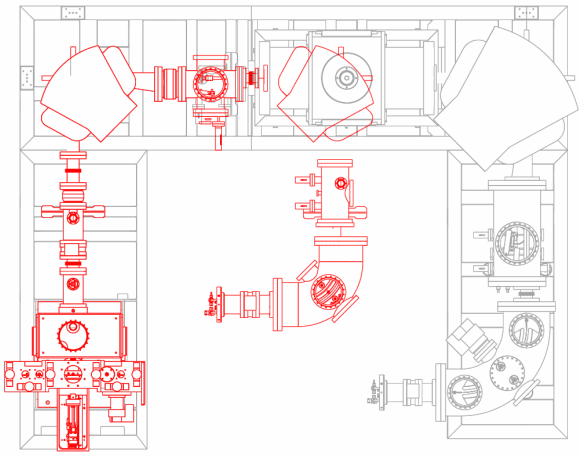

Fig. 1: *Schematic view of the µCADAS design (red) overlaid on that of the MICADAS (gray).*

The stable isotope beam currents are measured with Faraday cups before (^{12}C) and after the stripper (^{12}C and ^{13}C). An electron multiplier tube (EMT) is used to count ^{14}C events. Although the EMT has a dark count rate it was chosen because its multiplication effect is necessary to detect the low energy ions used in this system.

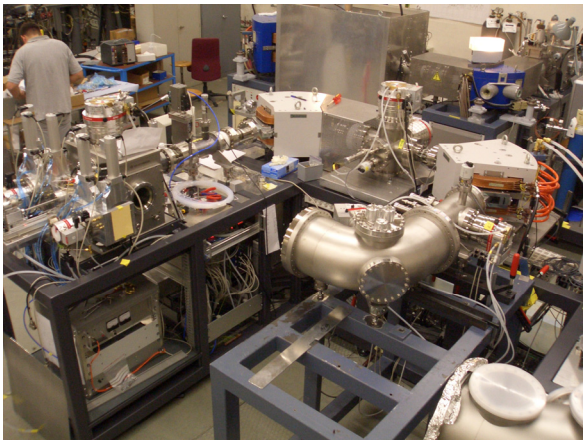

Fig. 2: *Picture of the µCADAS setup while under construction.*

The µCADAS system is planned as a temporary modification before the final construction of the EnvironMICADAS system. Due to the similarity of the two systems, the MICADAS power supply and measurement control systems can be used with only minor adaptations. The ion source and the first magnet are set up in the configuration of the EnvironMICADAS. The support for the gas stripper and the second magnet are temporarily modified while the beam line after the second magnet is placed on an additional frame. The system was completed in November 2010 and can be operated for about two months.

[1] T. Schulze-König et al., Nucl. Instr. & Meth. B 269 (2011) 34

LASER ABLATION AMS (LA-AMS)

First direct coupling of a laser ablation cell to an AMS

L. Wacker, B. Hattendorf[1], M. Christl, D. Günther[1], H.-A. Synal

A laser ablation system was used for the first time to produce CO_2 from a carbonate sample and inject it directly and continuously into a gas ion source of an AMS system. Solid carbonates like stalagmites or corals are suitable materials because they can be ablated and decomposed continuously while still meeting the requirements for long-lasting and stable measurement conditions.

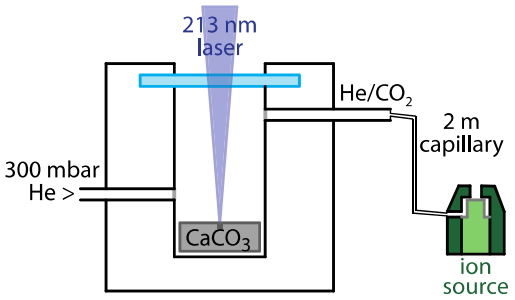

Fig. 1: *Sketch of the experimental setup.*

The setup consisted of a commercial laser ablation unit (LSX 213, CETAC Technologies, Omaha, USA) equipped with a specially designed laser ablation cell (Figs. 1 and 2). CO_2 formed during the ablation process was directly and continually flushed with He into the gas ion source of the MICADAS AMS system. The high energy density of the focused laser beam (up to 15 J/cm^2) allows ablation of practically any solid material with a lateral resolution of 150 µm or less. The production rate of CO_2 was adjusted by varying the laser frequency (1-20 Hz), the crater diameter (1-150 µm) and the energy (0.2-3 mJ/pulse) of the pulsed laser (frequency quintupled Nd:YAG with 5 ns pulse duration). The laser settings were optimized with stalagmite material (Tab. 1).

The maximal CO_2 production rate was estimated from the pressure buildup in the ablation cell assuming any produced gas is CO_2. Using this value, a maximum CO_2 yield of >70 % was calculated, significantly more than observed in a previous study [1]. The high C^- current observed from the ion source further supports a high CO_2 yield of more than 50 %.

Laser		Measurement	
Wavelength	213 nm	Ablated $CaCO_3$	24 µg/min
Frequency	20 Hz	Ablated carbon	2 µg C/min
Energy	2.7 mJ/pulse	Produced CO_2	1.5 µg C/min
Lateral res.	150 µm	C^- current	9 µA
Feed motion	2 µm/s	Total eff. C^-	3.4 %

Tab. 1: *Optimized laser settings (left); corresponding ablation rates, CO_2 production, C^- current and efficiency (right).*

The analysis of a >300 kyr old stalagmite sample indicated a contamination with 5 % of modern carbon. A stalagmite of known age (28.7 ± 0.2 pMC) was well replicated with 28.36 ± 0.76 pMC. These initial results show that LA-AMS is a promising new tool to allow direct radiocarbon analysis of corals and stalagmites at unprecedented high resolution.

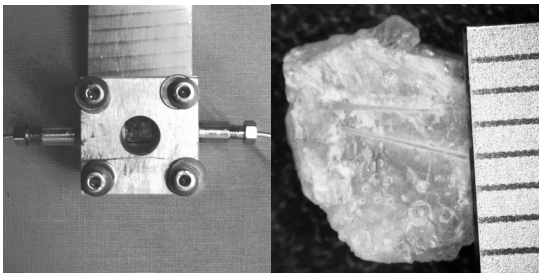

Fig. 2: *Ablation cell (left) and stalagmite with 150 µm laser tracks (right).*

[1] B.E. Rosenheim et al., Rapid Commun. Mass Spectrom. 22 (2008) 3443

[1] *Inorganic Chemistry, ETHZ*

MOLECULE SUPPRESSION IN AMS SYSTEMS

Survival rate measurement with varying stripper gas pressure

M. Seiler, T. Schulze-König, H.-A. Synal

The suppression of isobaric molecules is a key property for radiocarbon mass spectrometry. In compact AMS instruments, where ions in charge state 1+ are analyzed, this suppression is due to multiple collisions with the stripper gas.

Measurements to further analyze this process were made with the DatingMICADAS. The areal density of the stripper gas was varied by changing the stripper gas inlet pressure. Calibration was by measurement of the beam energy loss at different stripper densities via the changing terminal voltage. The areal density was then calculated using stopping power values from the literature. The molecule survival rate falls off exponentially with increasing areal density of the stripper medium which allows the definition of a cross section for the destruction process (Fig. 1).

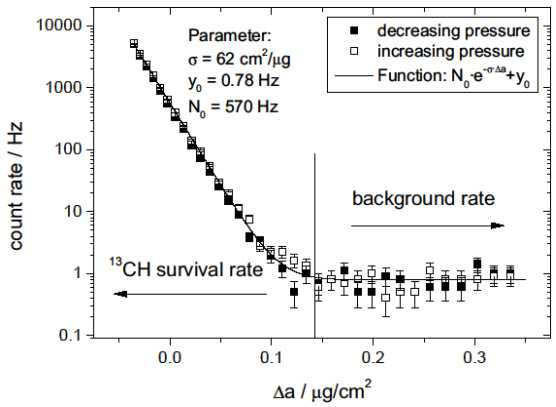

Fig. 1: *Measured count rate for surviving ^{13}CH molecules as function of the stripper gas areal density [1].*

In order to distinguish between ^{13}CH and $^{12}CH_2$ a carbon foil with an areal density of 3 µg/cm^2 was placed in front of the electrostatic analyzer (ESA) at the HE side. In this foil the surviving molecules from the stripper are destroyed. The ESA was then used to separate the carbon fragments of the molecules ^{13}CH and $^{12}CH_2$ based on their energy. These measurements were made for several beam energies between 80 and 240 keV and nitrogen as stripper gas (Fig. 2). Beside nitrogen, the regular stripper gas of the MICADAS type systems, measurements were also made with helium in the energy range of 80-140 keV (Fig. 2). The comparatively low breakthrough voltage of helium prohibited measurements at higher energies to avoid damaging the instrument. The results indicate no energy dependency within the measured energy range for helium, while there is evidence for a lower cross section in nitrogen stripping at energies below 100 keV. Given the average cross sections, an areal density of about 1.4 µg/cm^2 nitrogen is needed to suppress molecules by a factor of 10^{12} needed for radiocarbon dating. For helium, this areal density is only 0.4 µg/cm^2 which reduces beam losses due to angular straggling, an advantage when measuring at low energies.

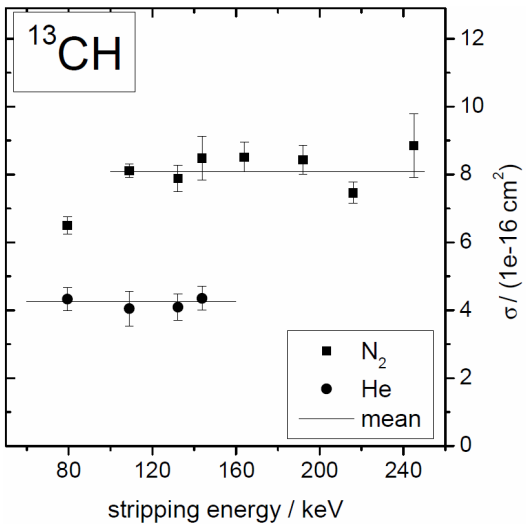

Fig. 2: *Measured destruction cross sections for ^{13}CH molecules [1].*

[1] T. Schulze-König et al., Nucl. Instr. & Meth. B 269 (2011) 34

IMPROVING A GAS ION SOURCE FOR ^{14}C AMS

Towards higher precision and faster analysis of small samples

S. Fahrni[1], L. Wacker, H.-A. Synal, S. Szidat[1]

Generally, sample sizes in ^{14}C AMS range from a few milligrams down to about 100 µg of carbon. The vast majority of samples are converted to graphite as this material offers high negative ion yields and high currents [1]. In the graphitization of small (<100 µg) and especially of ultra-small (<10 µg) samples, however, problems arise due to the increasing influence of contaminations and unreliable outcomes of the graphitization reaction [2].

In order to circumvent the graphitization of samples in this range, Ruff et al. set up a CO_2 feeding system for the AMS facility MICADAS [3]. Measurements with gaseous samples of 2 to 50 µg C were made and many users have measured their samples with this gas handling system. The relatively low ionization yield and the resulting low negative ion currents, however, limited the quality of the measurements in comparison to graphitized samples. With a new ion source installed at MICADAS, tests were conducted in order to improve the performance of gas measurements.

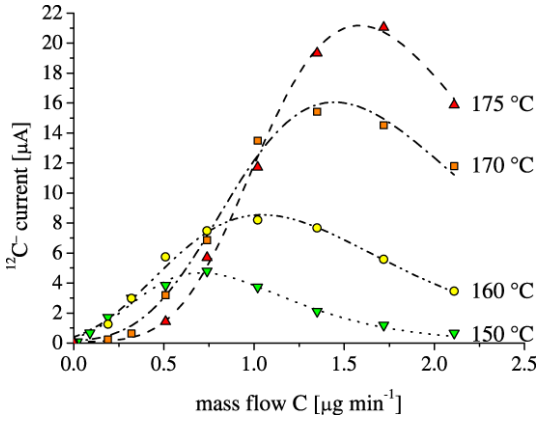

Fig. 1: *Ion currents as functions of carbon mass flow rate and Cs reservoir temperature.*

C$^-$ currents could be boosted from initially 3 µA to up to 12-15 µA for average samples. Fig. 1 shows that higher C$^-$ currents and thus faster measurements depend, as expected, on the temperature of the cesium reservoir, which is a proxy for the Cs beam intensity deposited onto the target. Average ionization yields for gas samples could be increased by a factor of 2 and are now in the range of 8% for average samples. This results in twice the sample throughput compared to before. An example for the time flow of a single radiocarbon measurement with the old and the new ion source is illustrated in Fig. 2.

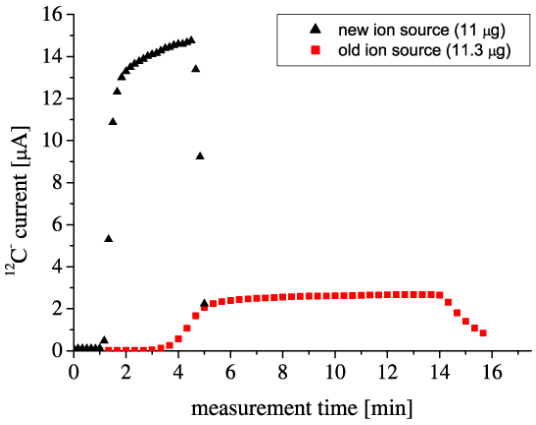

Fig. 2: *^{12}C$^-$ time flow of a measurement before (red squares) and after the improvements (black triangles).*

The higher negative ion yields and the increased mass feeding rates allow now radiocarbon AMS measurements down to 5 ‰ counting statistics within only 30 minutes and without the time-consuming graphitization process.

[1] J. Southon and G.M. Santos, Nucl. Instr. & Meth. B 259 (2007) 88
[2] R. Drosg et al., Nucl. Instr. & Meth. B 259 (2007) 340
[3] M. Ruff et al., Radiocarbon 49 (2007) 307

[1] *Chemistry and Biochemistry, University of Bern*

DETECTION AND ANALYSIS

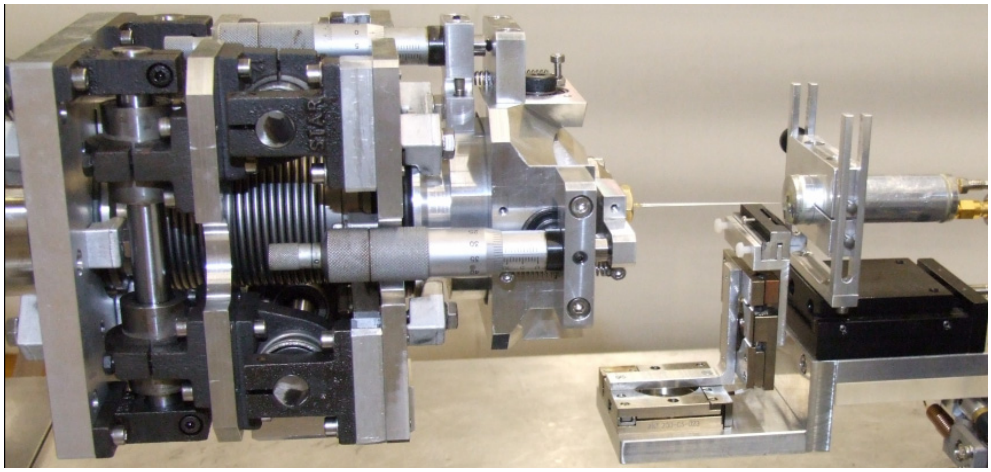

Improvements of the measurement software

Microprobe scan control unit

Miniature gas ionization chambers: Round II

A new compact backscattering gas detector

Detettore POMODORO

A new 2D sensitive detector setup for ^{36}Cl

Detection limit of ^{236}U at TANDY

Chlorine-36 interlaboratory comparison

IMPROVEMENTS OF THE MEASUREMENT SORTWARE

A new database server, remote control of *squirrel* and a new web server

R. Pfenninger, S. Bühlmann

The numerical data collected with the data acquisition programs *hamster* (TANDEM) and *squirrel* (TANDY, MICADAS) are stored in databases. The TANDY and MICADAS data have been transferred from our Oracle database to a MySQL database hosted by D-PHYS of ETHZ. Our Oracle database is now used only for the TANDEM data.

The data acquisition program *squirrel* was upgraded with a TCP server. It is now possible for the LabView program of the gas ion source to manage the data acquisition program. The following commands are implemented:

Command	Function
start	start the next run
start(<position>)	change sample to <position> and start the next run
stopafcyc	stop run after the current cycle
stop	stop run immediately
getstatus	get status of measurement
getopmode	get operation mode of measurement

Fig. 1: *Commands for squirrel remote control.*

Sample changing at the TANDY system requires the rotation of the sample wheel exposing other samples to the Cs beam when passing over their position. To avoid sputtering those samples which are not in the measurement sequence, the data acquisition program *squirrel* has been modified to set the Cs potential to zero before moving the wheel.

All software used in the accelerator control PC has been migrated from Windows XP to Windows 7. In addition, the compiler has been upgraded from Delphi 2006 to Delphi 2010 (embarcadero [1]). The hardware access to the timer boards (National Instruments [2]) uses now the new NI-DAQmx library (from National Instruments) instead of the old NI-DAQ library which is not supported anymore.

Program name	Function (accelerator)	Program language
panda	device control (TANDEM, TANDY, MICADAS)	C#
squirrel	measurement control (TANDY, MICADAS)	Delphi 2010
hamster	measurement control (TANDEM)	C
pump control	turbo pump control (MICADAS)	Delphi 2010
nemo	data visualization (TANDEM, TANDY, MICADAS)	Delphi 2010

Fig. 2: *Migrated software programs for AMS measurements.*

The web server *vollmond*, which was used for the visualization of numerical data, had reached the end of its life cycle and has been replaced with a virtual web server hosted at D-PHYS. This server has the same functionality as the retired web server.

[1] www.embarcadero.com/products/delphi
[2] www.ni.com/dataacquisition/software

MICROPROBE SCAN CONTROL UNIT

A rastering and data acquisition system for the capillary ion microbeam

S. Roost, M.J. Simon, W. Wiederkehr, M. Döbeli

An ion microprobe has been set up at the 6 MV Tandem accelerator facility. The particle beam is collimated by a glass microcapillary to a diameter of approximately one micron. With this capillary the beam can be extracted into air without the need of a membrane. For imaging the sample can be raster scanned in both X and Y direction. Figs. 1 and 2 show selected parts of the setup.

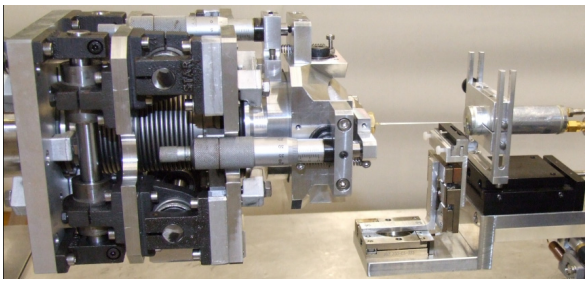

Fig. 1: *View of the capillary microprobe setup with goniometer, microcapillary, XY table, and STIM detector.*

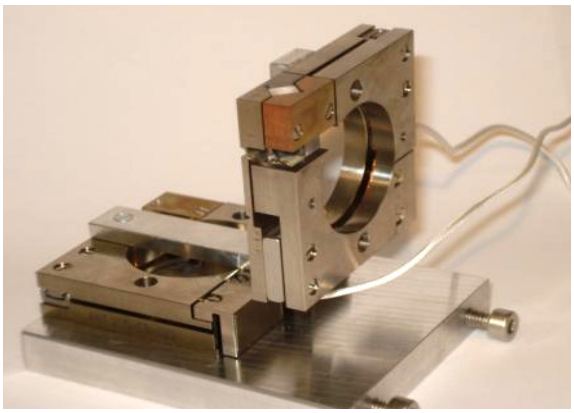

Fig. 2: *Piezo driven XY-table for precise raster scanning of the sample.*

The residual energy of transmitted particles is measured by a gas ionization counter for STIM applications (Scanning Transmission Ion Microscopy). Alternatively, emitted X-rays are recorded by a silicon drift diode to allow for PIXE imaging (Particle Induced X-Ray Emission).

Sample rastering as well as energy data acquisition is controlled by a LABVIEW program. Via the graphical interface the user can move the sample to a specific position to take energy spectra. A region of interest can be selected over which the number of events in the energy spectrum is summed. This number is displayed online as a 2-dimensional intensity plot during raster scans (Fig. 3).

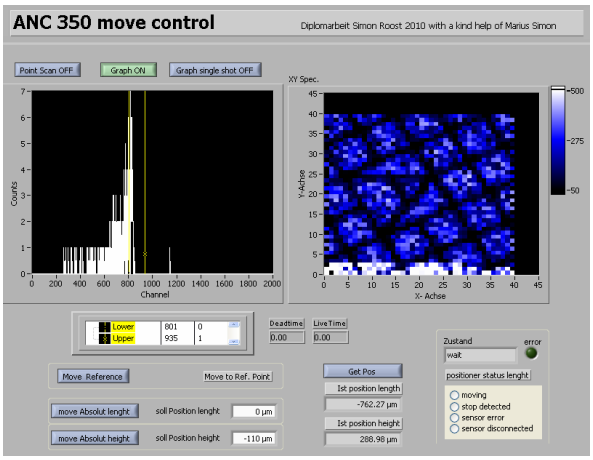

Fig. 3: *Detail of the user interface of the LABVIEW scan control software.*

Scan parameters for sample imaging such as frame position, XY dimensions, step size, and dwell time can be defined in a scan control window. Apart from the intensity plot full energy spectra are recorded at each point during a raster scan.

The scan unit is fully operational and first STIM images have been acquired (see corresponding contribution in this annual report). Presently, the acquisition speed is being improved by optimizing spectral data readout and the movement control of the piezo tables.

MINIATURE GAS IONIZATION CHAMBERS: ROUND II

New designs of compact GIC were developed and tested

A.M. Müller, A. Cassimi, M. Döbeli, R. Gruber, I. Monnet, M. Simon, H.-A. Synal, W. Wiederkehr

One year ago we began with the development of very small and simple gas ionization chambers (GIC) for different Ion Beam Analysis applications like Scanning Transmission Ion Microscopy (STIM) or backscattering experiments.

The latest design as illustrated in Fig. 1 is of a simple Geiger-Müller geometry where a copper wire anode is mounted in an aluminum tube of 60 mm length and 20 mm outer and 18 mm inner diameter. The front and back ends of the cylinder are glued-on aluminum lids.

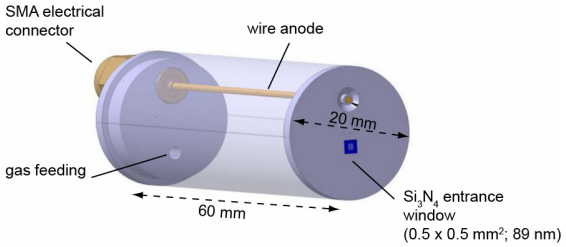

Fig. 1: *Perspective view of a mini GIC with a wire anode.*

With this simple GIC, an energy resolution of about 13 keV (FWHM) was achieved for 500 keV protons comparable to the performance of our 'state-of-the art' GIC with a Frisch grid. Additionally, the detector is very radiation hard. Even after collecting more than 50 million proton events no change in detector response is observed (Fig. 2). For the same beam spot size of a few μm^2, the pulse height of a Si PIN diode decreases by about 30 % after 15 million counts [1].

In the framework of the EU project SPIRIT measurements were performed at the IRRSUD beam line of the GANIL facility in Caen, France. Fig. 3 shows a spectrum taken with ^{129}Xe ions at 72 MeV. By optimizing detector pressure and bias voltage a relative energy resolution of 1.4 % was achieved.

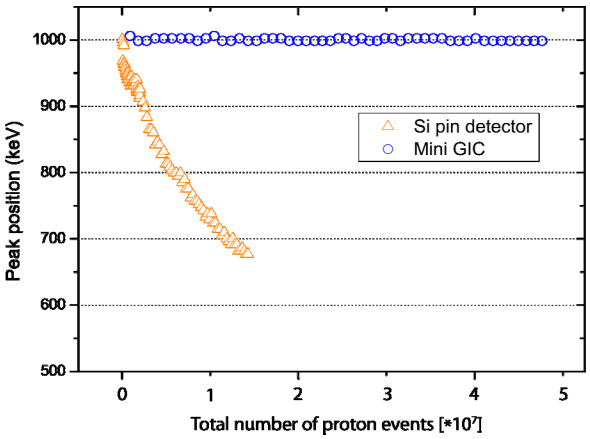

Fig. 2: *Pulse height stability for a Si PIN diode and a miniature GIC as a function of the number of accumulated 1 MeV protons.*

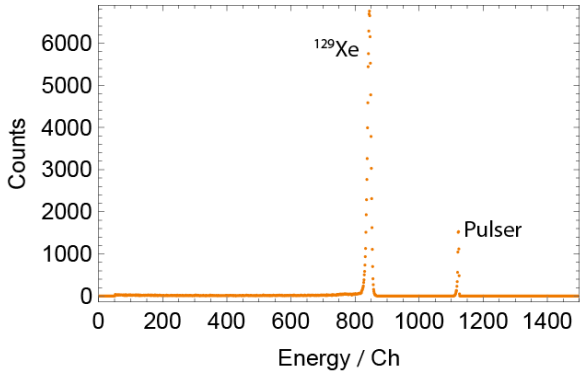

Fig. 3: *Spectrum of 72 MeV ^{129}Xe ions recorded at the IRRSUD beam line of the GANIL facility in Caen, France [1].*

Based on these findings a new detector series with Bragg geometry is under construction.

[1] A.M. Müller et al., Nucl. Instr. & Meth. B, accepted

A NEW COMPACT BACKSCATTERING GAS DETECTOR

Developments of a simple miniaturized RBS gas ionization chamber

A.M. Müller, M. Döbeli, R. Gruber, M. Limacher, M. Simon, H.-A. Synal, W. Wiederkehr

The successful developments made with small gas ionization chambers (GIC) and the good performance of the in-line Heavy Ion Rutherford Backscattering (HIBS) detector [1] was the motivation to design a miniaturized GIC for backscattering experiments (μ-HIBS) (Fig. 1).

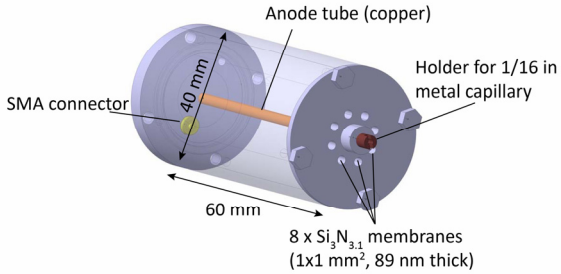

Fig. 1: *Perspective view of the μ-HIBS detector.*

The basic assembly is very simple. A 1/16" metal capillary with a 1 mm bore hole is used as beam pipe through the detector. It is fixed by hollow lock screws and sealed by o-rings on the front and back end side of the detector housing. An anode made of a copper tube (4 mm $\varnothing_{outer}$) surrounds the beam capillary with electrical insulation in between. No Frisch grid is installed. Eight holes in the detector front flange arranged in a circle (∅ 14 mm) around the beam axis are closed with $Si_3N_{3.1}$ membranes (1x1 mm^2, 89 nm thick) to act as entrance windows for the backscattered ions into the detector.

For a first backscattering experiment, the detector was installed about 50 mm from an aluminum sample coated with a 150 nm thick Al_2O_3 layer (Fig. 2). This geometry produces a solid angle of 3.2 msr for a backscattering angle of 8°. In order to obtain the best possible energy resolution for helium projectiles, an Amptek CoolFET® preamplifier was used.

In Fig. 3, a spectrum of the Al_2O_3 sample bombarded with 2 MeV He projectiles is shown. The red solid line corresponds to a RUMP simulation [2] with an energy resolution of 17 keV at the Al edge. The resolution is dominated by electronic noise, which is at the level of about 15 keV. In the near future, experiments with minimized signal cable length are planned. This should reduce electronic noise significantly.

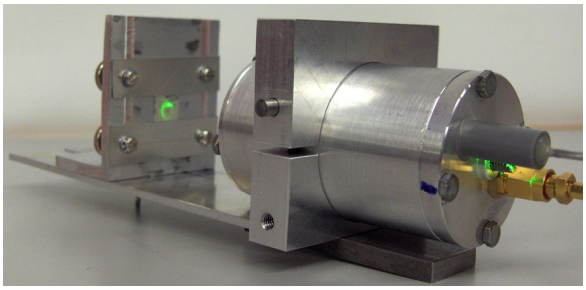

Fig. 2: *Picture of the backside of the μ-HIBS detector. A laser beam passing through the 1/16" capillary in the detector is used to adjust the position of the Al_2O_3 sample.*

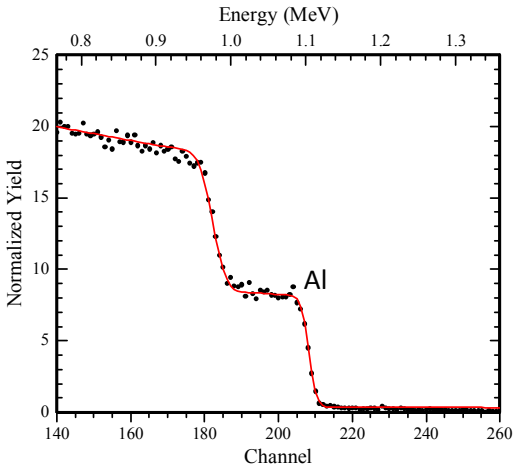

Fig. 3: *2 MeV ^{4}He Rutherford Backscattering spectrum of a 150 nm thick Al_2O_3 oxide layer on aluminum backing.*

[1] M. Mallepell et al., Nucl. Instr. & Meth. B 267 (7) (2009) 1193

[2] L.R. Doolittle, Nucl. Instr. & Meth. B 15 (1986) 227

DETETTORE POMODORO

Particle detectors do not have to be expensive

A.M. Müller, M. Döbeli, R. Gruber, M. Simon, H.-A. Synal, W. Wiederkehr

Inspired by Andy Warhol's famous soup can artwork and the results obtained during the last year with very small and simple gas ionization chambers (GIC) [1], the idea came up to make a gas detector based on a can of concentrated tomato paste.

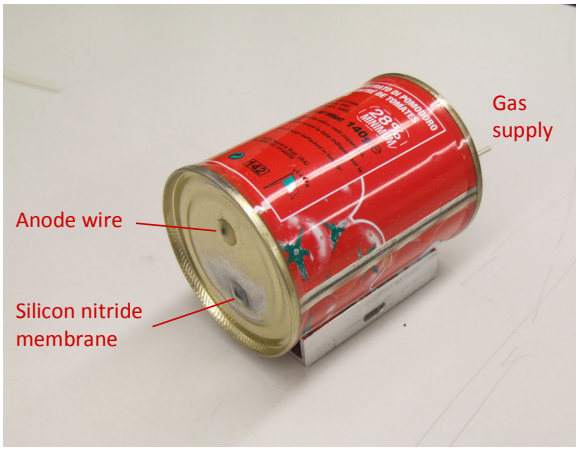

Fig. 1: *Photograph of the GIC based on a can of concentrated tomato paste.*

The basic idea was to use the empty can as detector housing and cathode. The inner surface of the can was sandblasted in order to detach the protective plastic lining. A gas feedthrough and a SMA connector, to which a (anode) wire was attached, were glued into the removed top. The can was then closed with the modified lid and sealed with epoxy. The anode wire was mechanically fixed with epoxy to the front side (Fig. 1), into which also an entrance window of $Si_3N_{3.1}$ with an area of 0.5 x 0.5 mm^2 and a thickness of 89 nm was glued.

The mechanical stability of the can and the strength of the SiN membrane allow the use of the GIC in the normal atmospheric environment. So, a first test was performed in air with a proton micro beam, which was extracted into atmosphere through a tapered glass capillary as illustrated in Fig. 2. A CREMAT® preamplifier was mounted directly on the SMA connecter. Fig. 3 shows a spectrum of 1 MeV protons recorded with the "Pomodoro" GIC. It demonstrates that a working gas ionization counter can be made by extremely simple means.

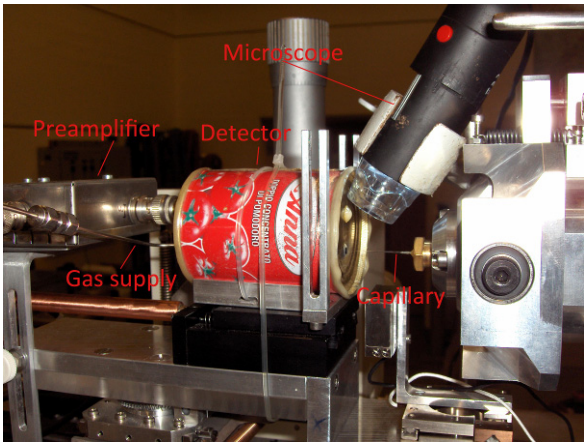

Fig. 2: *"Pomodoro" GIC placed in front of the micro-capillary setup. An electronic microscope was used for positioning the entrance window directly in front of the capillary.*

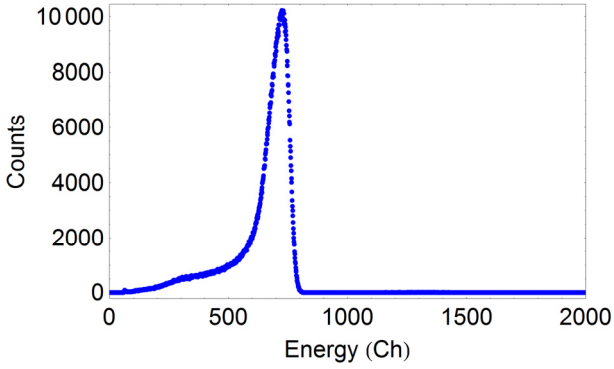

Fig. 3: *Energy spectrum of 1 MeV protons entering the "Pomodoro" detector.*

[1] A.M. Müller et al., Nucl. Instr. & Meth. B, accepted

A NEW 2D SENSITIVE DETECTOR SETUP FOR ^{36}Cl

Improving precision and isobar separation for ^{36}Cl measurements

V. Alfimov, C. Vockenhuber, H.-A. Synal

The ^{36}Cl AMS measurement setup at the 6 MV EN TANDEM accelerator has undergone a major upgrade. A new gas ionization detector is now placed between the Faraday cups for the stable Cl isotopes (Fig. 1). This reduces ion-optical losses for ^{36}Cl to a minimum, which in turn improves the precision of the isotope ratio measurements.

The main challenge for ^{36}Cl measurements is the discrimination of the interfering isobar ^{36}S by specific energy-loss measurements in a gas ionization chamber (IC). The central anodes of the new IC are shaped trapezoidal following the angular straggling of the initially 44 MeV ^{36}Cl ions inside the detector gas (see inset of Fig. 1).

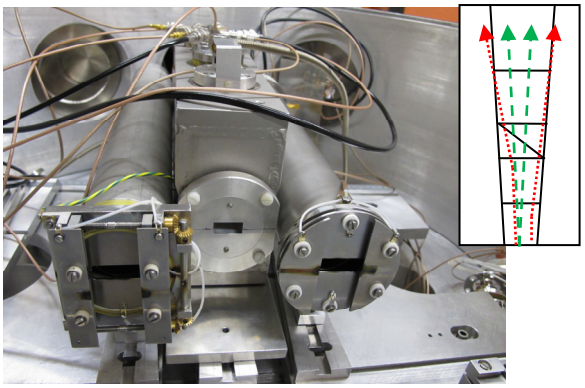

Fig. 1: *The new setup with the ^{36}Cl detector (middle) and the ^{35}Cl (position sensitive; right) and ^{37}Cl (left) Faraday cups. The insert shows how the new anode arrangement can reduce background from the high-energy tail of inelastically scattered ^{36}S ions (red) in the first two anodes.*

For effective isobaric suppression of ^{36}S the trapezoid is split into five segments, four anodes for energy-loss measurements and the central split-anode for position determination. This allows identifying scattered ^{36}S ions which have lost more energy in the first section of the IC and thus mimic ^{36}Cl ions in the other sections.

This is enough to reduce the ^{36}S background by a factor of 3. Another factor of 3 is gained in the evaluation of the time-of-flight signal between the first and third energy-loss signals.

Finally, ^{36}Cl is identified and counted in a 2D spectrum, for which the events have been gated in all previous 1D spectra (Fig. 2).

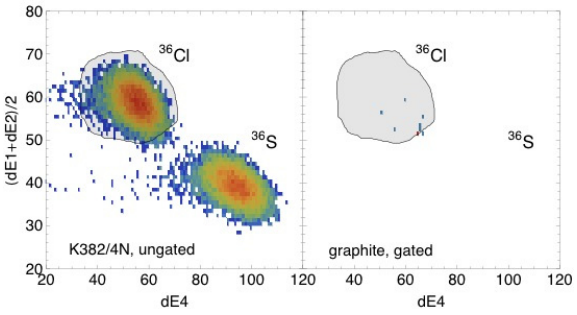

Fig. 2: *2D-spectrum (dE1+dE2 vs. dE4) of a standard (K382/4N, left) and a "blank" (graphite, right) sample. To also show the location of the ^{36}S peak the left spectrum is plotted without gates on the 1D spectra. The grey area is used to count the ^{36}Cl events.*

The overall ^{36}S background suppression was determined with a graphite sample that produced several 1000 ^{36}S cts/s. This reduces the chance of detecting real ^{36}Cl from an AgCl blank sample. With the new setup the ^{36}S suppression has been improved from 1:20000 to 1:150'000. Hence, the occasional "sulfur problem" of an unlucky AMS user has been greatly reduced. On the other hand, the rare isotope losses due to multiple gating increase slightly from 10% with the old setup to 20-30% with the new setup.

DETECTION LIMIT OF ^{236}U AT TANDY

Background analysis using a time-of-flight detector

C. Hofmann, C. Vockenhuber, M. Christl, J. Lachner, H.-A. Synal

AMS measurements of ^{236}U at low terminal voltages (< 1 MV) are more efficient than those at larger facilities. However, one might expect a higher detection limit as background discrimination is more challenging at lower energies. We investigated this problem at our TANDY AMS facility (running at 0.3 MV) using a time-of-flight (TOF) detector. The detector consists of two MCP-based timing detectors (Fig. 1) 0.45 m apart resulting in a flight time of 450 ns for 1.2 MeV U^{3+} ions. Each detector is equipped with a diamond-like carbon foil (0.5 μg/cm^2 for the start and 2 μg/cm^2 for the stop detector). The timing resolution is < 400 ps for light ions but ≈ 1 ns for U ions due to energy-loss straggling in the foils, which, however, is sufficient to identify background from ^{235}U and ^{238}U ions. Due to losses on grids and scattering in the start foil the detection efficiency is ≈ 30%.

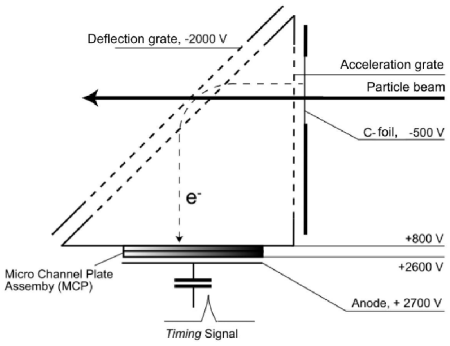

Fig. 1: *Schematic of a MCP-based timing detector.*

TOF spectra were recorded for different slit settings at the HE spectrometer. Background was calculated by peak fitting the expected p/q and E/q interferences of the abundant isotopes ^{234}U, ^{235}U and ^{238}U (Fig. 2). Tight slits (±1.5 mm) at the HE spectrometer resulted in negligible background for samples with ^{236}U/^{238}U ratios above 10^{-11}. Below that level, a background of about 4×10^{-12} from the E/q interference of ^{235}U becomes visible (Fig. 2b).

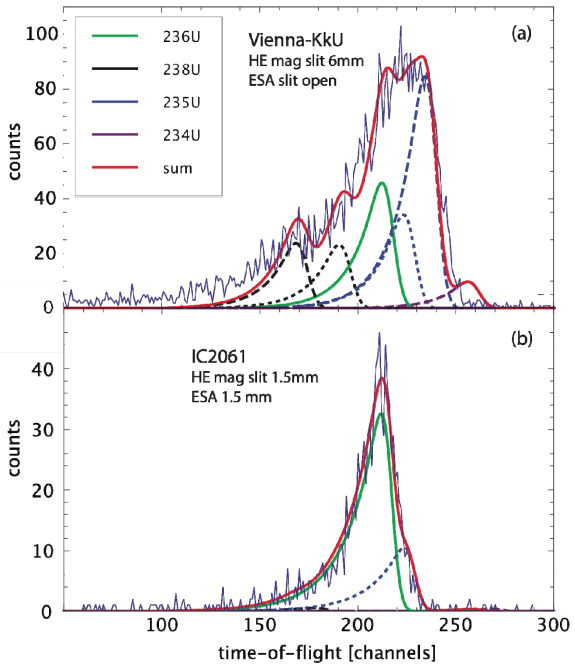

Fig. 2: *TOF spectra (thin blue line) with moderate (a) and tight (b) slit settings. The dashed lines depict the p/q (- - -) and E/q (···) interferences of the corresponding U isotope.*

First experiments with ^{236}U standard reference materials demonstrate our ability to measure ^{236}U/^{238}U-ratios in the 10^{-11} range, previously a domain of larger AMS systems equipped with TOF detectors [1]. For ratios larger than 10^{-11} background becomes negligible, if the slits at the HE spectrometer are properly set. Our overall efficiency is higher than that at larger AMS facilities due to the higher stripping yield and the use of an ionization detector (almost 100% detection efficiency) instead of a TOF system.

[1] C. Vockenhuber et al., Nucl. Instr. & Meth. B, submitted

CHLORINE-36 INTERLABORATORY COMPARISON

Can we harmonize ^{36}Cl data on a world-wide scale?

S. Merchel[1,2], W. Bremser[3], V. Alfimov, World-Wide-AMS-TEAM[4]

As a first step towards using world-wide a common ^{36}Cl standard-type material for the normalization of ^{36}Cl AMS results, we have initiated an interlaboratory comparison, but with differences in the execution of the project compared to other round-robin exercises: a) participants have given up anonymity to better optimize discussion and conclusions, b) preliminary results have been shown at various scientific meetings and workshops to discuss first trends and to increase the number of participants, c) participants had the possibility to repeat their AMS measurements and/or change measurement setups or data evaluation to improve individual data [e.g. 1]. We are aware and acknowledge that these later changes by some of the participants, which led to different overall data compared with the initial results, are not fully consistent with the idea of a normal proficiency test layout. However, these data changes were accepted to better meet the main objectives of the intercomparison: to identify and eliminate differences between AMS laboratories, thus, improving the ^{36}Cl data quality world-wide as soon as possible.

The evaluation of the final results of the eight participating AMS laboratories for three synthetic AgCl samples with ^{36}Cl/Cl ratios at the 10^{-11} (SM-Cl-11), 10^{-12} (SM-Cl-12), and 10^{-13} (SM-Cl-13) level shows no difference in the sense of simple statistical significance [2]. However, more detailed statistical analyses indicate a certain interlaboratory bias and an under-estimation of uncertainties by some of the laboratories. The round-robin data demonstrate that ^{36}Cl/Cl results from two individual AMS laboratories can differ by up to 17% (Fig. 1). Thus, the necessity for further work on harmonizing the ^{36}Cl business on a world-wide scale and on improving the measurements is obvious.

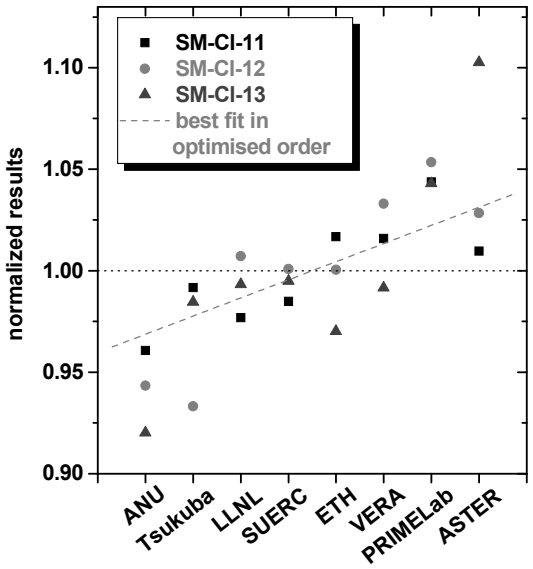

Fig. 1: *Regression of normalized results for the three investigated samples in the order of ascending average.*

[1] V. Alfimov et al., Ion Beam Physics Annual Report (2009) 13

[2] S. Merchel et al., Anal. Bioanal. Chem., submitted

[1] *Helmholtz-Zentrum Dresden-Rossendorf, Germany*
[2] *ASTER, CNRS-IRD-Université Aix-Marseille, France*
[3] *BAM, Berlin, Germany*
[4] *M. Arnold (ASTER), G. Aumaître (ASTER), L. Benedetti (ASTER), D.L. Bourlès (ASTER), M. Caffee (PRIME Lab), L.K. Fifield (ANU), R.C. Finkel (CAMS & ASTER), S.P.H.T. Freeman (SUERC), M. Martschini (VERA), Y. Matsushi (Tsukuba), D.H. Rood (CAMS), K. Sasa (Tsukuba), P. Steier (VERA), T. Takahashi (Tsukuba), M. Tamari (Tsukuba), S.G. Tims (ANU), Y. Tosaki (Tsukuba), K.M. Wilcken (SUERC), S. Xu (SUERC)*

^{14}C SAMPLE PREPARATION

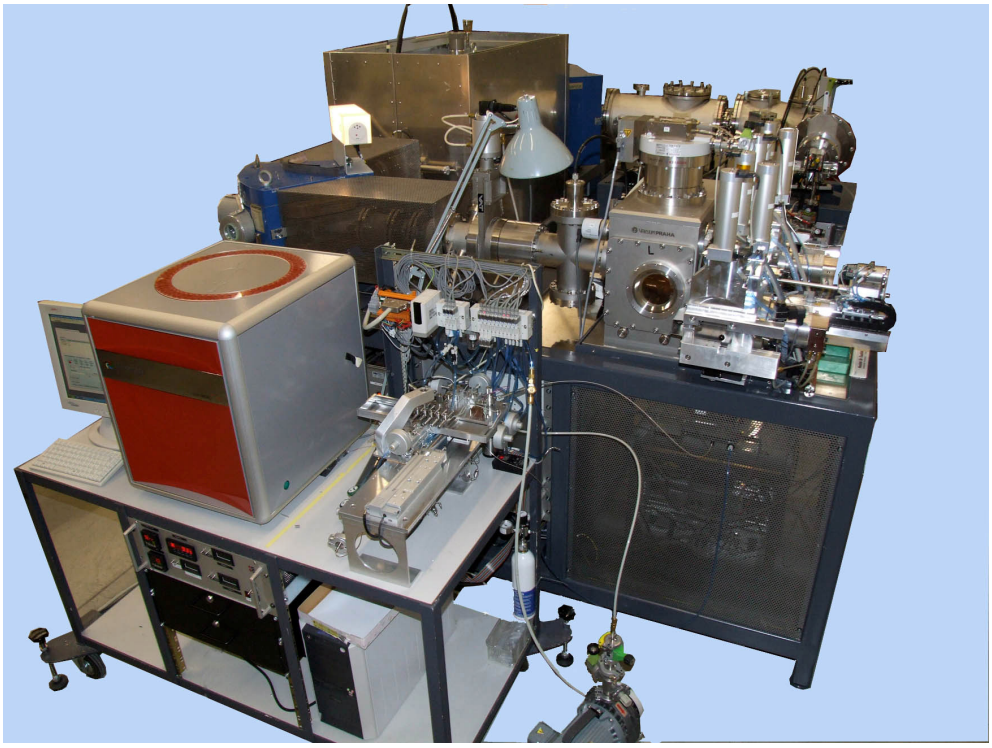

Automated radiocarbon sample preparation

Preparation of carbonates with AGE

Towards single-foraminifera dating

^{14}C dating of milliliter water samples

In-situ cosmogenic ^{14}C

Evaluating wood pre-treatment for ^{14}C dating

AUTOMATED RADIOCARBON SAMPLE PREPARATION

Sample size limits of the improved automated graphitization equipment

J. Rethemeyer[1], L. Wacker, I. Hajdas, R-H. Fülöp[1], U. Patt[1]

The radiocarbon preparation laboratory of the new AMS facility at the University of Cologne, Germany (CologneAMS) received the first model of the improved automated graphitization equipment (AGE2) for the conversion of organic samples into AMS graphite targets [1]. The system consists of an elemental analyzer for sample combustion coupled to a graphitization system with a zeolite trap for CO_2 concentration and subsequent release into reactors for reduction with H_2 (Fig. 1).

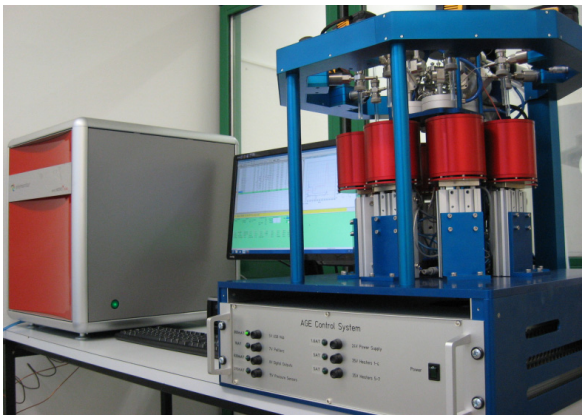

Fig. 1: *The new 'look' of the automated graphitization equipment (AGE2)*

We have tested the system with a number of reference materials (Ox-II, IAEA C6, selected VIRI samples) and the results are in good agreement with consensus values. The most critical issue is the graphitization blank. Using anthracite for normal sized samples (1 mg carbon) yielded ages between 46,000 and 51,000 years BP. External carbon is derived mainly from the tin boats in which the samples are combusted [2]. The contamination can be reduced significantly by cleaning the tin containers with organic solvents [2]. We obtained very low values for normal sized blanks (49,700 – 51,100 yrs BP) after cleaning the standard tin boats (Elementar, 4x4x11 mm) with ultra-pure dichloromethane (Fig. 2, red symbols).

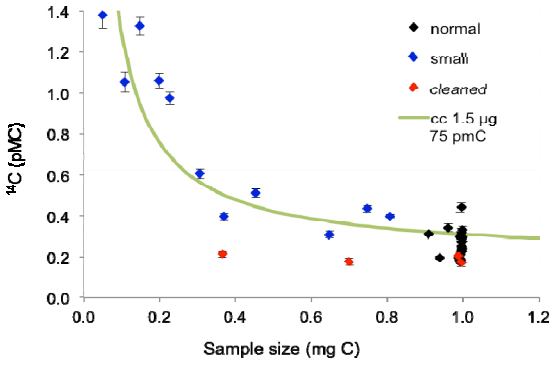

Fig. 2: *^{14}C concentration of anthracite vs. sample size. The green curve is calculated with the model of constant contamination (1.5 µg C of 75 pMC) with an offset of 0.2 pMC [2].*

We were also interested in the minimal sample size that can be reliably graphitized with the system. A size series of blanks starting from 50 µg C showed a heavy influence of the contamination introduced (about 1.5 µg C with 75 pMC) on very small samples (Fig. 2). However, promising results were obtained for relatively small amounts of anthracite (≤ 0.4 mg) combusted in dichloromethane cleaned tin boats. This will make it possible to reduce samples size and to graphitize even individual organic compounds isolated with chromatographic techniques like microbial fatty acids, which is work in progress.

[1] L. Wacker et al., Nucl. Instr. & Meth. B 268 (7-8) (2010) 931

[2] M. Ruff et al., Radicarbon 52 (4) (2010) 1645

[1] *Geology, University of Cologne, Germany*

PREPARATION OF CARBONATES WITH AGE

A new method for the conversion of carbonates to graphite

L. Wacker, R. Fülöp[1], I. Hajdas, M. Molnár[2], J. Rethemeyer[1]

Carbonates are often analyzed for radiocarbon. Presently, laboratories prepare samples by acid hydrolysis in evacuated glass tubes, subsequent CO_2 purification and reduction to graphite in self-made reduction manifolds [1]. This process is time-consuming and labor intensive. Here, we have tested a new approach to prepare carbonate samples with the automated graphitization equipment AGE [2]. A carbonate dissociation line replaces the elemental analyzer normally used for the combustion of organic samples (Fig. 1). The idea is to release the CO_2 with phosphoric acid in a septum sealed tube under He atmosphere. A similar carbonate dissociation line is often used in stable isotope ratio mass spectrometry (Thermo, Gasbench).

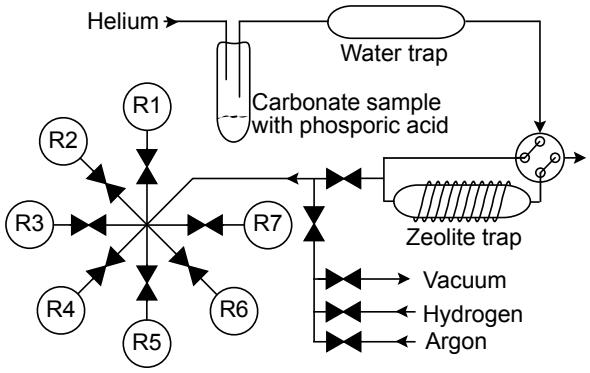

Fig. 1: *Schematic arrangement of the carbonate dissociation line connected to the AGE with its zeolite trap and the 7 reactors (R1 – R7).*

Cleaned carbonate samples are first flushed with He (100 ml/min) for 10 min in 12 ml septum sealed vials (Labco, UK) using a double-walled needle (Thermo, Germany). Then 1 ml of 85 % H_3PO_4 is added with a syringe. The samples are kept overnight at 75°C before the formed CO_2 is flushed within 2 min with 100 ml/min He to the trap of AGE. The CO_2 is then thermally released into a selected reactor, where it is converted with hydrogen to graphite.

The new method produces low processing blanks of only 0.32±0.03 pmC (46'000 years). Results of processed reference materials (IAEA-C2, FIRI-C) are very well reproduced and are in agreement with their consensus values (Tab. 1).

	Measured (pmC)	Reference (pmC)
FIRI-C	10.18 ± 0.08 10.35 ± 0.08	10.40 ± 0.01
IAEA-C2	41.27 ± 0.16 41.37 ± 0.15 41.59 ± 0.15 41.31 ± 0.15 41.26 ± 0.15	41.14 ± 0.03

Tab. 1: *Radiocarbon results from carbonate samples prepared with the presented method compared to consensus values.*

The presented setup is very simple because it gets by without a high-vacuum system and the use of liquid nitrogen. A commercially available auto-sampler will be installed next for sampling the released CO_2 in the septum sealed tubes. It will allow a fully automated graphitization of carbonates with up to 21 samples per day.

[1] M. Schleicher et al., Radiocarbon 40 (1998) 85
[2] L. Wacker et al., Nucl. Instr. & Meth. B 268 (2010) 931

[1] *Geology, University of Cologne, Germany*
[2] *also Hungarian Academy of Sciences, Debrecen, Hungary*

TOWARDS SINGLE-FORAMINIFERA DATING

Measurement of carbonate samples with a gas ion source

L. Wacker, J. Lippold[1], M. Molnár[2], H. Schulz[3]

Carbonate shells from foraminifera are often analyzed for radiocarbon to determine the age of deep-sea sediments or to assess radiocarbon reservoir ages. However, a single foraminifera contains typically only a few micrograms of carbon, while most laboratories require more than 100 µg for a radiocarbon analysis with accelerator mass spectrometry (AMS). The collection of the number of foraminifera needed is therefore time-consuming and not always possible. Here, we will present a simple way to feed CO_2 directly into the AMS gas ion source after acid decomposition of 50 – 500 µg of carbonate (5 – 50 µg C) in septum sealed vials. Only a small adaptation of our previously existing gas interface [1] was necessary (Fig. 1).

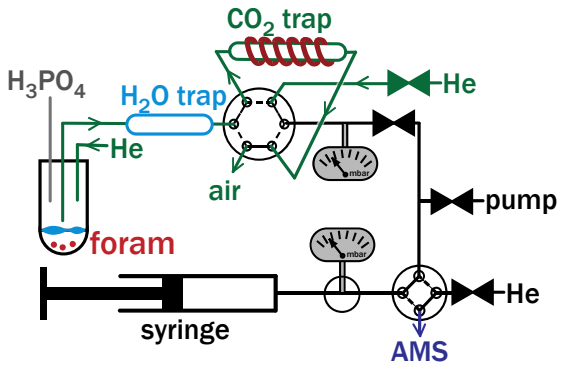

Fig. 1: *Setup of the gas handling system for carbonate samples.*

Cleaned samples (50 – 500 µg) are put into 4 ml septum sealed vials (Labco, UK), where they are first flushed with He (50 ml/min) for 15 min through a double-walled needle (Thermo, Gasbench). 0.5 ml of 85 % H_3PO_4 is added with a syringe. After 30 min of heating at 75°C, the formed CO_2 is flushed within 2 min with He (50 ml/min) into a small zeolite trap. The trap is then heated and the released CO_2 is transferred to a syringe. From here, the CO_2 is constantly pressed into the ion source (2 µg C/min flow rate).

	Weight (µg)	Measured gas (pmC)	Reference (pmC)
IAEA-C2	400	41.16 ± 0.49	41.14 ± 0.03
	200	41.14 ± 0.59	
	200	41.68 ± 0.69	
FIRI-C	400	10.69 ± 0.34	10.40 ± 0.01
	400	11.26 ± 0.39	

Tab. 1: *Results from carbonate samples measured with the gas source compared to consensus values.*

A sample of 40 µg C (400 µg carbonate) produces a $^{12}C^-$ current of up to 15 µA over 20 minutes, which results in a measurement precision of 7 ‰ for a modern sample. First results using carbonate samples with known ^{14}C concentration are shown in Tab. 1. Blank foraminifera samples (>30 kyr) were measured to contain 1.0 ±0.2 pmC, the same value as measured for ^{14}C-free CO_2 gas. The method has been also applied to samples of unknown age. Samples of < 10 µg C (< 100 µg $CaCO_3$) could be measured and even analyses of single foraminifera were possible.

Overall, preparation time is greatly reduced compared to the conventional method [2] and the method allows principally fully automated measurements of pre-cleaned samples with an auto-sampler.

[1] M. Ruff et al., Radiocarbon 49 (2007) 307
[2] M. Schleicher et al., Radiocarbon 40 (1998) 85

[1] *Heidelberg Academy of Sciences, Heidelberg, Germany*
[2] *also Hungarian Academy of Sciences, Debrecen, Hungary*
[3] *Geosciences, University of Tübingen, Germany*

^{14}C DATING OF MILLILITER WATER SAMPLES

A new sample preparation method for groundwater analyses

M. Molnár[1], L. Wacker, H.A. Synal, I. Hajdas, R. Janovics[1], L. Rinyu[1], M. Veres[2]

In this study we investigated the applicability of a new method to prepare samples from dissolved inorganic carbonate (DIC) in groundwater for radiocarbon AMS analysis.

The pretreatment method developed does not require sample preparation under vacuum, which significantly reduces the complexity. Reaction time and conditions can be easily controlled as the CO_2 content of a water sample is extracted by acid addition in a He atmosphere using a simple septum sealed test tube. A double needle with flow controlled He carrier gas is used to remove CO_2 from the test tube (Fig. 1). The CO_2 extraction yield is less than 80% mainly because a large portion of the gas remains in solution in accordance with Henry's Law. CO_2 is then trapped on zeolite without using liquid N_2 freezing.

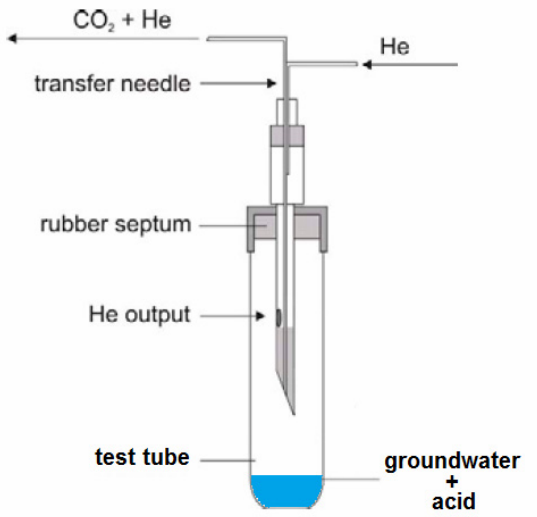

Fig. 1: *CO_2 transfer method using He carrier gas flushing through a double needle (Thermo, Gasbench) in a septum sealed test tube.*

The new method can be combined with an automated graphitization system like AGE from ETHZ [1] to have a fully automated water preparation line for AMS graphite targets. In this case, about 5-12 ml of water is needed for an AMS sample.

The greatest advantage of the new groundwater pretreatment method is the possibility to connect the extraction line directly to an AMS system using gas ion source interface (Fig.2).

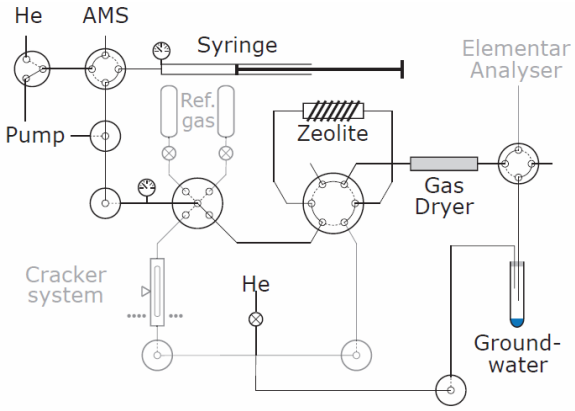

Fig. 2: *Layout of the connection of groundwater preparation line to the existing ETHZ AMS gas ion source interface [2].*

With our MICADAS AMS system we demonstrated that the ^{14}C content in 1 ml of water could be routinely measured with better than 1% precision (for a modern sample). The AMS measurement of one water sample including sample preparation takes only about 20 minutes.

[1] L. Wacker et al., Nucl. Instr. & Meth. B 268 (2010) 931
[2] M. Ruff et al., Radiocarbon 49 (2007) 307

[1] *Hungarian Academy of Sciences, Debrecen, Hungary*
[2] *Isotoptech Zrt., Debrecen, Hungary*

IN-SITU COSMOGENIC ^{14}C

A progress report on the analysis of *in-situ* produced ^{14}C at ETH

K. Hippe[1], F. Kober[1], L. Wacker, S. Fahrni, S. Ivy-Ochs, R. Wieler[1]

Due to the short half-life (5730 years), terrestrial cosmogenic *in-situ* produced ^{14}C responds rapidly to geomorphological changes forced by climate, tectonics or human activity. It is therefore a useful tool in detecting complex surface exposure histories and recent changes in landscape-forming processes. However, the analysis of the terrestrial cosmogenic *in-situ* ^{14}C nuclide requires a time-consuming procedure; first removing the atmospheric contamination from the sample (quartz) surface and then extracting the *in-situ* produced fraction from the crystal lattice.

At ETH, *in-situ* ^{14}C is routinely extracted from quartz samples. No flux agent is used for sample outgassing and thus the quartz is not melted even at extraction temperatures of 1650°C. Standard measurements using the PP-4 sample from the U. Arizona yield comparable results to those reported from U. Arizona [1] and SUERC [2], showing that quartz melting is not needed for a quantitative *in-situ* ^{14}C release. A good reproducibility of the measured ^{14}C concentrations within less than 5% can be proven by PP-4 and other samples (Fig. 1).

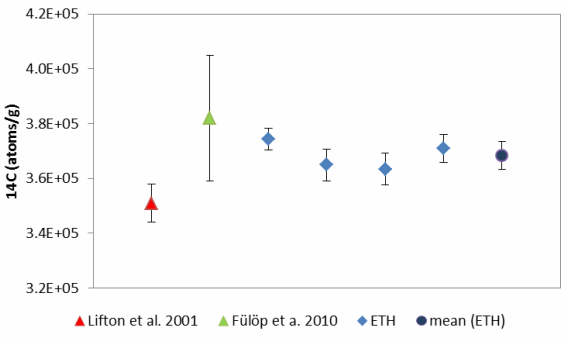

Fig. 1: *Results for PP-4 measurements.*

The total amount of extracted CO_2, which is mainly $^{12}CO_2$, reveals a strong dependence on the origin of the quartz sample. Sedimentary quartz tends to release up to 5 times more CO_2 than quartz from crystalline bedrock which yielded as little as 5 µg of C from the processed 5 g of quartz. These small samples are measured, without dilution or graphitization, with the gas ion source at the AMS system MICADAS yielding analytical uncertainties <1% and $^{14}C/^{12}C$ ratios up to 7 times above the modern ratio. A low mean procedural blank of ~4 x 10^4 ^{14}C atoms (Fig. 2) contributes to very precise *in-situ* ^{14}C analyses.

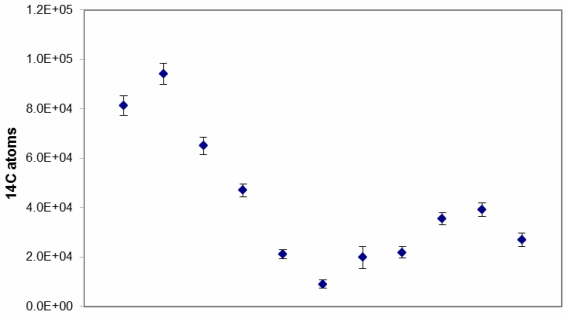

Fig. 2: *Drop in blank level, Feb-Oct 2010.*

During the past year, we have applied *in-situ* ^{14}C analysis in different multi-nuclide studies. Results from a study on catchment-wide denudation rates on the Bolivian Altiplano demonstrate the ability of ^{14}C to detect periods of sediment storage and burial. An investigation of the post-glacial ice retreat on the Gotthard Pass, Swiss Alps, illustrates how complex exposure histories caused by climatic changes can be revealed and reconstructed with the help of ^{14}C.

[1] N. Lifton et al., Geochim. Cosmochim. Acta 65 (2001) 1953
[2] R.H. Fülöp et al., Radiocarbon 52 (2010) 1288

[1] *Geology, ETHZ*

EVALUATING WOOD PRE-TREATMENT FOR ^{14}C DATING

Wood pre-treatments tested for possible sample contamination

D. Güttler, L. Wacker, N. Bleicher[1], H.-A. Synal

The ^{14}C amount in remains from archaeological sites or in ancient artifacts depends on the age of the organic material, but also on the past atmospheric ^{14}C concentration. Since the latter has undergone fluctuations over the last 50.000 years, radiocarbon dating relies on a calibration curve that connects ^{14}C age and calendar age.

At the Laboratory of Ion Beam Physics, high precision ^{14}C measurements have been made in tree rings with accuracy down to 12 years ^{14}C age and a time resolution of two years to improve the calibration curve IntCal09. The data obtained so far complement the current calibration curve in a consistent way. However, our data is offset by 15-25 radiocarbon years [1].

The measurements with the MICADAS system require extensive wood pre-treatment for the cellulose extraction and graphitization. For sample processing a base-acid (NaOH, HCl) bleaching ($NaClO_2$) method is applied [2].

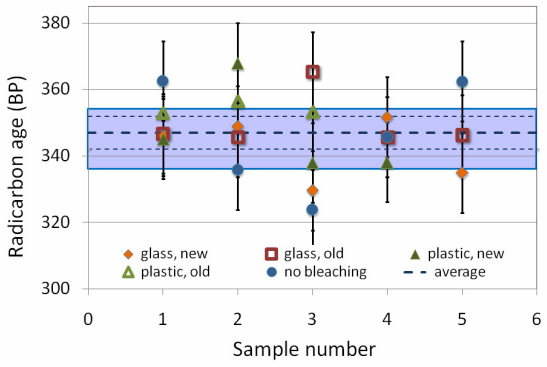

Fig. 1: *Comparison of wood pre-treatments.*

To evaluate sample processing for possible sources of contamination, pre-treatment has been tested using a pine tree ring from 1515 AD. ^{14}C results have been compared in terms of a) test tubes (plastic vs. glass) b) chemicals (fresh vs. old) and c) bleaching step applied (yes or no). The results in Fig. 1 show there are no significant differences between the various sample series. Furthermore no offset is observed with respect to the IntCal09 curve (blue band). The average of all samples yield a ^{14}C age of 347 ± 5 y BP, which is in very good agreement with 345 ± 8 for 1515 AD.

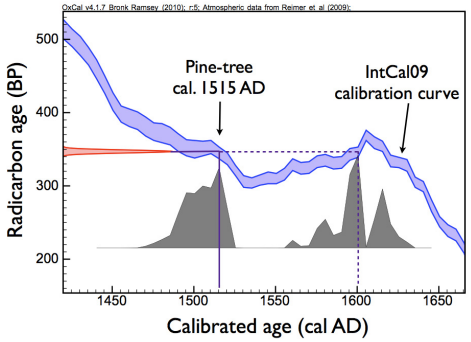

Fig. 2: *Radiocarbon age averaged over all wood samples. Intersections with the calibration curve yield probabilities for the sample age.*

The pre-treatment tests show that the ^{14}C analyses at the ETH AMS facility are highly reproducible and that the applied method of sample processing is applicable for high precision measurements. From these tests it can be concluded that contamination during sample preparation seems not to be the source of the ~20 yr offset in ^{14}C ages discussed in last years annual report [1].

[1] L. Wacker et al., Ion Beam Physics Annual Report (2009) 48
[2] N. Němec et al., Radiocarbon 52 (2010) 1358

[1] *Laboratory for Dendrochronology, City of Zurich*

RADIOCARBON APPLICATIONS

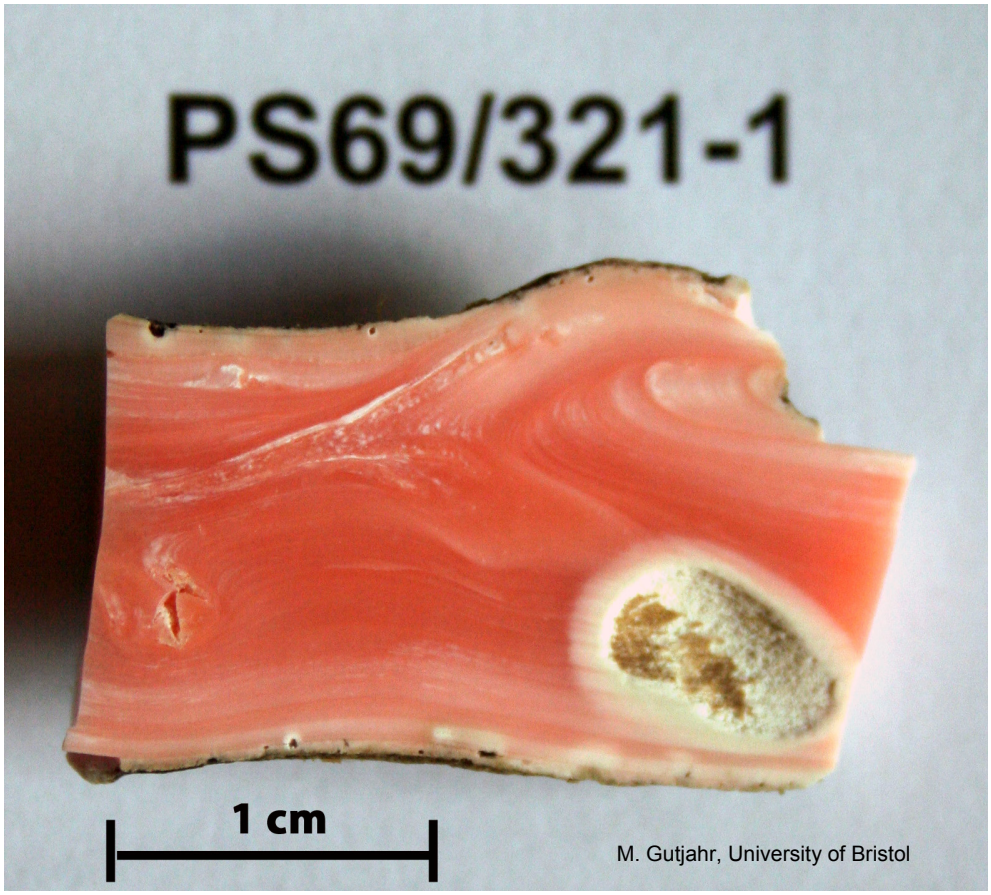

The ^{14}C samples of 2010

Large flood events around the old Samarkand

Fresh, old leaves from Lajatico, Italy

'Bomb peak' as our daily bread

^{14}C source apportionment of aerosols

Compound-specific ^{14}C analysis of aerosols

Compound-specific radiocarbon analysis

THE ^{14}C SAMPLES OF 2010

An overview of sample types, applications and collaborations

I. Hajdas, C. Biechele, G. Bonani, S. Iglesias, M. Maurer, H.-A. Synal, C. Vockenhuber, L. Wacker

During 2010, we analyzed 3854 ^{14}C samples (solid and gas) on our MICADAS system (Tab. 1). More than 1300 samples had been treated (cleaned) and prepared in our laboratory. Most of these were analyzed in graphite form. Only 20 samples turned out to contain less than 100 micrograms of C and were measured as CO_2 gas samples.

A large number of the prepared targets consisted of standards (oxalic acid II) and blanks as well as IAEA reference materials (wood, cellulose, oxalic acids). These samples are measured along with the unknown samples to ensure quality of the preparation and measurements procedures.

	Number of Samples	
Sample Type	**2009**	**2010**
Standards (OXA II)	324	290
Blank Samples	230	283
Reference materials (IAEA)	85	130
Subtotal	639	703
Category		
Internal	237	110
Gas Samples	450	793
Gas Test Samples		200
Archaeology	518	764
Past Climate	118	191
Environmental	118	145
Art	144	169
Other types (wine, wax, etc)		26
External Solid Targets		753
Subtotal	1535	3151
Grand Total	**2224**	**3854**

Tab. 1: *Sample numbers of various applications prepared and measured in 2010.*

Now that the MICADAS system is operating routinely the number of samples in category 'Internal' has become less during the last years and includes samples mainly prepared during school projects.

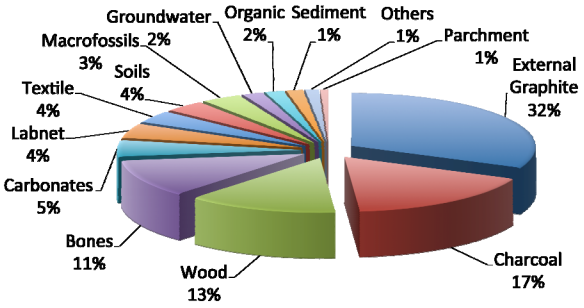

Fig. 1: *Sample 'pie' shows percentage of various types of material analyzed in 2010.*

More than 50% of all the samples submitted for radiocarbon dating had their origin in an archaeological context. When compared to the year before we observe a larger share of charcoal and bones being prepared in our laboratory (Fig 1). Also new types of materials such as oil products were among the samples submitted for analysis.

LARGE FLOOD EVENTS AROUND THE OLD SAMARKAND

^{14}C dating of archaeological sites and numerical models of overland flow

L. Malatesta[1], S. Castelltort[1], V. Picotti[2], S. Mantellini[3], I. Hajdas, G. Simpson[4], L. Wacker, S. Willett[1]

The rich human history of the Central Asian Silk Road provides an insight into the social, political as well as climatic development of the region. Several archaeological sites document the various irrigation schemes that were designed to support human presence in and around the Tian Shan during the arid late Holocene (ca. 300 BC - 500 AD). This is particularly striking in the Middle Zeravshan Valley in Uzbekistan. From the 4th century BC onwards, it was one of the Silk Road main paths and extensive irrigation works were engineered to sustain the agriculture around the historical city of Afrosiab, now Samarkand. The irrigation system upstream of the historical city of Afrosiab consisted of two main canals, the Dargom and the Jangi Aryk. We investigated deposits of a destructive flood, found in a particularly well studied dwelling next to the Dargom, with sedimentological and surface processes methods. We thus obtained original constraints on the nature of extreme precipitation events during this time (80-240 AD).

We estimated that an intense precipitation event of at least 65 mm/h for at least 2 hours allowed for a 0.6 m high flooding of the archaeological site based on a numerical model surface overland flow. Elevated dwellings, the usual construction type in the valley at this time and the recurrence of flood horizons in the stratigraphy attest to a repetition of floods during the first centuries AD in western Central Asia.

We also established a new precise quantitative timeframe for the canals' construction time. The flood-related sediments were dated with radiocarbon and analyzed with XRD methods. The radiocarbon dating was performed on bones, teeth and charcoals collected in the archaeological sites (Fig. 1).

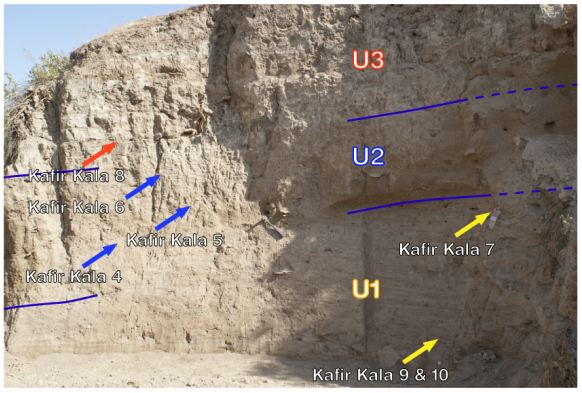

Fig. 1: *Sampling site in the moat of the Kafir Kala fortress. The units U1-3 document the maintenance of the moat: U1 is the first deposition unit, which has been cut for re-deepening of the moat; U2 is one homogeneous collapse unit that ensued the maintenance and U3 is the following continued sedimentation in the moat. The arrows show ^{14}C samples location.*

The nature of the sediments confirmed the presence of the two canals in the 2nd century AD. Furthermore, we could discredit the idea that the canals were a product of the highly centralized Achaemenid state (4th century BC). Our findings support the hypothesis that they were rather built by the non-centralized and loosely organized Kushan society.

[1] *Geology, ETHZ*
[2] *Earth Sciences, University of Bologna, Bologna, Italy*
[3] *Archaeology, University of Bologna, Ravenna, Italy*
[4] *Geology and Paleontology, University of Geneva*

FRESH, OLD LEAVES FROM LAJATICO, ITALY

Radiocarbon dating as a tracer of old CO_2

I. Hajdas, G. Bonani, P. Cherubini[1], M. Notzli[1], M. Saurer[2], H.-A. Synal, C. Vockenhuber, L. Wacker

Radiocarbon analyses provide a tool for detection of 'old' carbon dioxide that can be applied to study volcanic hazards or a presence of fossil fuels in various environments as well as products (i.e. bio-fuels). An aspect, which is of interest here, is the extent of 'old CO_2' emissions and their effect on the ^{14}C concentration in living biomass.

A geological spring of carbon dioxide, which is located near the small town of Lajatico, Pisa, Italy, has been intensively studied as an area naturally enriched in CO_2. In a small plot downstream from the spring, evergreen oaks (*Quercus ilex*) grow in an atmosphere of over 600 ppm CO_2. Dendrochronological studies supported by stable isotopes and ^{14}C analyses of tree rings have shown no advantages of an enriched CO_2 atmosphere for the growing biomass [1, 2].

Fig. 1: *'I Borboi' CO_2 spring near Lajatico. Leaves growing above the spring were sampled for ^{14}C analysis.*

During a 2009 excursion organized for students of Department of Geography of the University of Zurich, fresh leaves of evergreen oak were sampled directly at the spring. In addition, 'a control' sample of oak leaves was taken from the top of the hill where no 'old' CO_2 was expected. The spring is located in a small canyon and the heavy CO_2 is expected to remain in the lower part of that canyon.

Fig. 2: *The 'old' leaf (9315±40 BP) that grew above the spring.*

The ^{14}C content measured in the leaf that grew right above the spring shows that over 60% of assimilated $^{14}CO_2$ originated from the spring (pMC=31.35%). But also the leaf sampled up on the hill (control sample) showed some traces of old CO_2 (pMC=97.5%). This wide range of influence by spring emitted carbon dioxide on ^{14}C ages of biota is of great relevance to archaeological samples found in volcanic regions. More systematic sampling in the region of Lajatico, including trees from the 'clean' area might add to understanding of the effect.

[1] R. Tognetti et al., Tree Physiology 23 (2003) 997
[2] M. Saurer et al., New Phytologist 146 (2000) 59

[1] *WSL, Birmensdorf*
[2] *Atmospheric Chemistry, Paul Scherrer Institut, Villigen*

'BOMB PEAK' AS OUR DAILY BREAD

Remains of atmospheric nuclear tests as a tracer and 'forgery' detector

I. Hajdas, G. Bonani, H.-A. Synal, C. Vockenhuber, L. Wacker

Natural ^{14}C is a long-lived radioactive isotope of carbon that is produced by thermalized secondary cosmic ray neutrons captured on atmospheric nitrogen. The above-ground nuclear tests that took place in the 1950/60s left behind artificially produced radiocarbon that added to the naturally produced ^{14}C and at that time doubled the ^{14}C concentration in the atmosphere. The presence of this 'bomb peak' creates a complication for the radiocarbon dating. On the other hand, the ^{14}C excess provides an excellent tracer that is being used in environmental, biomedical and forensic studies. It is often applied to detect forgery in art and antique pieces. Thanks to the data of atmospheric ^{14}C concentration collected for the last half century [1], it is possible to pin down the year when the 'bomb peak' carbon was fixed into the organic or inorganic matter of the sample being investigated.

Our laboratory performs such analyses for environmental studies (soils, trees) as well as authenticity checks that allow the detection of forgery attempts (Tab. 1). Sporadically, so-called 'modern' samples appear also in archaeological records or past climate studies.

Analyses 2010	Total	'Bomb peak'
All Samples	1399	165
Authenticity analyses	141	28

Tab. 1: *Number of measured ^{14}C 'Bomb peak' samples (graphite targets).*

It is important to note that the tracer is disappearing from the atmosphere. The uptake of the CO_2 by the world's oceans moved the artificial ^{14}C to levels close to natural levels, which were raised by another anthropogenic 'Suess' effect, i.e. the addition of ^{14}C free CO_2 from fossil fuel combustion.

As the 'peak' flattens out (Fig. 1) it is still possible and quite exciting to use it as an illustrative tool for working with students during School Projects. Often students bring own material that is not older than 50 years. During one of the projects that took place this year a sandwich and a banana was sampled, as well as a piece of hair 'sponsored' by one of the students. Small differences in activity measured in $F^{14}C$ (Fraction Modern=1.0 for year 1950AD) [2] are observed between bread, sesame seeds and fresh salad. A detailed discussion will be possible when the data for atmospheric ^{14}C for 2009 and 2010 will be available (Fig. 1).

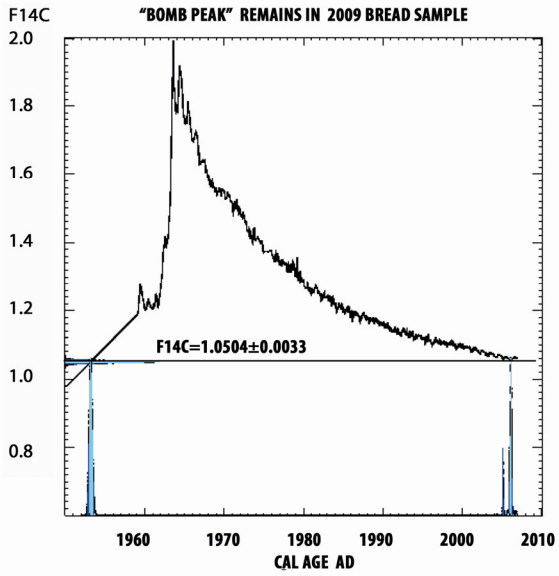

Fig. 1: *CALIBomb shows the year of wheat growth $F^{14}C=1.0504\pm0.0033$ corresponds to 1956 and 2006 AD but the 1956 AD can be excluded.*

[1] I. Levin et al., Sci. Total Environment 391 (2008) 211

[2] P.J. Reimer et al., Radiocarbon 46 (2004) 1299

^{14}C SOURCE APPORTIONMENT OF AEROSOLS

A new sample preparation system at University of Bern

Y.L. Zhang[1,2], S. Szidat[1], N. Perron[2], A.S.H. Prevot[2], L. Wacker

Carbonaceous aerosols, which comprise the large fractions of elemental carbon (EC) and organic carbon (OC), badly affect climate and human health [1]. However, there is a large uncertainty about detailed apportionment and quantification of their sources due to the vast number of origins and chemical compounds associated with the aerosols. Radiocarbon measurements have been shown to be a useful isotopic tracer for distinguishing contemporary and non-fossil emissions [2, 3].

Since OC and EC are influenced by very different sources [3], this method requires a clear separation of both fractions, which is not trivial. On the one hand, some thermal unstable OC compounds may char during the combustion at low temperature, which will produce additional, apparent EC. On the other hand, some non-refractory EC may be removed prematurely together with recalcitrant OC at intermediate temperature. As a result, the ^{14}C measurement of EC may then be biased.

Thus, a major improvement in sample preparation is necessary. In order to evaluate the extent of charring during analysis, we performed sample preparation with a new commercial Sunset Thermo-Optical OC/EC Analyzer. This instrument is equipped with a NDIR detector to quantify the formed CO_2. It also monitors the optical properties of the remaining aerosols on the filters with a 660 nm tuned diode laser during the thermal treatment. The gas flow parameters of this analyzer are adjusted and stabilized to 65 mL/min of pure O_2. The resulting CO_2 is collected in designated cryogenic traps [4] after quantification by the NDIR detector. The setup is sketched in Fig. 1.

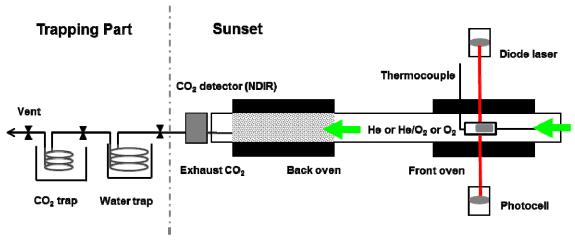

Fig. 1: *The new sample preparation system coupling a commercial Sunset OC/EC Analyzer to cryogenic traps.*

The main advantage compared to the previous setup [4] is the online optical monitoring of the remains of aerosols on the filters during analysis by the Sunset OC/EC Analyzer. Charring was significantly reduced to less than 5% when analyzing water-extracted summer and winter filters under pure O_2.

In the future, the thermal course of the Sunset Analyzer program will be tested on a variety of filters from different locations to find the best method to separate the OC/EC fractions for ^{14}C measurements.

[1] U. Pöschl, Angew. Chem. Int. Ed. 44 (2005) 7520
[2] L.A. Currie, Radiocarbon 42 (2000) 115
[3] S. Szidat et al., Atmos. Chem. Phys. 9 (2009) 1521
[4] S. Szidat et al., Nucl. Instr. & Meth. B 223-224 (2004) 829

[1] *Chemistry and Biochemistry, University of Bern*
[2] *Atmospheric Chemistry, Paul Scherrer Institut, Villigen*

COMPOUND-SPECIFIC ^{14}C ANALYSIS OF AEROSOLS

Sources of dicarboxylic acids and humic-like substances in air

S. Fahrni[1], S. Szidat[1], E. Vogel[1], L. Wacker, M. Rzaca[2], H. Puxbaum[2], H. Bauer[2]

Dicarboxylic acids (DCA) and humic-like substances (HULIS) in carbonaceous aerosols have received great attention in the past. The research on these compounds is strongly motivated by their abundance and their hydrophilicity, which is related to the ability to influence cloud condensation processes. Even though DCAs and HULIS were studied extensively, a clear attribution to the sources has so far been not possible. In order to provide quantitative information on their sources, ^{14}C source apportionment is a promising method: carbon from fossil, i.e. radiocarbon-free sources, is distinguished from carbon of biogenic and biomass-burning emissions, which exhibit the contemporary radiocarbon level.

The method for the separation of DCAs comprises water extraction and preparative 2D-chromatography by means of ion chromatography and HPLC separation [1]. Separation of HULIS samples was performed at the Technical University of Vienna with a method developed by Limbeck et al. [2]. Filters were extracted with 0.1 N NaOH and acidified to enable their retention on a solid phase extraction column. HULIS were eluted from the column with methanol and eluates were mixed with diluted nitric acid. These solutions were loaded onto a strong anion exchange column and eluted with diluted ammonia. The fractions were collected in PFA vials and transported to the University of Bern for further processing. Aqueous solutions were concentrated under a flow of nitrogen and concentrated HULIS solutions were transferred to pre-cleaned quartz vessels. The concentrates were dried, treated with 1 M HCl in order to remove carbonates, and dried again. Samples from both DCAs and HULIS were combusted and ^{14}C was analyzed in the resulting CO_2 with the gas feeding system at the MICADAS.

The results show that the DCA oxalic acid is more strongly influenced by non-fossil contributions than is the organic carbon in general. The main findings for HULIS suggest residential wood heating as the major source of this compound class during winter. Slightly more fossil contributions are observed during summer.

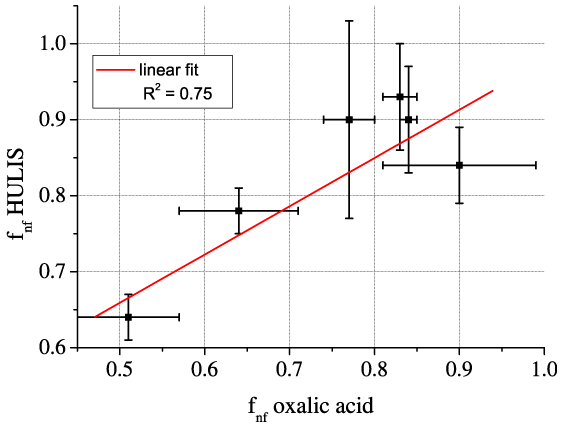

Fig. 1: *Correlation between radiocarbon results from oxalic acid and HULIS.*

A significant correlation between the non-fossil fractions (f_{nf}) of oxalic acid and HULIS was found indicating common sources (Fig. 1). A combination with other techniques such as aerosol mass spectrometry and a determination of levoglucosan may help to subdivide non-fossil contributions further into biogenic and biomass burning contributions.

[1] S.M. Fahrni et al., Radiocarbon 52 (2010) 752

[2] A. Limbeck et al., Analyt. Chem. 77 (2005) 7288

[1] *Chemistry and Biochemistry, University of Bern*

[2] *Chemical Technologies and Analytics, Technical University of Vienna, Austria*

COMPOUND-SPECIFIC RADIOCARBON ANALYSIS

Analytical developments and application to lake sediments

A. Birkholz[1], M. Gierga[1], R.H. Smittenberg[1], S.M. Bernasconi[1], I. Hajdas, L. Wacker

The project "Compound-specific radiocarbon dating on lake sediments" aims at determining the ages of specific biomarkers in lacustrine sediments. An integral part of the project is the development of organic geochemical methods to isolate individual organic compounds from sediments. The ^{14}C content of biomarkers obtained using the MICADAS gas ion source system requires the correction for contamination acquired in the chromatographic preparation systems i.e. determination of procedural backgrounds. One major scientific goal is to gain a better insight into the build-up and recalcitrance of soil organic carbon in surrounding terrestrial ecosystems. Secondly, we seek to find compounds that reflect the age of deposition of the sediment in order to provide an alternative dating tool for lake sediments.

During the year 2010, the main focus of the project was on method development. Accurate and reliable dates are a prerequisite for our study. A new method for the separation and purification of branched Glycerol Dialkyl Glycerol tetra ethers (GDGTs) from soil and lake sediments was developed using high performance liquid chromatography (HPLC). These GDGTs are produced by soil bacteria. Amounts of the isolated compounds ranged from 1.5 – 15 µg C. The radiocarbon results show that the age of the GDGT is much older than the depositional age of the sediment. This confirms the hypothesis that the compounds pre-age in the catchment soils before entering the lake sediment. Secondly we established a new method to isolate long-chain fatty acids (LCFAs) by the use of HPLC. LCFAs, (>20 C atoms) are primarily biosynthesized by terrestrial higher plants and are, therefore, typically regarded as biomarkers for terrestrial organic matter. First ^{14}C measurements with isolated fatty acid standards of varying C chain-length and with varying sample size were accomplished by the end of the year.

For both methods we enlarged the data set of processed standards (^{14}C 'dead' and modern substances). With the results of these measurements we are able to infer a constant contamination of extraneous C to the samples from the isolation and preparation procedure. The main finding was that samples smaller than 10 µg C become easily contaminated (Fig. 1).

Next to the methodological developments, we purified individual *n*-alkanes from a sediment core of Lake Ioannina, Greece. These plant-wax derived compounds may have been deposited in the sediment by aeolian transport, which would make them suitable for chronological purposes. We measured the ^{14}C content of four individual *n*-alkanes from one sample and a combination of these four *n*-alkanes from three samples. The alkanes showed an age offset compared to expected ages, albeit constant, which makes this a partial success. We plan to date individual fatty acids from the same samples to evaluate their potential for dating purposes.

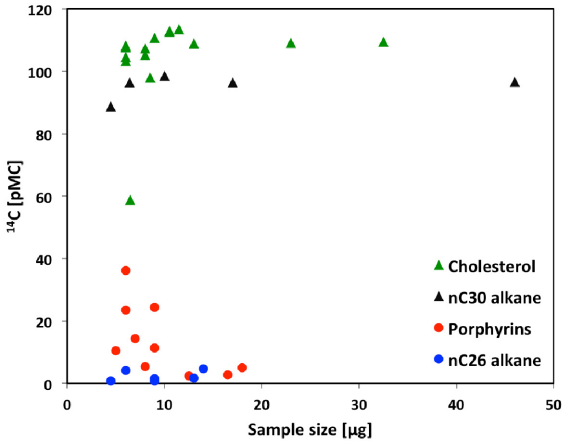

Fig. 1: *Procedural blanks (modern in triangles, ^{14}C dead in circles) versus samples size.*

[1] *Geology, ETHZ*

APPLICATIONS IN GEOLOGY

A modern ^{10}Be production rate

The cosmogenic ^{21}Ne production rate revisited

Chlorine-36 depth profile from Vue des Alpes

Post-depositional impacts on 'Findlinge'

Surface exposure ages from the Gotthard Pass

Landscape dynamics in the Albula region

LateGlacial and Holocene glacier dynamics

Ice-sheet configuration in the high Arctic

Glaciations at Uludağ Mountain (NW Turkey)

Glacial history of the northwestern Tian Shan

Pleistocene glaciation in the arid Central Andes

Glaciation history of Queen Maud Land

Erosion rates from degraded mountain basins

^{10}Be based sediment production in the Amazon

Cosmogenic erosion rates across the Andes

Correlation of Makran fluvial terraces

The rise of the eastern Alps

^{36}Cl exposure dating of landslides in Trentino

Dating of landslides in the Kyrgyz Tien San

^{36}Cl exposure dating of palaeo-earthquakes

Ancient quarries in western Turkey

A MODERN ^{10}Be PRODUCTION RATE

The rock avalanche of 1717 AD in Val Ferret (Mont Blanc Massif, Italy)

N. Akçar[1], V. Alfimov, S. Ivy-Ochs, P. Deline[2], P.W. Kubik, M. Christl, C. Schlüchter[1]

We have measured cosmogenic ^{10}Be in surface samples of nine large granitic boulders within the deposits of a rock avalanche that occurred in 1717 AD in the upper Val Ferret valley, Mont Blanc Massif, Italy (Figs. 1 and 2) [1].

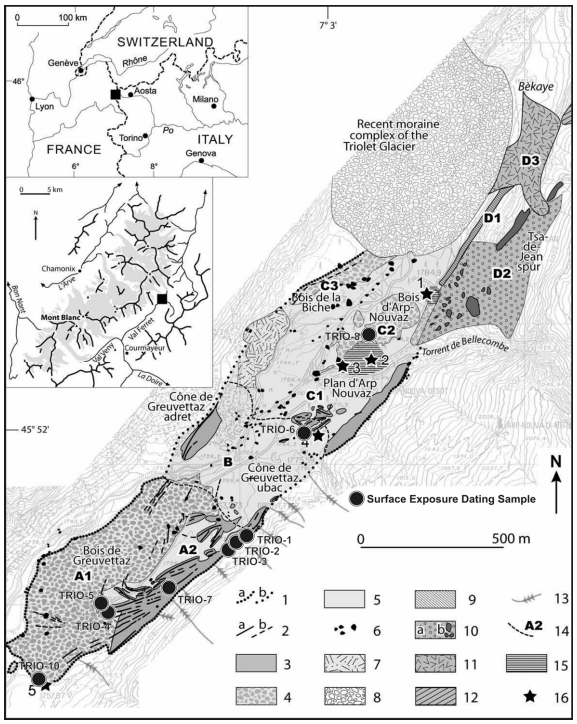

Fig. 1: *Map of upper Val Ferret deposits and locations of sampled boulders. 1: Limit of the deposits of Plan d'Arp-Nouva/Greuvettaz; 2. granitic ridges; 3: till [2]; 4: chaotic blocks; 5: alluvial deposits; 6: megablocks; 7: local rockfall deposit; 8: recent moraine complex of Triolet Glacier; 9: diamicton consisting of granite blocks within a schistose matrix; 10: granitic veneer (a), with megablocks (b); 11: deposit of granite blocks; 12: till comprising weathered granite blocks; 13: snow avalanche couloir; 14: limit and number of Arp-Nouva/Greuvettaz and Tsa-de-Jean sectors; 15: peat bog; 16: location of radiocarbon dates [1, 2].*

This site of a historically known exposure time is suitable for ^{10}Be production rate calibration.

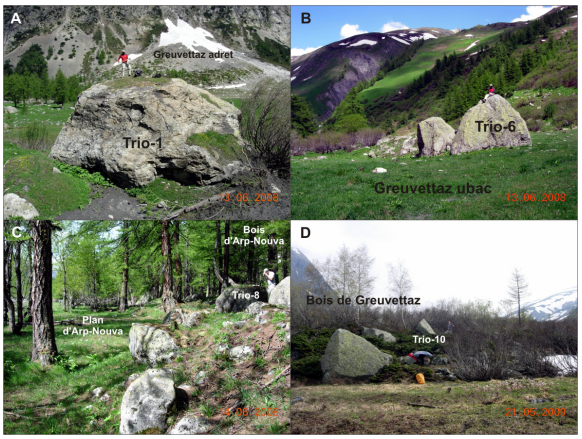

Fig. 2: *Sampled boulders in the Ferret Valley.*

The ^{10}Be concentrations normalized to the 07KNSTD ^{10}Be AMS standard were corrected for shielding of the cosmic ray flux by the surrounding topography, dip of rock surface, sample thickness and snow cover. Temporal changes in palaeomagnetic intensity and polar wander were taken into account by the scaling procedures (http://hess.ess.washington.edu/). Our calibration yielded the following modern sea level, high latitude ^{10}Be production rates for the scaling schemes St (4.37±0.17 at. $g^{-1}\cdot a^{-1}$); De (4.66±0.18 at. $g^{-1}\cdot a^{-1}$); Du (4.52±0.17 at. $g^{-1}\cdot a^{-1}$); Li (4.98±0.19 at. $g^{-1}\cdot a^{-1}$); Lm (4.39±0.17 at. $g^{-1}\cdot a^{-1}$) [1]. Our production rates agree well with the average of the global dataset.

[1] N. Akçar et al., Earth Planet. Sci. Lett., submitted

[2] P. Deline and M. Kirkbride Geomorph. 103 (2009) 80

[1] *Geology, University of Bern*
[2] *EDYTEM Laboratory, University of Savoie, France*

THE COSMOGENIC ^{21}Ne PRODUCTION RATE REVISITED

Evaluating the ^{21}Ne production rate via known ^{21}Ne-^{10}Be data

F. Kober[1], V. Alfimov, S. Ivy-Ochs, P.W. Kubik, R. Wieler[1]

The production rate of *insitu* produced cosmogenic ^{21}Ne was for a long time only calibrated based on a handful of samples. In an effort to circumvent problems of pre-exposure, unknown erosion rates or complex exposure at calibration sites, a new approach was chosen to evaluate the ^{21}Ne production rate. Advantage was taken of the fact that in numerous samples both ^{21}Ne and ^{10}Be had been measured at ETH (Fig. 1). Since the ^{10}Be production rate is fairly well calibrated at multiple sites, one can assume its production rate as a known variable. By using then the unique ^{21}Ne/^{10}Be ratio at a specific point in time under a specific erosion rate the ^{21}Ne production rate can be estimated. This unique coupling can be graphically expressed in an erosion island plot (Fig. 1).

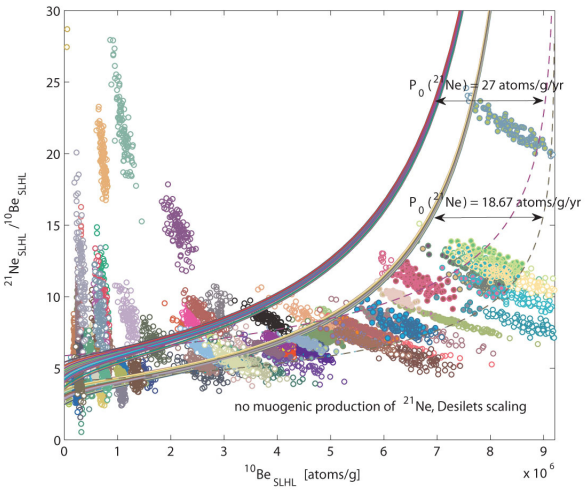

Fig. 1: *Erosion-island plot displaying the ETH data shown as Monte Carlo simulated data points together with two erosion islands, where one is based on a ^{21}Ne production rate of 18.67 atoms/g/yr defined by the best fit to the ETH data, while the one with 27 atoms/g/yr is shown to highlight the misfit of the erosion island for such a high ^{21}Ne production rate with the data set.*

Since samples with complex exposure had not been excluded a priori in order to avoid a pre-selection, the best fit of an erosion island with the data and thus the most probable ^{21}Ne production rate is then taken where a plateau is approached (Fig. 2), which develops when consecutively samples with low ^{10}Be concentrations are excluded. Since these samples have the highest likelihood to have suffered a complex exposure it can be demonstrated with the data-fit that their "too high" ^{21}Ne production rate will be misleading (for details see [1]). The ^{21}Ne production rate determined based on this method is 18.7 atoms/g/yr.

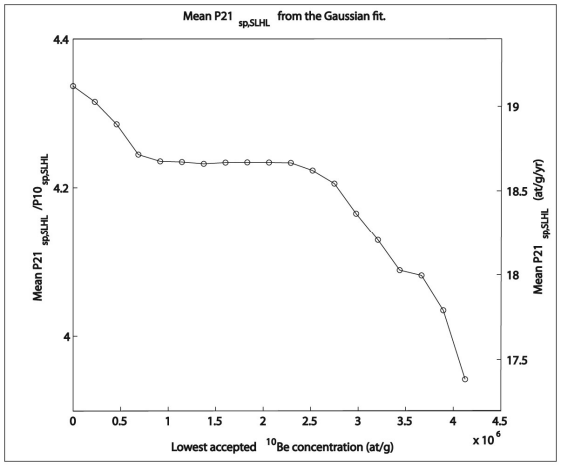

Fig. 2: *^{21}Ne/^{10}Be ratios, ^{21}Ne production rates vs. the lowest accepted ^{10}Be concentration. The plateau between 1 and 3 million ^{10}Be atoms/g defines the ^{21}Ne production rate the best.*

[1] F. Kober et al., Earth Planet. Sci. Lett. 302 (2011) 163

[1] *Geology, ETHZ*

CHLORINE-36 DEPTH PROFILE FROM VUE DES ALPES

New information about previous glacial-interglacial periods in Alps

V. Alfimov, S. Ivy-Ochs, P.W. Kubik, J. Beer[1], M. Suter, H.-A. Synal

We have measured ^{36}Cl concentrations in a 100-m long limestone core from Vue des Alpes, Jura Mountains, Switzerland (1256.86 m, 47°4.780N, 6°52.245E) (Fig. 1).

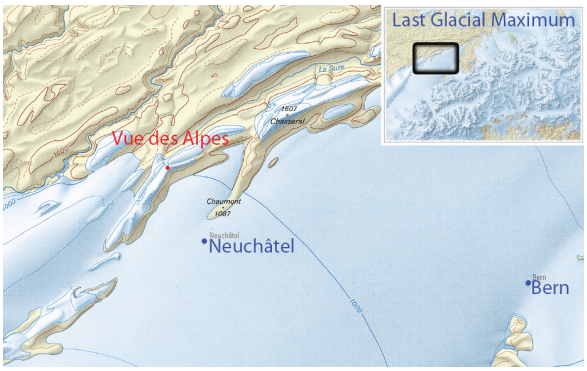

Fig. 1: *The map of the region with the contours of the Last Glacial Maximum (from [1]).*

The measurements were compared with model calculations of cosmogenic ^{36}Cl in the core. The long-lived radionuclide ^{36}Cl ($T_{1/2}$=301 kyr) is produced in limestone by cosmic rays via several pathways of different attenuation length. At the surface the dominant production is spallation of Ca by fast neutrons. Below one meter of rock, slow muon capture on ^{40}Ca starts to take over, while below a depth of 10 m fast muon-induced processes in Ca start to become dominant. The three mentioned processes and the U-Th content of the rock are responsible for the production of thermal neutrons, which can be captured in stable ^{35}Cl contained in the rock to also produce ^{36}Cl. This process is an important pathway for the sampled core, because the stable chlorine concentrations are not negligible (65 ppm on average but varying from 17 to 210 ppm over the whole depth). All pathways were combined in a model of ^{36}Cl production [2]. An exposure scenario with a starting point at the end of the previous major glaciation and including erosion and cover at the surface was optimized to fit the measured profile (Fig. 2).

Our modeling suggests that the Vue des Alpes site was little modified during the Last Glacial Maximum and the last major re-shaping of the landscape happened at Vue des Alpes about 140 kyr ago, when glaciers removed more than 15 m of rock (Fig. 2).

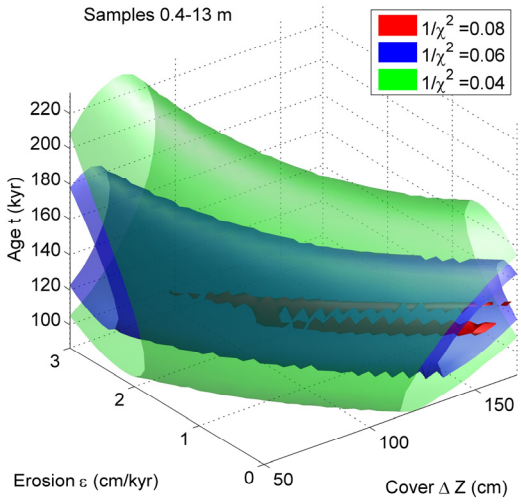

Fig. 2: *The optimization parameter $1/\chi^2$ plotted against time t, erosion rate ε, and cover ΔZ using the muon stopping rate of [3].*

[1] A. Bini et al., Die Schweiz während des letzteiszeitlichen Maximums (2009) ISBN 978-3-302-40049-5

[2] V. Alfimov and S. Ivy-Ochs, Quatern. Geochron. (2009) 462

[3] J.O.H. Stone et al., Geochim. Cosmochim. Acta 62 (1998) 433

[1] *EAWAG, Dübendorf*

POST-DEPOSITIONAL IMPACTS ON 'FINDLINGE'

Implications for surface exposure dating

N. Akçar[1], S. Ivy-Ochs, P.W. Kubik, C. Schlüchter[1]

As the understanding and interpretation of 'numbers' produced on depositional age of an erratic boulder by surface exposure dating is important in the construction of glacial chronology, we have sampled three 'Findlinge' (glacially transported boulders) located on the right-lateral moraine of the Last Glacial Maximum (LGM) Aare glacier in Möschberg, Grosshöchstetten, southeast of Bern, with the aim of shedding light on this topic (Fig. 1).

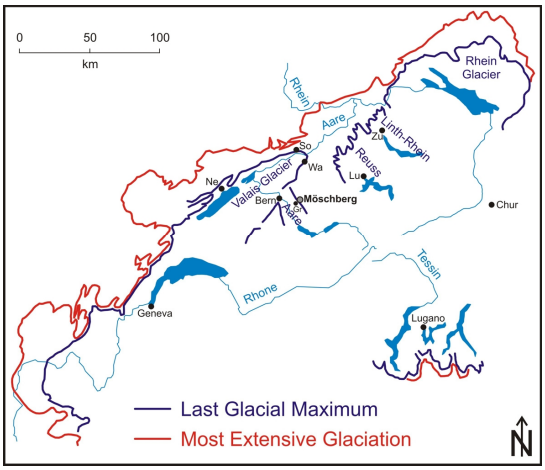

Fig. 1: *Extension of the LGM and the MEG (most extensive glaciation) in the Alps (outline shown). Gr: Grosshöchstetten, Lu: Lucerne, Ne: Neuchatel, So: Solothurn, Wa: Wangen an der Aare, Zu: Zurich [1].*

The boulders have the same depositional, but different post-depositional histories: simple exposure, exhumation and human impact. We measured cosmogenic ^{10}Be concentrations and calculated apparent exposure ages of 13.7±0.5 ka, 18.2±0.9 ka, and 7.2±0.4 ka respectively [1]. The exposure age of the first boulder reflects exhumation. The apparent exposure age of 18.2±0.9 ka (erosion-corrected exposure age: 19.1±1.0 ka) from the second boulder correlates well with the end of the Alpine and global Last Glacial Maximum [1]. The third boulder shows evidence of quarrying as it is surrounded by a rim of excavation material, which is also reflected by the 7.2±0.4 ka apparent exposure age [1]. We modeled the variation of ^{10}Be concentrations with depth down into the sediment in which the first (exhumed) boulder was once buried in, and down into the third (quarried) boulder (Fig. 2).

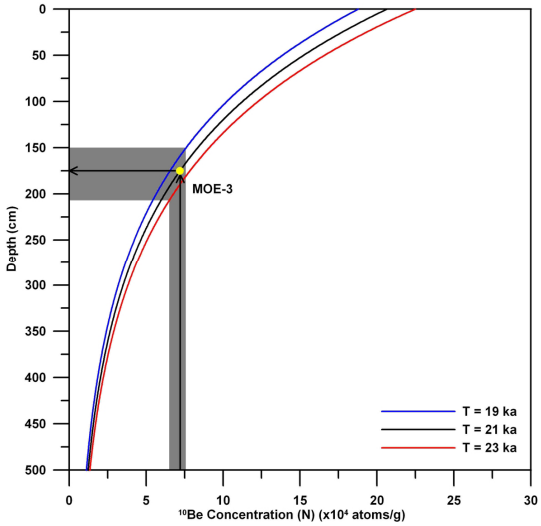

Fig. 2: *Variation of ^{10}Be concentration with depth for sample MOE-3 based on an exposure of 21±2 ka (shaded area) without inheritance with constant erosion at a rate of 3 mm/ka [1].*

We determined that the exhumed 'Findling' was buried in sediment at a depth of around 1 m, and around 2 m of rock was quarried from the third 'Findling'. Our results reveal the importance of sampling for surface exposure dating within a well defined field context, as post-depositional impacts can easily hinder accurate exposure dating of surfaces.

[1] N. Akçar et al., Swiss J. Geosci., submitted

[1] *Geology, University of Bern*

SURFACE EXPOSURE AGES FROM THE GOTTHARD PASS

Reconstructing complex surface exposure using ^{10}Be and *in situ* ^{14}C

K. Hippe[1], S. Ivy-Ochs, F. Kober[1], R. Wieler[1], L. Wacker, P.W. Kubik, V. Alfimov, C. Schlüchter[2]

With the end of the last glaciation a major recession of the Alpine ice masses started. Following the cold early Lateglacial period, a pronounced change towards a warmer climate accompanied by major deglaciation is assumed by ~15 ka (Bølling interstadial) [1]. However, surface exposure ages obtained by cosmogenic ^{10}Be from Alpine bedrock surfaces are often younger. ^{10}Be surface exposure data presented in this study from the Gotthard Pass (Fig. 1), Central Alps, follow this trend suggesting deglaciation as late as ~11.5-8.5 ka (13-9.5 ka with modern snow correction).

Fig. 1: *Bedrock sampling at the Gotthard Pass.*

To detect a possible complex exposure history, we combine the ^{10}Be data with analyses of cosmogenic *in situ* ^{14}C. While short-lived ^{14}C is sensitive to recent surface changes such as surface shielding, the ^{10}Be concentration does not change significantly. Thus, any change in surface exposure will mostly be recorded by an offset between ^{10}Be and ^{14}C exposure ages.

For one location, ~50 m above the pass elevation, the *in situ* ^{14}C age agrees within error with the ^{10}Be age and can be interpreted to record local Lateglacial ice cover. For another location closer to the pass, however, the obtained ^{14}C age is ~2 ka younger than the ^{10}Be age. We have calculated a simple two-stage model showing that the observed concentrations agree well with deglaciation already at ~15 ka when a 1m increase in annual snow cover for the last 5 ka is included (Fig. 2). This assumption is reasonable as Holocene climate reconstructions for the Alps suggest a switch towards a colder climate around 5-4 ka [1].

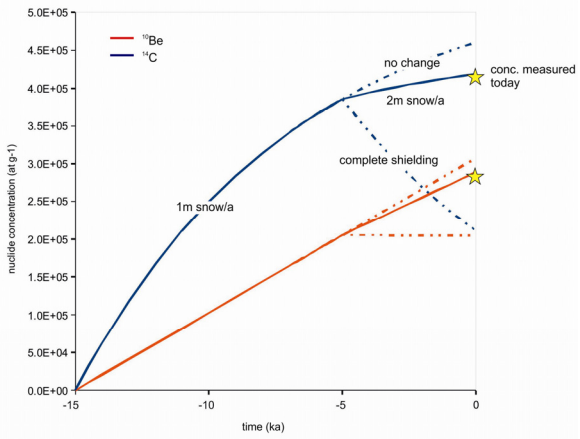

Fig. 2: *Possible deglaciation history for the Gotthard Pass based on paleoclimate reconstructions and the measured ^{10}Be and in situ ^{14}C concentrations. Note that model concentrations for complete shielding starting at 5 ka are also plotted to show that ^{14}C is more affected than ^{10}Be.*

We thus propose that late Holocene climate change can bias cosmogenically derived surface exposure ages towards younger ages due to partial surface shielding by increased snow cover during the last ~5 ka.

[1] S. Ivy-Ochs et al., Quat. Sci. Rev. 28 (2009) 2137

[1] *Geology, ETHZ*
[2] *Geology, University of Bern*

LANDSCAPE DYNAMICS IN THE ALBULA REGION

Numerical and relative dating techniques enable a cross-check

M. Egli[1], R. Böhlert[1], M. Maisch[1], D. Brandová[1], S. Ivy-Ochs[2], P.W. Kubik, W. Haeberli[1]

Moraines and polished bedrocks contain the only direct evidence of past glacier fluctuations. Glaciers are highly sensitive to climate changes. The aim of this study was to improve the understanding of the Lateglacial and early Holocene chronology by dating both glacial (moraines, glacially polished bedrock) and periglacial (rock glacier) landforms using surface exposure dating (^{10}Be) and relative dating methods (Schmidt-hammer rebound values and weathering rind thicknesses) applied to the same landforms [1].

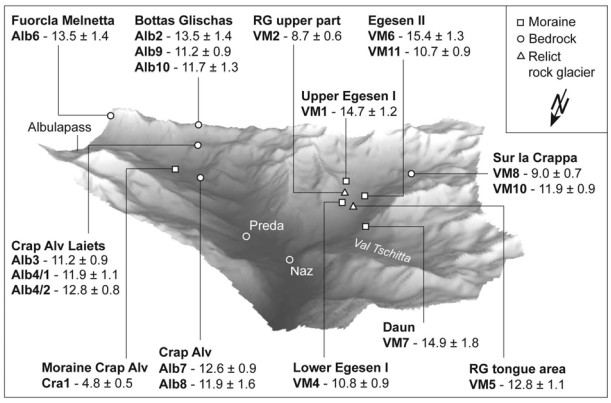

Fig. 1: *Relief with sampling locations and ^{10}Be ages (ka).*

The investigated area includes Val Mulix and the region to the west of Albula Pass in the eastern part of the Swiss Alps. Polished bedrock of a well-pronounced transfluence saddle near the trimline and a roche moutonnée within the former tongue area of the Daun glaciation were investigated in the Albula region. In Val Mulix, numerous landforms (well-preserved moraines and a rockglacier that created a breach into a moraine) from the Lateglacial and the early Holocene time period can be found suggesting several re-advances of glaciers and permafrost activities. Numerical and relative dating techniques provided some new, process-related insights into the landscape evolution. At high-elevation sites near the Last Glacial Maximum (LGM) trimline, ^{10}Be exposure ages of glacially modified bedrock are between 11.2 ka and 13.5 ka (Fig. 1). We expected higher ages, because the chosen sites should have highlighted the timing of the breakdown of the LGM Engadine ice dome. This suggests the persistence of long-lasting, small local ice caps after the breakdown of the LGM ice domes or, alternatively, a reformation of ice perhaps during the Younger Dryas.

In Val Mulix we obtained one of the first ages for the Daun-stadial moraines (14.9±1.8 ka), supporting a pre-Bølling chronological position. The geomorphological situation in Val Mulix is quite complicated. ^{10}Be ages, weathering rind measurements and partially Schmidt-hammer R values from boulders found on a relict rock glacier indicated that the main active phase lasted from the Lateglacial until the early Holocene. Exposure ages from a glacially polished rock barrier, close to the 1850 AD moraine, showed that this area was ice-free at the end of the Younger Dryas (9.0±0.7 ka and 11.9±0.9 ka). Surface exposure dating is, however, limited by several methodological constraints. The choice of suitable snow depths plays a crucial role in the calculation of the ^{10}Be ages and is a potential source of considerable uncertainty. Therefore, the use of different dating methods enables a cross-checking, an extended interpretation of the data and a more accurate estimate of the possible sources of error.

[1] R. Böhlert et al., Geomorph. 127 (2011) 1

[1] *Geography, University of Zurich*
[2] *also Geography, University of Zurich*

LATEGLACIAL AND HOLOCENE GLACIER DYNAMICS

Surface exposure dating of the last glacial – interglacial transition

I. Schindelwig[1], N. Akçar[1], P.W. Kubik, C. Schlüchter[1]

The Alps play a pivotal role for glacier and thus climate reconstructions within Europe. The Belalp and Great Aletsch valleys host adjacent glacier systems that differ strongly in their glacier and catchment size, and also in their level of moraine preservation. They are thus considered an ideal field area to (a) investigate the glacial record and decipher the chronology of complex glacial landsystems during the last glacial - interglacial transition (LGIT), and (b) deduce glacier dynamics in response to climatic forcing or various influences such as geometrical aspects. The contrast in the glacial record is most evident as the Belalp cirque glacier features multiple moraines (Fig. 1), whereas the Great Aletsch valley glacier features apparently only one Lateglacial moraine.

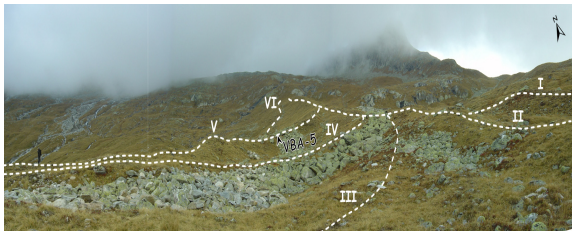

Fig. 1: *Multiple moraines at Belalp valley consecutively numbered (Roman numerals) within the Lateglacial/early Holocene complex. Dashed lines indicate crest-lines. Position of boulder VBA-5 indicated.*

21 cosmogenic 10Be ages (Tab. 1) of boulders from moraines at Belalp constrain up to six individual moraine ridges with weighted mean ages of ~10.9 ka, 11.1 ka, 11.0 ka, and 9.6 ka. They are attributed to the Egesen, Kartell and Schams glacial stadials. Four cosmogenic 10Be ages of boulders and ice-moulded bedrock of the Great Aletsch glacier yield a weighted mean age of ~12.5 ka and thus correlate to the Egesen stadial related to Younger Dryas cooling. The data indicate that during the LGIT glaciers in the Swiss Alps seem to have been significantly affected by rapidly repeating cold climatic conditions initiated during the Younger Dryas and lasting well into Boreal times [1].

Moraine complex	Sample	Ages with related errors (corrections incl. error of the production rate)			
Belalp					
I	VBA-3	13.8	±	0.6	(1.0)
	VBA-22	11.3	±	0.6	(0.8)
	VBA-23	11.4	±	0.8	(1.0)
	VBA-24	10.8	±	0.8	(1.0)
	VBA-25	10.9	±	0.6	(0.9)
	VBA-26	10.0	±	0.7	(0.9)
IV	VBA-6	11.0	±	0.6	(0.8)
	VBA-15	8.7	±	0.8	(1.0)
	VBA-16	11.2	±	0.6	(0.9)
V	VBA-1	12.1	±	0.6	(0.9)
	VBA-2	10.6	±	0.5	(0.8)
	VBA-4	9.2	±	0.6	(0.8)
	VBA-5	10.6	±	0.6	(0.8)
	VBA-11	11.0	±	0.6	(0.9)
	VBA-12	11.6	±	0.7	(0.9)
	VBA-13	10.7	±	0.6	(0.8)
	VBA-14	10.8	±	0.6	(0.8)
VI	VBA-17	9.4	±	0.5	(0.7)
	VBA-18	9.4	±	0.5	(0.7)
	VBA-19	9.6	±	0.5	(0.7)
	VBA-20	9.9	±	0.6	(0.8)
outside	VBA-21	12.8	±	0.7	(1.0)
Great Aletsch site	VBA-7	13.0	±	0.7	(1.0)
	VBA-8	13.2	±	0.6	(0.9)
	VBA-9	11.6	±	0.9	(1.1)
	VBA-10	11.9	±	0.7	(1.0)

Tab. 1: Snow and erosion corrected 10Be exposure ages from moraines in the Belalp and Great Aletsch valleys.

[1] I. Schindelwig et al., J. Quatern. Sci., submitted

[1] *Geology, University of Bern*

ICE-SHEET CONFIGURATION IN THE HIGH ARCTIC

Constraining the timing on Nordaustlandet, Svalbard with ^{10}Be and ^{26}Al

A. Hormes[1], N. Akcar[2], P.W. Kubik

Nordaustlandet is located east of the main island of the Svalbard archipelago, Spitsbergen, and is the northernmost land in the Norwegian sector reaching into the Arctic Ocean. Its fjords and uplands were subject to several glaciations of the Svalbard-Barents Sea ice sheet.

Fig. 1: *View of Murchisonfjord from the north. The red quartzite erratic boulder on the rim (Flora-2) became exposed at 15.4 ± 1.0 ^{10}Be ka and is evidence that the fjord was filled with an actively erosive ice stream during MIS 2.*

We collected 13 surface samples from glacially transported erratic boulders and 6 from bedrock for cosmogenic nuclide dating with ^{10}Be and ^{26}Al (Fig. 1). It is our main objective to reconstruct deglaciation ages and the ice sheet configuration of the last glaciation during Marine Isotope Stage 2 (MIS 2). Only ^{10}Be ages were useful for our interpretations because of unresolved analytical problems with ^{26}Al in this area.

The ^{10}Be exposure ages (Fig. 2) emphasize our present understanding of former ice sheet configurations during MIS 2 in the Arctic with cold-based non-erosive ice domes on higher plateaus and erosive faster flowing ice streams in fjords. Bedrock samples on higher plateaus indicate all a complex glacial and exposure history with apparent ages between 33.3 and 120.3 ka. In addition, several erratic boulders suggest a cover of non-erosive cold-based ice during several periods with apparent ages between 24.7 and 122.8 ka. Also ground-truthed aerial image interpretation confirms this ice sheet configuration with ice-marginal channels left by cold-based ice dome upland of Murchisonfjord. Erosional ice streams were confined to the fjords and lowlands below 200-230 m altitude. They became deglaciated between 13 and 15.4 ka.

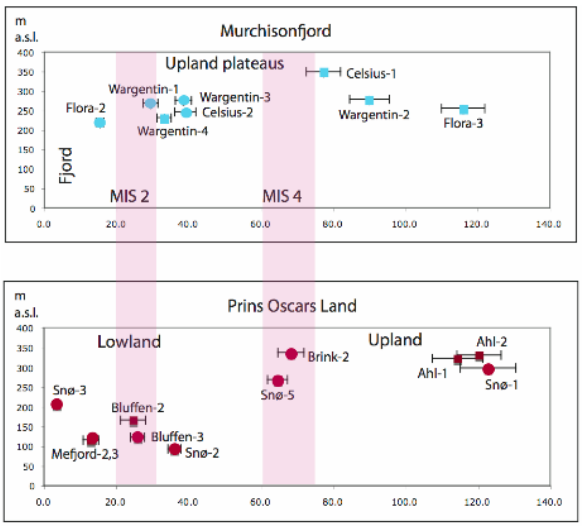

Fig. 2: *^{10}Be exposure age versus altitude plots for the erratic boulders (●) and bedrock (■) in Murchisonfjord and Prins Oscars Land.*

Two erratic boulders indicate deglaciation ages of 64-68 ka and could be interpreted as showing inheritance, but based on lithological studies we are left with the possibility that higher upland areas in Prins Oscars Land were deglaciated after MIS 4 and ice-free during MIS 2 [1].

[1] A. Hormes et al., Boreas (2011) in review

[1] *Arctic Geology, The University Centre in Svalbard, Norway*
[2] *Geology, University of Bern*

GLACIATIONS AT ULUDAĞ MOUNTAIN (NW TURKEY)

Field and cosmogenic exposure dating evidence

N. Akçar[1], V. Yavuz[2], P.W. Kubik, C. Zahno[3], C. Schlüchter[1]

Today's climate in northwestern Turkey is dominated by middle to high latitude westerlies. In addition, it is strongly influenced by the orography of the Anatolian plateau, the Mediterranean, the Aegean and the Black Seas. The interaction of these components results in a complex climate in northwestern Turkey. Quantification of Quaternary climate change in this region plays a key role in the understanding of the moisture transport in the eastern Mediterranean and the circum-Black Sea regions. Quaternary climate can be quantified using the glacial records of Quaternary glaciations in the Uludağ Mountain, which is a northwest-southeast trending fault-bounded mountain (2542 m a.s.l.). The Uludağ Mountain was glaciated in the past, since the landscape is dominated by distinct cirque morphology, glacial deposits and lakes [1, 2] (Fig. 1).

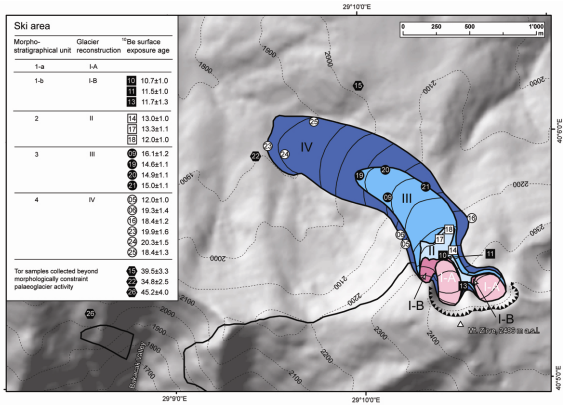

Fig. 1: *Hillshade of western Uludağ displaying glacier reconstructions constrained by geology and ^{10}Be exposure ages (I–IV) [1].*

With the aim of constructing the chronology of Quaternary glaciations in the eastern Uludağ, 92 new samples were collected from erratic boulders, glacially abraded bedrock and tor surfaces for cosmogenic ^{10}Be analysis. ^{10}Be exposure ages show that the glaciers advanced before around 21.2 ka, and continued until around 19.0 ka; then glaciers retreated.

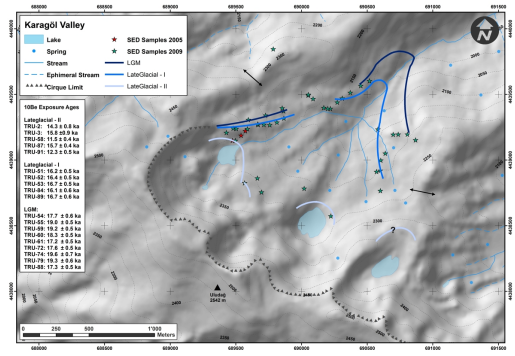

Fig. 2: *Hillshade of eastern Uludağ displaying glacier extensions constrained by geology and ^{10}Be exposure ages [2].*

This advance is synchronous with the last maximum glaciation in other mountains of Anatolia (Eastern Black Sea Mountains, Aladağ Mountains, Dedegöl Mountains, Mount Sandıras and Mount Erciyes), the European Alps, Central Apennines and the Greek Mountains during the global Last Glacial Maximum (21±2 ka) within Marine Isotope Stage 2. During the Lateglacial, the glaciers advanced again no later than around 16.7 ka, around 13.3 ka, and around 11.7 ka. These advances are in good agreement with the Lateglacial *Gschnitz* and *Egesen* advances in the European Alps and document an oscillating glacier retreat in NW Anatolia during Termination-I.

[1] C. Zahno et al., Quat. Sci. Rev. 29 (2010) 1173
[2] N. Akçar et al., in preparation

[1] *Geology, University of Bern*
[2] *Faculty of Mines, Istanbul Technical University, Turkey*
[3] *Louis Ingenieurgeologie GmbH, Weggis*

GLACIAL HISTORY OF THE NORTHWESTERN TIAN SHAN

^{10}Be surface exposure dating in the Anaulgen Valley

I. Roehringer[1], J. Wiesinger[1], A. Ni[2], M. Petrov[2], P.W. Kubik, A. Aldahan[3], L. Zoeller[1], W. Zech[1]

Chronological information about former glaciations in the northwestern Tian Shan occupying the westernmost part of the Himalayan-Tibetan orogen is still sparse. The objectives of our study were (I) to establish a local chronology of the main glacial stages and (II) to investigate the paleoclimatic forcings responsible for the glacier oscillations in this region.

In 2010, we analyzed 17 samples which were collected for ^{10}Be surface exposure dating from granite boulders on top of moraines in the Anaulgen Valley (Fig.1). This valley drains melting water from the Turpakbel Nizhniy Glacier (~ 3700 m a.s.l.) to the south. The recent glacier tongue is at 3260 m a.s.l.. Moraines cover the valley down to 2400 a.s.l. marking several former more extensive glaciations.

Fig. 1: *View looking northeast across lateral and latero-frontal moraines of the Turpakbel Nizhniy Glacier.*

BeO extractions were carried out at the University of Bayreuth and the University of Uppsala. ^{10}Be/^{9}Be ratios were measured at the ETH Zurich TANDEM AMS facility.

Exposure ages from the Anaulgen Valley (Tab. 1) can be assigned to at least three glacial stages. The local Last Glacial Maximum occurred during MIS4/MIS3. More restricted glacier advances occurred during MIS2 and the Late Glacial caused by increasing aridity throughout the region during the last glacial cycle.

sample	^{10}Be exposure ages [ka]	
	Lifton	*Lal/Stone*
uppermost latero-terminal moraine		
AN91	15.0 ± 1.6	15.5 ± 1.5
AN92	14.7 ± 1.7	15.1 ± 1.6
AN93	16.0 ± 1.7	16.7 ± 1.6
recessional moraine		
AN31	17.7 ± 2.0	18.5 ± 1.9
AN32	17.2 ± 2.0	17.9 ± 1.9
AN33	18.6 ± 2.2	19.5 ± 2.2
AN34	15.6 ± 2.0	16.1 ± 2.0
morphologically dominant terminal moraine		
AN61	17.5 ± 1.9	18.2 ± 1.8
AN62	19.0 ± 2.0	19.8 ± 1.9
AN63	15.2 ± 1.6	15.5 ± 1.5
AN64	18.6 ± 2.1	19.5 ± 2.0
dissected latero-terminal moraine		
AN41	23.9 ± 3.0	24.8 ± 2.9
AN44	20.1 ± 3.3	20.6 ± 3.2
highest lateral moraine ridge in the lower valley		
AN111	60.1 ± 6.4	68.1 ± 6.6
AN112	33.5 ± 4.4	36.9 ± 4.5
AN113	45.0 ± 5.3	51.6 ± 5.6
AN114	25.3 ± 2.6	27.2 ± 2.5

Tab. 1: *^{10}Be exposure ages from the Anaulgen Valley calculated with the CRONUS-Earth web-calculator (http://hess.ess.washington.edu) with "Lifton" and "Lal/Stone" scaling. No correction has been made for erosion.*

[1] *Geomorphology, Univ. of Bayreuth, Germany*
[2] *Geology and Geophysics, Tashkent, Uzbekistan*
[3] *Earth Sciences, University of Uppsala, Sweden*

PLEISTOCENE GLACIATION IN THE ARID CENTRAL ANDES

Changes in the tropical circulation and the Southern Westerlies

J. Zech[1], R. Zech[2], P.W. Kubik, H. Veit[1]

The reconstruction of past glacial advances can provide important information about past climate changes. In the arid Central Andes, where glaciers are particularly sensitive to precipitation changes, the timing of glaciation documents alterations in the three main atmospheric circulation systems - the South American Summer Monsoon, the El Niño Southern Oscillation and the Southern Westerlies [1].

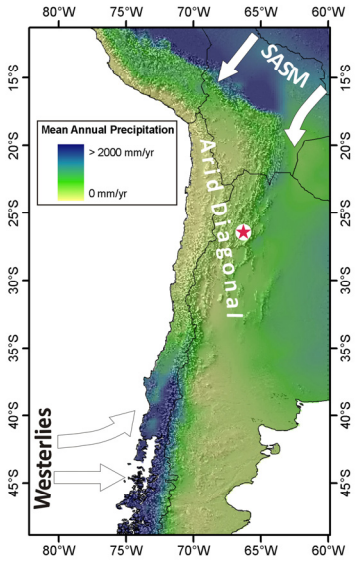

Fig. 1: *Geographic setting of the study area.*

Here we summarize our latest studies in the Sierra de Quilmes (~26°S), NW Argentina mainly based on ^{10}Be surface exposure dating (Fig. 1, 2). Our results show that glaciers advanced in phase with the global Last Glacial Maximum (LGM) at 25.8±0.8 ka and during the Lateglacial at 13.5±0.5 ka and 12.8±0.5 ka, which is in agreement with earlier results [2]. Glacier climate modeling reveals that the Lateglacial advances were favored by massive precipitation increases combined with temperature depressions of -1.4 to -5.4°C. The Lateglacial moisture conditions can be explained with enhanced upper tropospheric easterlies in response to intensified tropical circulation and cooler sea surface temperatures in the eastern Pacific.

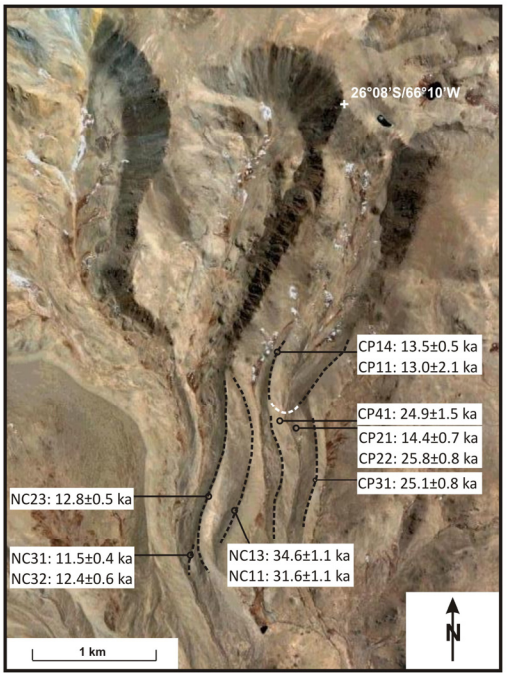

Fig. 2: *Ages calculated with the CRONUS-Earth web calculator (http://hess.ess.washington.edu) applying the Lifton scaling model.*

The oldest dated moraine documents a pre-LGM advance at 34.6±1.1 ka that coincides with glaciations in northern Chile (~30°S) and Central Argentina (~39°S), which record increased precipitation from the Southern Westerlies. Our new data therefore suggest that the Southern Westerlies might have played an important role for moisture advection and paleoglaciation as far north as 30°S.

[1] R. Zech et al., J. Quat. Sci. 6-7 (2008) 635
[2] J. Zech et al., Palaeo3 284 (2009) 180

[1] *Geography, University of Bern*
[2] *Geology, ETHZ*

GLACIATION HISTORY OF QUEEN MAUD LAND

Al-26 surface exposure dating near the Wohlthat Massif, Antarctica

H. Wiesel[1], G. Delisle[2], B. Kuczewski[1], P.W. Kubik

Quartz rich samples for surface exposure dating were taken during the 2007 BGR-expedition "Queenmet" at two Nunataks south-east of the Wohlthat Massif in Queen Maud Land, Antarctica. Rock exposure ages for the Wohlthat Massif itself based on ^{26}Al and ^{10}Be measurements at the AMS facility in Zurich were already presented by Altmaier et al. [1]. Their data suggest that the regionally highest mountain summits have been above the ice surface since at least 1 - 4 Ma ago. The elevation of the ice sheet in the Wohlthat Massif was generally 200 - 400 m higher than today until about 0.5 Ma ago. Our new results for the exposure of rock surfaces on two Nunataks summits at the edge of the Polar Plateau approx. 100 km south-east of the Wohlthat Massif (Fig. 1) help to determine, to which extent the results from the Wohlthat Massif are of regional significance.

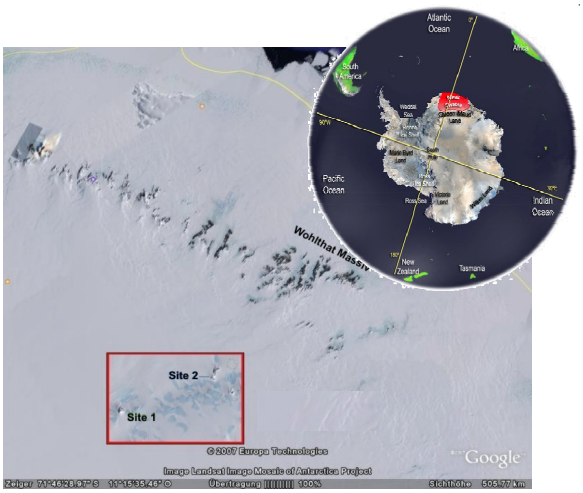

Fig. 1: *Sample location (Site 1: HWAP 1-6; Site 2: HWAP 7-10), 100 km south-east of the Wohlthat Massif.*

Our data suggest that the peak of the outcrop at Site 1 emerged out of the ice about 1.9 Ma ago. Subsequent mountain uplift or reduction in ice thickness or both factors caused the main mass of both outcrops to emerge about 0.7 to 0.5 Ma ago. This result correlates well with the interpretation of the glaciation history for the Wohlthat Massif presented by Altmaier et al. [1]. The data indicate in addition a complex reburial and exposure history for all samples. The analysis of the Be-10 data is still pending.

Sample Name	Latitude (S)	Elevation (m)	Age (Ma)
HWAP 1	72°21.248	2534	0.28
HWAP 3	72°21.616	2652	0.71
HWAP 4	72°21.477	2606	1.86
HWAP 6	72°21.458	2530	0.01
HWAP 5	72°21.279	2510	0.39
HWAP 7	72°13.685	2316	0.48
HWAP 8	72°13.695	2333	0.48
HWAP 9	72°13.722	2347	0.39
HWAP 10	72°13.742	2368	0.51

Tab. 1: *Preliminary ^{26}Al exposure ages of the samples collected at Site 1 and 2.*

[1] M. Altmaier et al., Polar Science 4, Issue 1 (2010) 42

[1] *Nuclear Chemistry, University of Cologne, Germany*
[2] *Georisk Division, BGR Hannover, Germany*

EROSION RATES FROM DEGRADED MOUNTAIN BASINS

Contrasting modern and Holocene erosion rates in Southeast Spain

V. Vanacker[1], N. Bellin[1], N Sougnez[1], R. Ortega Perez[1], P.W. Kubik

In Europe, southeastern Spain was identified as one of the regions with a major threat of desertification in the context of future land use and climate change (Fig. 1). Since erosion processes are related to both human and climatic components, it is important to analyze these processes in their time-space context [1].

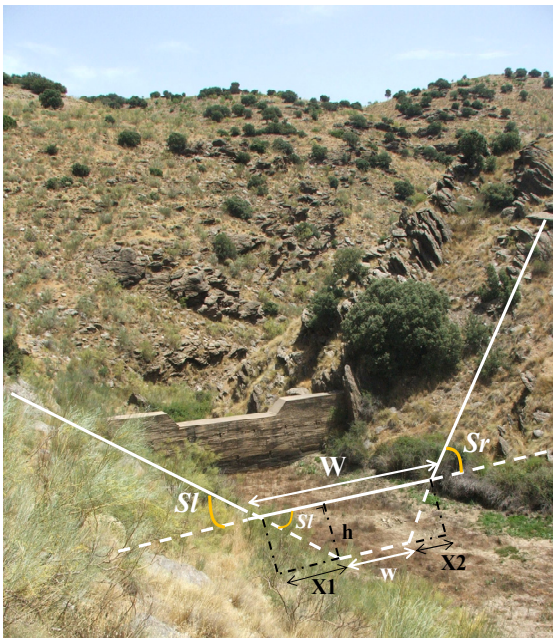

Fig. 1: *Highly degraded mountain site in the Spanish Betic Cordillera. Illustration of the methods used to quantify modern basin-wide erosion rates.*

For 15 small river basins in the Spanish Betic Cordillera, we derived basin-wide denudation rates from ^{10}Be concentrations of river-borne sediment. Modern erosion data were quantified through analysis of sediment deposition volumes behind check dams for 36 basins. They represent average erosion rates over the last 10 to 50 years [2].

Spatially averaged ^{10}Be basin-wide denudation rates vary between 20 and 400 mm/ky, and integrate over the last 2000 to 25000 years (Fig. 2). Modern basin-wide erosion rates are surprisingly low given the degraded aspect of the environment (mean 54 mm/ky; median 23 mm/ky, Fig. 2).

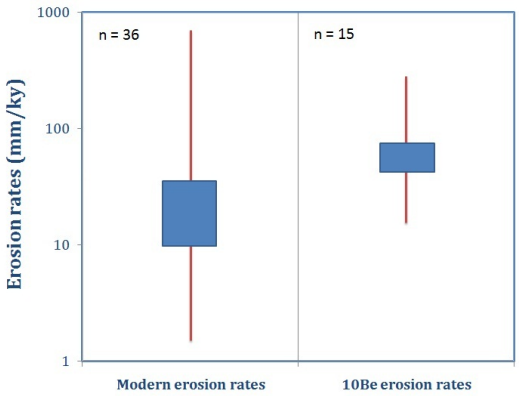

Fig. 2: *Modern and cosmogenically derived basin-wide erosion rates for the Betic Cordillera.*

Our data from mountain basins in the Betic Cordillera show that modern erosion rates are of the same order of magnitude as time-integrated erosion rates for the Holocene. The human impact on erosion rates remains difficult to be quantified in this dynamic environment where major shifts occurred in vegetation cover, climate, erosion, and human occupation during the last 12 ky. The present-day landscape is the result of a long occupation history where past human disturbances strengthened or buffered natural climatic shifts.

[1] L. Reinhardt et al., Earth Surf. Proc. Landf. 35 (2010) 78
[2] N. Sougnez, B. Van Wesemael and V. Vanacker, Catena 84 (2011) 1

[1] *Earth and Life Institute, University of Louvain, Louvain-la-Neuve, Belgium*

^{10}Be BASED SEDIMENT PRODUCTION IN THE AMAZON

Cosmogenic ^{10}Be and recent river loads decipher sediment transport

H. Wittmann[1], F. von Blanckenburg[1], L. Maurice[2], J.L. Guyot[3], N. Filizola[4], P.W. Kubik

Sources and sinks of sediment within the world's largest fluvial system, the Amazon basin, were investigated using cosmogenic ^{10}Be and published modern sediment loads from river gauging. Modeling of nuclide concentration changes during floodplain sediment transfer [1] and testing the effects of storage on ^{10}Be concentrations in a large Amazon tributary [2] have shown that this method allows calculating erosion rates in depositional basins despite intermediate sediment storage, with the result that fluxes of the sediment-producing hinterland can now be linked to those discharged at the basins´ outlet.

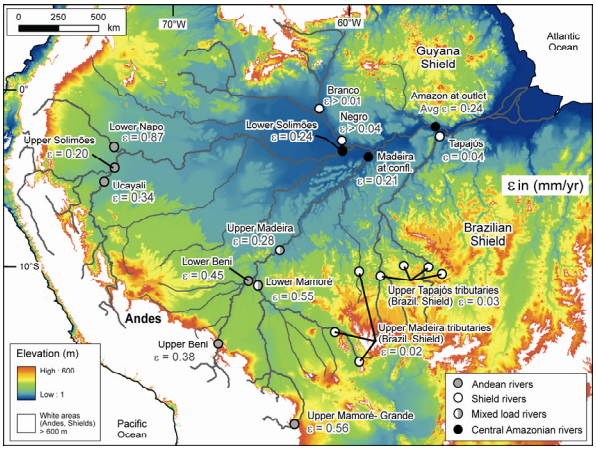

Fig. 1: *^{10}Be-based erosion rates in the basin*

In order to derive a cosmogenic nuclide-based sediment budget for the Amazon basin, we sampled the sediment source areas (Andes, Guyana and Brazilian Shields) and the central lowlands. In rivers of central Amazonia, sediment of finer grain sizes (125-500 µm) yields a cosmogenic nuclide-based erosion rate ε of 0.24±0.02 mm/yr that is comparable to the rate of all main Andean-draining rivers (0.37±0.06 mm/yr), the Beni, Napo, Mamoré, Ucayali, and upper Solimoes rivers (Fig. 1). Coarser-grained sediment (>500 µm) of central Amazonian rivers is indicative of a source from the tectonically stable cratonic headwaters of the Guyana and Brazilian Shields, for which the ^{10}Be-based erosion rates are low at 0.01-0.02 mm/yr.

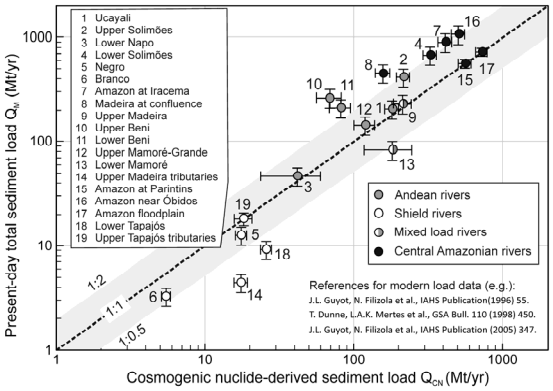

Fig. 2: *Modern vs. cosmogenic-derived loads*

These rates can be converted to sediment loads (Mt/yr). For the Amazon outlet at Óbidos, a sediment production rate of ~610 Mt/yr results. Non-Andean source areas contribute only ~45 Mt/yr. Our cosmogenic-derived rates compare well with published loads (see Fig. 2); they compare best in the lowlands and show larger scatter for sediment-source areas. We attribute this similar trend in cosmogenic vs. modern sediment loads to the buffering capability of the Amazon floodplain and to the absence of long-term sediment storage in the basin.

[1] H. Wittmann, F. von Blanckenburg, Geomorph. 109 (2009) 246

[2] H. Wittmann et al., Earth Planet. Sci. Lett. 288 (2009) 463

[1] *Mineralogy, University of Hannover (now GFZ Potsdam), Hannover, Germany*

[2] *IRD Toulouse & Univ. Paul Sabatier Toulouse, France*

[3] *IRD Lago Sul, Brazil*

[4] *University of Amazonas, Manaus, Brazil*

COSMOGENIC EROSION RATES ACROSS THE ANDES

Strong coupling of denudation rates to mean precipitation rates

F. Kober[1], K. Hippe[1], G. Zeilinger[2], S. Ivy-Ochs, P.W. Kubik

The Central Andes of northern Chile and western Bolivia resemble a mountain belt with high relief (Fig. 1), a large internally drained plateau (the Altiplano) and a huge contrast in precipitation rates that leads to hyperarid condition on the Western Escarpment, arid to semihumid conditions in the Western Cordillera and Altiplano region and humid conditions for the Eastern Cordillera and the Andean Foreland.

We present here a compilation of catchment averaged ^{10}Be denudation rates obtained at ETH and complement those with additional data from other sources (Fig. 1).

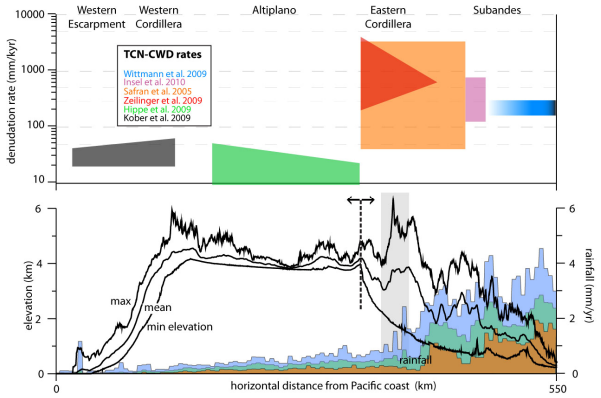

Fig. 1: *Morphology, rainfall distribution and catchment wide denudation rates [1-6] obtained from cosmogenic nuclide ^{10}Be analysis*

From Fig. 1 we see that precipitation and denudation rates are strongly coupled. Denudation rates increase only slightly with elevation in the Western Escarpment and Cordillera region and are complexly exposed (in a contemporaneous analysis of ^{26}Al and ^{21}Ne) due to storage in the lower river course [3], remain constant but low in the Altiplano region and suddenly increase by 2 to 3 orders of magnitudes when the impinging high rainfall rates and the strong relief contrasts of the Eastern Cordillera are approached.

While rainfall is strongly orographically controlled and moisture source dependent (Amazon basin), the denudation rates follow this pattern. Denudation rates are integrated over 20-100 ky for the Western Escarpment and Altiplano region, however rates from the Eastern Cordillera only integrate over millennial time-scales. Nevertheless shorter term sediment yield data and long-term denudation rates of similar magnitudes suggest that this pattern of precipitation and denudation rates must have prevailed at least back into the Pliocene.

Analyzing the studied sites individually suggested that a more complex denudation rate pattern exists with significant storage signals west of the precipitation divide and episodic processes east of the divide - signals only resolved with multiple cosmogenic nuclides. Thus the pacing of denudation rates with precipitation rates is predominantly true only for the comparison of the large scale morphotectonic units.

[1] K. Hippe et al., in preparation
[2] N. Insel et al., Geomorph. 122 (2010 65
[3] F. Kober et al., Earth Surf. Proc. Landf. 34 (2009) 398
[4] E. Safran et al., Earth Surf. Proc. Landf. 30 (2005) 1007
[5] H. Wittmann et al., Earth Planet. Sci. Lett. 288 (2009) 463
[6] G. Zeilinger et al., in preparation

[1] *Geology, ETHZ*
[2] *Geology, University of Potsdam, Potsdam, Germany*

CORRELATION OF MAKRAN FLUVIAL TERRACES (IRAN)

Interaction between surface processes and tectonics in the Makran

N. Haghipour [1], F. Kober[1], J-P. Burg[1], G. Zeilinger[2], S. Ivy-Ochs, P.W. Kubik

The driving forces and genesis of the Quaternary sequences covering the Makran accretionary wedge require detailed studies for a better understanding of the contribution and feedback of surface processes to the growth of the wedge (Fig. 1). For this purpose, temporal and spatial correlation of fluvial and alluvial sequences are investigated to document recent uplift rates and answer whether the Makran accretionary wedge has reached a steady state (critical taper) with a uniform uplift pattern and incision rate distribution.

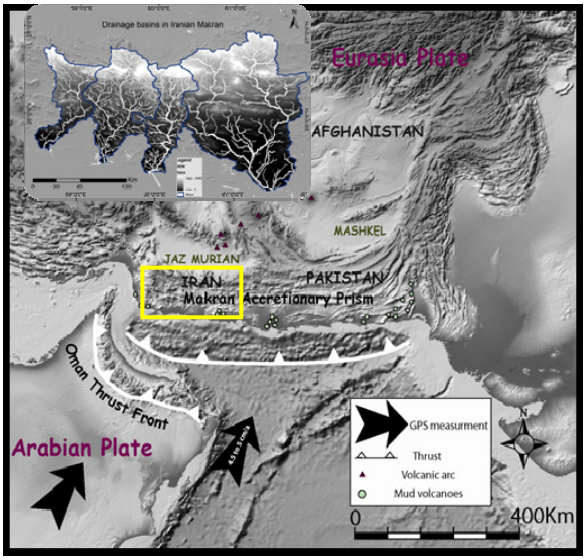

Fig. 1: *Tectonic setting of Makran accretionary wedge. The box indicates the four studied catchments.*

We investigated four main catchments, where several levels of terraces are preserved. The preliminary ^{10}Be ages provide a large variety of abandonment ages of the underlying bedrock strath of these terraces. They are in the range of 220 ka and 17 ka with oldest ages in the east.

The results illustrate a strong correlation of terraces in western catchments compared to the eastern ones, where they apparently experienced less tectonic influence. Based on ^{10}Be exposure ages the abandonment of the two preeminent terraces are ca. 90 ka and 21 ka in the western part of the study area, whereas the abandonments ages in the eastern part vary between 218 ka and 28 ka and make regional correlation difficult.

These ages imply a uniform, average fluvial incision rate of 0.5 mm/a throughout Pleistocene times. There is a marked change in incision rate (0.9 mm/a) where the rivers cut across a regional streak of folds. These preliminary results differ from previous work on marine terraces, which documented 0 to 0.2 mm/a uplift rate in Pleistocene times along the coastal Makran.

The temporal difference of terrace abandonment between eastern and western catchments suggests that the Makran accretionary wedge experienced different deposition, incision and tectonic histories during the Pleistocene.

[1] *Geology, ETHZ*
[2] *Geosciences, University of Potsdam, Potsdam, Germany*

THE RISE OF THE EASTERN ALPS

Can ^{10}Be disentangle climate, lithology and tectonics in the landscape?

K.P. Norton[1], F. von Blanckenburg[2], R. DiBiase[3], F. Schlunegger[1], P.W. Kubik

In this study, we measured ^{10}Be-derived basin-averaged denudation rates of 170 to 1400 mm ky^{-1} in the Eastern and Southern European Alps. These rates are similar to those from the Central Alps for similar lithologies (Fig 1). We present the new rates together with a detailed topographic analysis in order to infer the forces driving erosion.

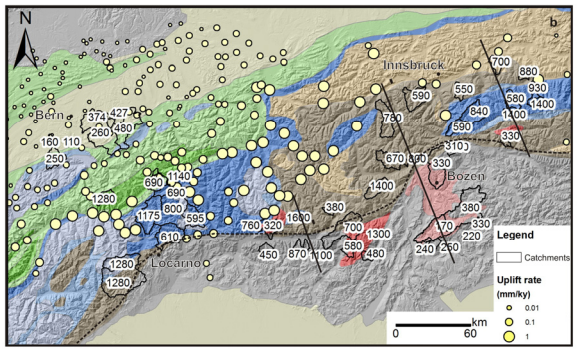

Fig. 1: *Denudation rates and rock uplift rates (mm/ky) across the Eastern and Central Alps.*

Denudation rates in the Eastern and Southern European Alps vary considerably between different lithologies, with higher variability for steeper landscapes. In addition, correlations with topographic metrics become poorer as landscapes steepen. Clear relationships between rock type, denudation rate, and basin morphology are not apparent. For instance, resistant rocks such as Tertiary volcanics and pre-Alpine gneisses both exhibit steep slopes, but the former have low denudation rates and the latter have high denudation rates. We suggest that the major factor controlling erosion in this setting is geomorphic preconditioning. This preconditioning is primarily related to large erosive glaciers in the late Quaternary. The Eastern Alps do not display strong correlations as seen in the Central Alps because the glaciers there were more diffuse and therefore less effective in priming landscapes for erosion. However, there are also distinct differences in tectonic evolution between the Eastern and Central Alps. This enhances the differences in their geomorphic response. In particular, the Eastern Alps are subject to an ongoing tectonic influx. The result is that denudation rates in the Eastern Alps are generally lower than preliminary rock uplift data, indicating the potential for surface uplift in the Eastern and Southern European Alps (Fig 2).

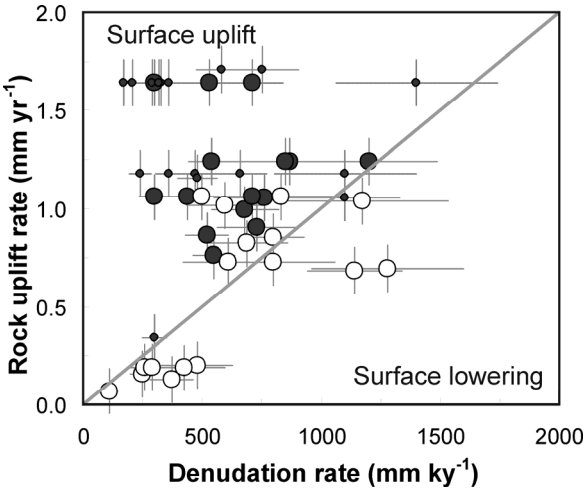

Fig. 2: *Rock uplift rate plotted against denudation rate for the Eastern (filled) and Central (open) Alps indicate relief growth in the Eastern Alps.*

[1] K.P. Norton et al., Intern. J. Earth Sci. (2011) in press

[1] *Geology, University of Bern*
[2] *German Geoscience Research Center (GFZ), Potsdam, Germany*
[3] *SESE, Arizona State University, Tempe, USA*

^{36}Cl EXPOSURE DATING OF LANDSLIDES IN TRENTINO

Assessing regional hazards based on magnitude-frequency data

S. Ivy-Ochs, S. Martin[1], P. Campedel[2], V. Alfimov, E. Andreotti[3], A. Vigano[4], G. Carugati[3]

In the Trentino province of northeastern Italy there are numerous large landslide and rock avalanche deposits, notably in valleys that are densely inhabited. For example, in the Adige River valley, the towns of Trento and Rovereto were built on rock avalanche deposits derived from the collapse of the Marzola and Zugna Mountains, respectively.

Recent applications of cosmogenic radionuclide surface exposure dating to rock avalanche deposits have shown that cosmogenic geochronology can be an important tool for evaluating the geological risks involving inhabited mountainous regions. Geochronological data obtained by exposure dating boulders and scarp area bedrock provide fundamental information necessary for calculation of the return time of slope collapses or other detachment events.

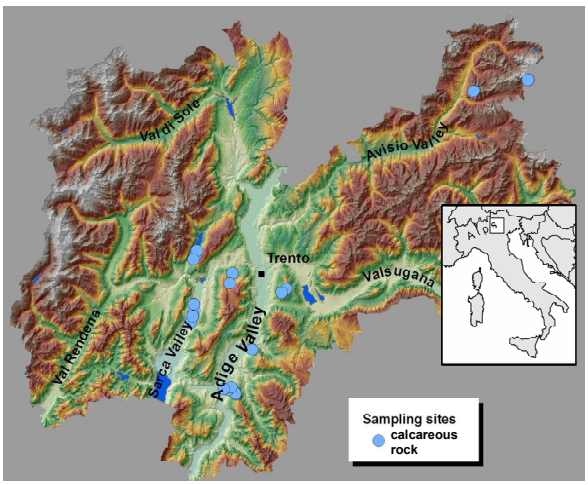

Fig. 1: *Shaded-relief DEM showing ^{36}Cl surface exposure dating sample sites of mass movements in Trentino.*

To this end we are studying several Trentino landslides (Fig. 1), which include i) the Marzola deep gravitational slope movement; the Castelpietra, Lavini di Marco, and Monte Palone rock avalanche deposits in the Adige valley, ii) the Marocche di Dro (Fig. 2) and the Molveno deposits in the Sarca valley, and neotectonic features at the foot of the Vallaccia peak in the Avisio valley. Boulders and bedrock from these rock avalanche and landslide deposits, made of dolomite, marly limestone and massive limestone, have been exposure dated with ^{36}Cl.

Fig. 2*: Bouldery deposits of the Marocche di Dro rock avalanche; postulated scarp in the background.*

Preliminary ^{36}Cl results agree well with historical records and provide support for the hypothesis of repeated activation of the slopes at many of these sites, often dramatically, during historic time.

[1] *Geosciences, Università di Padua, Padua, Italy*
[2] *Servizio Geologico della Provincia di Trento, Trento, Italy*
[3] *INFN, Università dell'Insubria, Como, Italy*
[4] *Engineering, Università di Trento, Trento, Italy*

DATING OF LANDSLIDES IN THE KYRGYZ TIEN SHAN

^{10}Be exposure ages from granitic boulders of river-blocking landslides

K. Sanhueza-Pino[1], O. Korup[2], R. Hetzel[1], H. Munack[2], J.T. Weidinger[3], S. Dunning[4], C. Ormukov[5], P. Kubik

Numerous large landslides occur in the tectonically active Tien Shan. However, their significance in Quaternary landscape evolution and natural hazard assessment remains unresolved. We determined ^{10}Be exposure ages for three prominent (>10^7 m^3) river-blocking bedrock landslides in the Kyrgyz Tien Shan. Several samples were obtained from each landslide from granitic boulders located on the highest parts of the deposits (Fig. 1) [1].

Fig. 1: *Granitic boulder on top of the Aksu landslide, from which sample 08K8 was taken.*

For two of the landslides (Alamyedin and Aksu) ^{10}Be ages fall into a narrow age interval. Samples from the Alamyedin rockslide (42°37'N, 74°40'E) yield ^{10}Be ages of 14.7–7.3 ka (Tab. 1). Except for the youngest age (sample 08K11), these are consistent with calibrated ^{14}C ages of 11.7 ± 0.9 ka and 13.6 ± 0.6 ka BP, which we obtained from gastropod shells in loess-flow deposits overlying the landslide debris. We conclude that the Alamyedin landslide formed between 15 and 11 ka.

Three boulders of the very large (~10^9 m^3) Aksu landslide (42°32'N, 73°59'E) yielded ^{10}Be ages between 67.1 and 63.0 ka. A fourth boulder gave a younger age of ~34 ka (Tab. 1), which may have been caused by recent block tilting. The data indicate that the Aksu landslide is among the oldest documented bedrock landslides in semi-arid continental interiors.

Blocks from the Ukok landslide (42°6'N, 75°54'E) yielded more variable ^{10}Be ages (not shown in Tab. 1) which may indicate multiple events. Presumably, a major part of the landslide was deposited in the early to mid-Holocene [1].

Sample ID	Length of boulder	Dip angle (°)	^{10}Be age (ka)[a]
Alamyedin landslide			
08K11	5.5	25	7.3 ± 0.4
08K12	3	25	11.3 ± 0.5
08K13	3	30	12.8 ± 0.8
08K14	3.5	15	14.7 ± 0.6
Aksu landslide			
08K7	4	10	67.1 ± 3.8
08K8	4.5	5	66.5 ± 2.1
08K9	6.5	45	63.0 ± 2.1
08K10	4	40	34.1 ± 1.6

[a] Ages (1σ internal errors) were calculated with CRONUS-Earth webcalculator, (http://hess.ess.washington.edu) assuming no erosion and using the time-dependent Lal/Stone scaling scheme.

Tab. 1: *^{10}Be exposure ages of granitic boulders from two landslides in the Kyrgyz Tien Shan.*

The landslides deposits studied here have not been reworked by glaciers, hence their locations and ages mark maximum extents and minimum ages of glacial advances, respectively. Thus, landslide deposits may provide valuable constraints for glacial advances in landscapes where glacial sediments are poorly preserved.

[1] K. Sanhueza-Pino et al., Quatern. Res., submitted

[1] *Geology & Paleontology, University of Münster, Münster, Germany*
[2] *Earth and Environmental Sciences, University of Potsdam, Potsdam, Germany*
[3] *Erkudok Institute, Gmunden, Austria*
[4] *Division of Geography, Northumbria University, Newcastle, UK*
[5] *Institute of Seismology, Bishkek, Kyrgyz Republic*

^{36}Cl EXPOSURE DATING OF PALAEO-EARTHQUAKES

First results from the western Anatolian Extensional Province, Turkey

N. Akçar[1], D. Tikhomirov[1], Ç. Özkaymak[2], V. Alfimov, S. Ivy-Ochs, H. Sözbilir[2], B. Uzel[2], C. Schlüchter[1]

Based on historical and instrumental data, societies in the Eastern Mediterranean and Middle East survived at least 150 large earthquakes (generally M > 6) during the last 2500 years, which have resulted in the deaths of many thousands of people and caused economic devastation [1]. As the only remaining evidence of seismic activity is the bedrock scarp, cosmogenic ^{36}Cl is a suitable nuclide to be applied in the determination of the seismic history and slip rate of an active fault plane [2]. In this study, we focus on the 4 m high exposed Mugırtepe fault scarp within the active Manisa Fault Zone of western Anatolia [3] (Fig. 1).

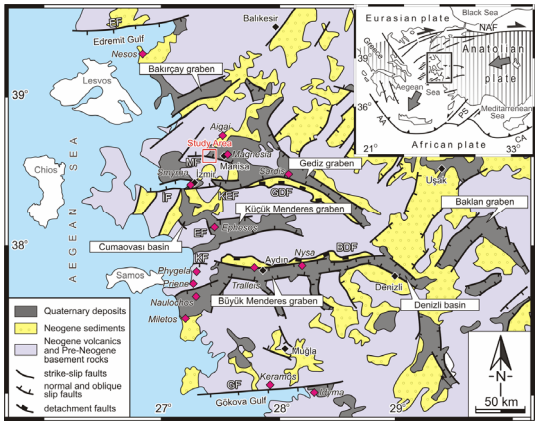

Fig. 1: *Simplified geological map showing major structural elements and the Neogene-Quaternary deposits in the western Anatolia [2].*

We analyzed 42 samples for cosmogenic ^{36}Cl in two slightly overlapping strips covering a total height of 2.65 m of the fault scarp. The measured ^{36}Cl concentrations suggest 4 events, with displacements of 0.50, 0.30, 0.95, and 0.90 meters [2] (Fig. 2). In order to analyze the timing and the length of the paleoseismic events, we applied the Schlagenhauf Matlab® code [4]. This yielded two scenarios, one with 2 seismic events at 13.7 ± 0.8 ka with a 0.5 ± 0.2 m displacement and at 7.8 ± 0.5 ka with a 2.15 ± 0.35 m displacement. The second scenario yields one event with a 2.65 ± 0.35 m displacement at 8.6 ± 0.6 ka.

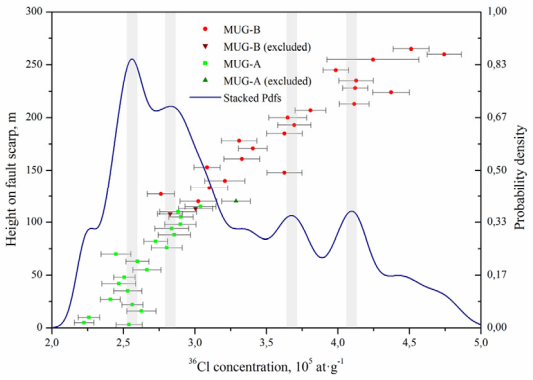

Fig. 2: *Measured ^{36}Cl concentration with 1σ error bars versus height on the scarp and stacked probability density functions [2].*

These results indicate that the first surface faulting at Mugırtepe occurred not later than around 14 ka and seismic activity continued until around 8 ka. Unfortunately, earthquakes which caused this slip on the fault scarp cannot be resolved by this code due to its detection limits of ±20 cm and ±500 a [4].

[1] N.N. Ambraseys and J.A. Jackson, Geophys. J. Int. 133 (1998) 390
[2] N. Akçar et al., in preparation
[3] C. Özkaymak et al., Turk. J. Earth Sci. (2011) in press
[4] A. Schlagenhauf et al., Geophys. J. Int. 182 (2010) 36

[1] *Geology, University of Bern*
[2] *Dokuz Eylül University, Izmir, Turkey*

ANCIENT QUARRIES IN WESTERN TURKEY

Cosmogenic ^{10}Be exposure dating

E. Haudenschild[1], N. Akçar[1], V. Yavuz[2], S. Ivy-Ochs, V. Alfimov, P.W. Kubik, C. Schlüchter[1]

Kestanbol Granite quarries located near the Ezine village of Çanakkale, northwestern Turkey (Fig. 1), have been operated for the production and export of building stones since ancient times. It is known that the Romans were trading the Kestanbol Granite (known to the Romans as Marmor Troadense) all over the Mediterranean region [1]. The building stones produced vary from pavement stones to 11 meters long columns (Fig. 2). Today, remnant building stones can still be found in the ruins of these quarries, whose extent and operation periods are unknown, although archaeologists roughly estimate a Roman period from 500 BC to 500 AD [2]. Such vague limitation makes it impossible to understand both the development in time of the exploitation area and the historical and political context of the quarrying [2].

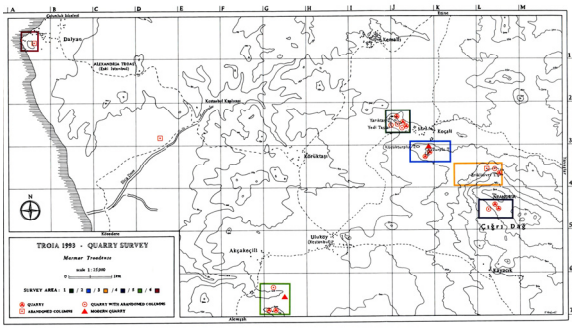

Fig. 1: *Map of the approximate areal distribution of the Kestanbol Granite quarries in northwestern Turkey [2, 3].*

Can cosmogenic ^{10}Be help to constrain the chronology of quarrying in this area? The aim of our study is therefore to first determine the extent of the Roman working area and then to date the operation periods of antique quarries by applying ^{10}Be surface exposure dating. To achieve this, 27 samples from the quarries, building stones and bedrock were collected after detailed field mapping [3] (Fig. 1).

Fig. 2: *Ancient Roman quarry "Yedi Taşlar" near Koçali [3].*

According to our first ^{10}Be results from bedrock samples, the landscape surface in the study area is at least 130 ka old. The exposure ages of the worked steps vary from 4 ka to 10 ka. These are significantly older than expected ages based on archaeological data. Therefore, our measured nuclide concentrations contain a significant amount of inheritance. We sampled a recently abandoned quarry nearby to model the variation of ^{10}Be with depth in order to gauge the amount of inherited cosmogenic ^{10}Be.

[1] L. Lazzarini, Bollettino d'Arte Suppl. 41 (1987) 157
[2] G. Ponti, Studia Troica 5 (1995) 291
[3] E. Haudenschild et al., in preparation

[1] *Geology, University of Bern*
[2] *Istanbul Technical University, Istanbul, Turkey*

ICE/RAIN AND OCEAN SAMPLES

Radiocarbon dating of an Andean ice core

The Laschamp event in the NGRIP ice core

^{7}Be and ^{10}Be in precipitation in Switzerland

Chlorine-36 in rain and cave dripping waters

Sedimentation rates in the Arctic Ocean

Beryllium-10 production from marine records

Past water mass mixing in the SW Indian Ocean

Uranium-236 in the Atlantic Ocean

Anthropogenic Uranium-236 in the North Sea

Long-lived radionuclides at Bikini Atoll

RADIOCARBON DATING OF AN ANDEAN ICE CORE

Age-depth relation at Nevado Illimani supplemented by new ^{14}C dates

A. Zapf[1,2], L. Wacker, S. Szidat[2], M. Schwikowski[1,2]

In paleoclimatological investigations of ice cores from high-alpine glaciers dating is a non-trivial task mainly due to the complex glaciological impacts resulting in a strongly non-linear age-depth relationship. Particularly in the deepest parts of the ice core where thinning of the annual layers does not allow for conventional annual-layer counting on seasonally varying parameters, other techniques are needed to establish precise age-depth models indispensable for paleoclimate reconstructions.

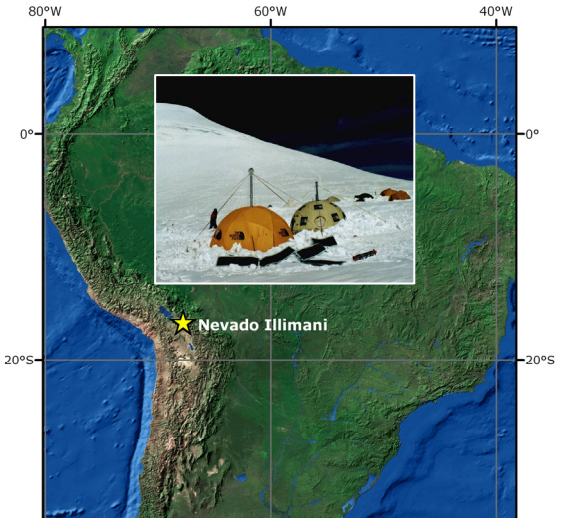

Fig. 1: *Location of the drilling site in the Bolivian Andes (insert: drilling camp at 6300 m).*

During the last years intensive analyses on an ice core from Nevado Illimani (drilled in 1999, Fig. 1) have been carried out in our group. A recent publication on this core deals with a new approach to reconstruct regional temperatures based on ammonium concentrations [1]. In order to draw meaningful conclusions from such an approach a well-established age-depth relationship is of the utmost importance.

Radiocarbon dating of carbonaceous particles embedded in the ice matrix using the MICADAS AMS system proved to be an appropriate tool to retrieve age information from the ice not accessible with common dating techniques [2].

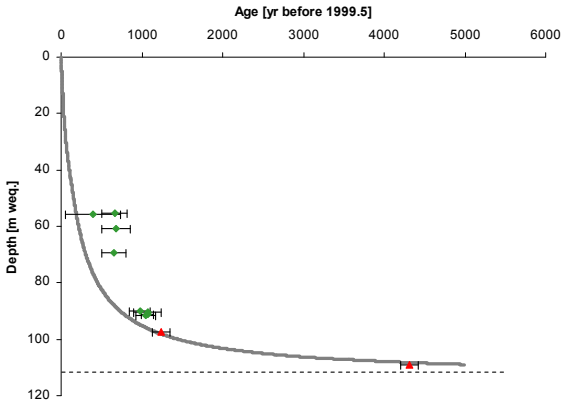

Fig. 2: *Age-depth relation of the Nevado Illimani ice core. The grey curve represents the output of a two-parameter model using volcanic horizons with ^{14}C dates (red triangles) as time markers. Eight independently measured ^{14}C dates are shown as green diamonds.*

Four samples were measured between 89.3 and 91.4 mwe containing and surrounding the ice-layer with the "unknown 1258" volcanic eruption. These show a very high consistency amongst each other and match the two-parameter model fairly well. ^{14}C dates from around 55 to 70 mwe show an offset of roughly 150 to 300 years compared to the fitted two-parameter model (Fig. 2).

[1] T. Kellerhals et al., J. Geol. Res. 115 (2010) D16123
[2] T. Jenk et al., J. Geol. Res. 114 (2009) D14305

[1] *Radiochemistry and Environmental Chemistry, Paul Scherrer Institut, Villigen*
[2] *Oeschger Centre, University of Bern*

THE LASCHAMP EVENT IN THE NGRIP ICE CORE

First manifestation of the 40 kyr ^{10}Be peak at NGRIP

M. Christl, J. Lachner, A. Müller, M. Bock[1], H. Fischer[1], F. Steinhilber[2], S. Bollhalder[2], J. Beer[2]

To look for the Laschamp geomagnetic excursion in the NGRIP ice core (Fig. 1) we measured ^{10}Be concentrations in the ice of the time period between 34 and 42 kyr BP. For the first time also, both the $\delta D(CH_4)$ signature of entrapped air [1] and the ^{10}Be concentration were successfully analyzed in the same sample. After degassing the samples for the $\delta D(CH_4)$ analysis 150 µg of ^{9}Be carrier was added. The spiked and degassed water was chemically purified and prepared for ^{10}Be/^{9}Be analysis at the compact (0.6 MV) AMS system TANDY.

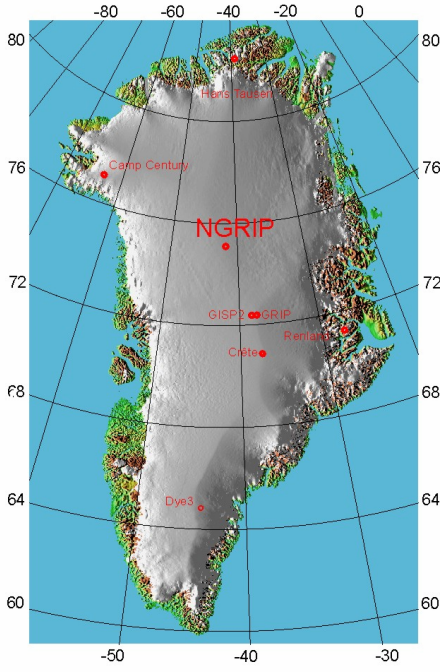

Fig. 1: *Location of the Greenland ice cores.*

The measured ^{10}Be concentrations at NGRIP are almost 2 times higher than the GRIP data [2]. This deviation is mainly caused by the lower snow accumulation rate at NGRIP. The calculated depositional fluxes of ^{10}Be (Fig. 2) are however similar at both locations. But an offset of about 30% between the ^{10}Be flux at NGRIP and GRIP remains. This offset might indicate differences in the transport or deposition processes of ^{10}Be at both localities. Whether a relative change between dry and wet precipitation of ^{10}Be could quantitatively explain the increased ^{10}Be flux at NGRIP is currently being investigated. Also a potential contribution of ^{10}Be desorbed from dust particles will be looked at.

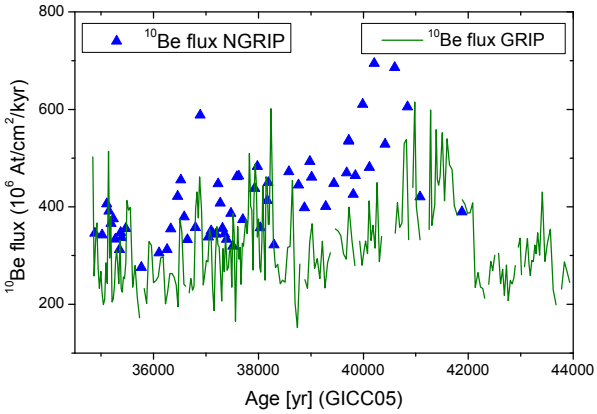

Fig. 2: *^{10}Be flux at NGRIP (blue) compared to the GRIP data (green) in the time range of 35 to 42 kyr BP.*

The increased ^{10}Be deposition recorded between about 40 - 41 kyr represents the first manifestation of the Laschamp geomagnetic event in the NGRIP ice core. A comparison with the ^{10}Be flux at GRIP, however, reveals that not the complete Laschamp peak has been sampled and analyzed (green line, Fig. 2).

[1] M. Bock et al., Science 328 (2010) 1668
[2] F. Yiou et al., J. Geophys. Res. 102 (1997) 26783

[1] *Climate and Environm. Physics, University of Bern*
[2] *EAWAG, Dübendorf*

^{7}Be AND ^{10}Be IN PRECIPITATION IN SWITZERLAND

Variations in the depositional fluxes of cosmogenic beryllium

M. Mann[1,2], J. Beer[1], F. Steinhilber[1], J.A. Abreu[1], M. Christl, P.W. Kubik

The aim of this project was to find common variances in precipitation records of cosmogenic ^{7}Be and ^{10}Be and terrestrial chemical components such as SO_4, NO_3, NH_4 and Ca to identify the deposition mechanism of cosmogenic beryllium. For this we analyzed cosmogenic ^{7}Be and ^{10}Be concentrations in precipitation at Jungfraujoch (3580m a.s.l.) collected on a monthly basis since 1982 and in Dübendorf (440m a.s.l.) sampled from 1988 on.

Using principle component analysis we identified 4 different site specific deposition mechanisms. The washout component is the first principle component at both sites. The depositional pattern for the aerosol constituents SO_4, NO_3 and NH_4 looked similar to those of ^{7}Be and ^{10}Be as exemplified with ^{10}Be and SO_4 in Fig. 1.

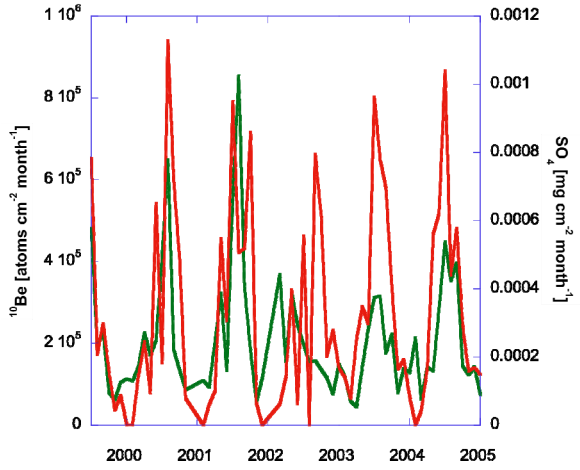

Fig. 1: *Monthly fluxes of ^{10}Be (green) and SO_4 (red) at Jungfraujoch.*

The calcium deposition flux is identified as the second principle component. Monthly fluxes of ^{7}Be and Ca between 1999 and 2004 at Dübendorf are shown in Fig. 2. There is a high common variance with the ^{7}Be flux but a lower one with ^{10}Be depositional flux. At Jungfraujoch, the calcium component could not be identified. Instead we found a component, which contains only the aerosol constituents SO_4, NO_3 and NH_4, showing a high common variance with the flux of both ^{7}Be and ^{10}Be.

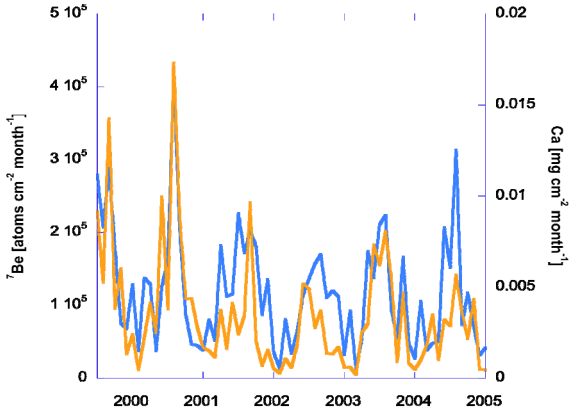

Fig. 2: *Monthly fluxes of ^{7}Be (blue) and Ca (orange) at Dübendorf.*

At Jungfraujoch, a large part of the variance of both beryllium isotopes could not be explained by the variance of any input parameter and was assigned to a fourth principle component.

Summarizing, 90% of the ^{7}Be variance and 80% of the ^{10}Be variance in the deposition can be explained by the variance of SO_4, NO_3, NH_4 and Ca at Dübendorf. At Jungfraujoch, the corresponding numbers are 40% for ^{7}Be and 65% for ^{10}Be.

[1] M. Mann et al., Atmospheric Environment, submitted

[1] *EAWAG, Dübendorf*
[2] *Biogeochemistry and Pollutant Dynamics, ETHZ*

CHLORINE-36 IN RAIN AND CAVE DRIPPING WATERS

An investigation of the evapo-transpiration at Bunker Cave, Germany

C. Münsterer[1], M. Christl, V. Alfimov, S. Ivy-Ochs, A. Mangini[1]

Speleothems are regarded as valuable paleo-climate archives, because they grow in many parts of the world and can be precisely dated by U-series [1]. In order to understand the information stored in speleothems, it is essential to develop a profound knowledge of the processes that influence the composition of substances and isotope concentrations in the seepage water and thus in the stalagmites. One important process is evapo-transpiration, because the amount of infiltration is the difference between precipitation and evapo-transpiration. Calculating the evapo-transpiration from climate data is an unsatisfactorily solved problem [2].

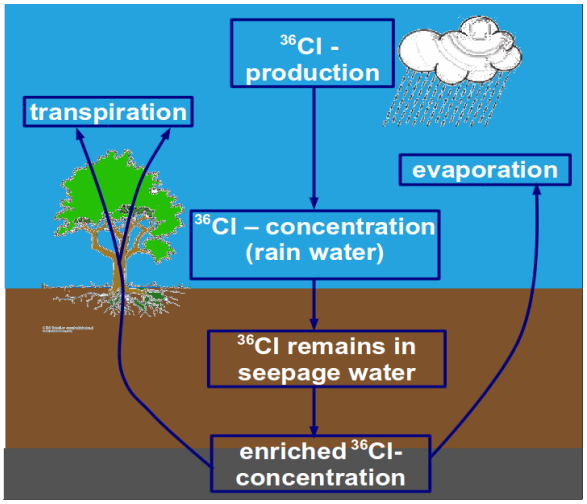

Fig. 1: *^{36}Cl pathways in dripping and rain water.*

Here we present a new approach. Ten monthly rain and dripping water samples from three drip sites in the Bunker Cave near Iserlohn, Germany were collected to measure their ^{36}Cl/Cl ratios and stable chlorine concentrations. ^{36}Cl is generally considered to be a conservative substance and its only significant source is expected to be atmospheric production (Fig. 1). The evaporative enrichment factors calculated from the ^{36}Cl and the stable Cl concentrations in rain and dripping water are too high to be the result of evapo-transpiration (Fig. 2).

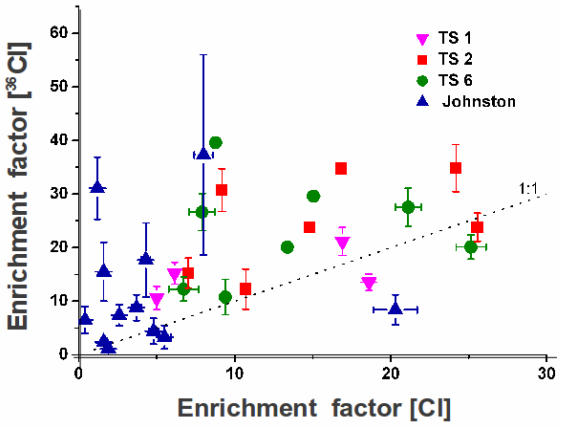

Fig. 2: *Enrichment factors for stable Cl and ^{36}Cl from this work and data from Johnston [3].*

The most likely source for the additional ^{36}Cl in dripping water is the nuclear weapon test series during the 1950s and 60s. If retained in the soil due to uptake by minerals and organic material, it would have been subsequently released. Thus, ^{36}Cl seems not to behave as a conservative tracer in areas where the soil is covered by vegetation. The high stable Cl values in dripping water are most likely the result of anthropogenic contamination. The residence time of ^{36}Cl in the soil for drip site TS 2 was estimated to be (645 +/-348) years.

[1] D. Scholz et al., J. Quat. Sci. 57/12 (2008) 52
[2] H. Häckel, Ulmer UTB (2008), 6th edition
[3] V. E. Johnston, Ph.D. thesis (2009) University College, Dublin, Ireland

[1] *Heidelberg Acadamy of Sciences, Heidelberg, Germany*

SEDIMENTATION RATES IN THE ARCTIC OCEAN

Carrier-free determination of $^{10}Be/^{9}Be$ ratios

J. Lachner, M. Christl, M. Frank[1], M. Jakobsson[2]

A method to determine natural $^{10}Be/^{9}Be$ ratios without using ^{10}Be carrier has been developed for the compact 0.6 MV AMS system TANDY. It simplifies the determination of the $^{10}Be/^{9}Be$ ratio and is more precise, because only a single measurement is required.

The four samples analyzed in this study are from two sediment cores located in the central Arctic Ocean (HLY0503-09JPC, HLY0503-14JPC; 9 and 14 in Fig. 1). These cores had been analyzed previously for natural $^{10}Be/^{9}Be$ using a combination of ICP-MS (^{9}Be) and AMS (^{10}Be) [1].

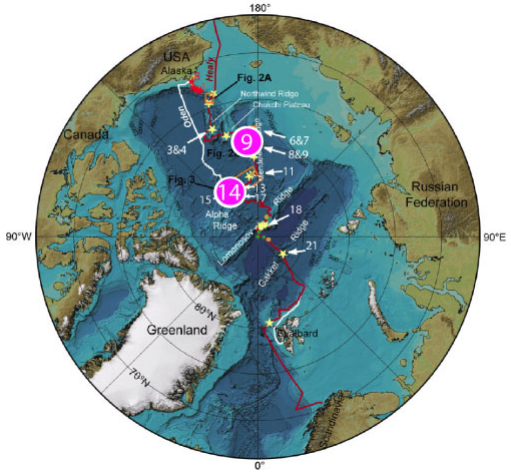

Fig. 1: *HLY0503 cruise track and studied sites.*

A comparison between the conventionally derived $^{10}Be/^{9}Be$ ratios and the carrier-free measurements (Fig. 2) shows that the new method yields systematically higher ratios. However, the resulting sedimentation rates of 2.1 mm/ka and 1.4 mm/ka are the same as obtained with the conventional method (Fig. 2). The good agreement means that the new carrier-free method is applicable to determine sedimentation rates in marine sediments.

The offset between the two methods is puzzling, as it affects all samples in the same way with a practically constant factor of 2. Since a contamination with ^{10}Be is unlikely, the offset may result from different leaching procedures applied (attacking a variable amount of lithogenic ^{9}Be). Also matrix effects during the ICP-MS measurement of ^{9}Be have to be considered as a source of systematic error. Further, the $^{10}Be/^{9}Be$ ratios measured in the surface sediments with the carrier free method correspond better to the deep water signature in the Arctic Ocean [2].

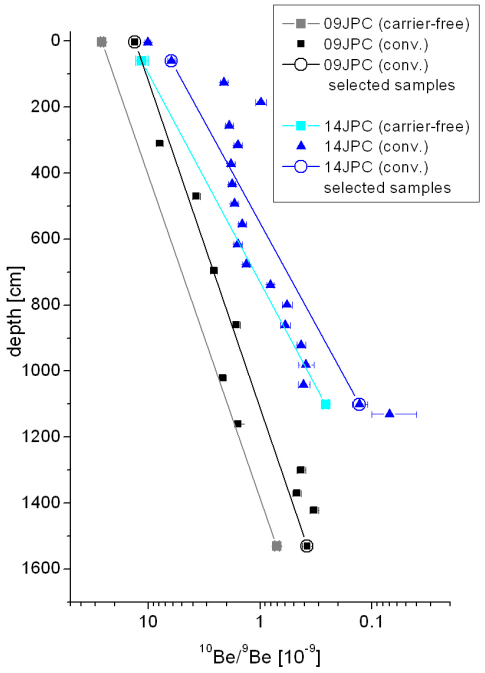

Fig. 2: *Comparison of the carrier-free $^{10}Be/^{9}Be$ ratios with values of the conventional method.*

[1] E. Sellen et al., Global Planet Change 68 (2009) 38

[2] M. Frank et al., Geochim. Cosmochim. Acta 73 (2009) 6114

[1] *IFM GEOMAR, Kiel, Germany*

[2] *Geology and Geochemistry, Stockholm University, Stockholm, Sweden*

BERYLLIUM-10 PRODUCTION FROM MARINE RECORDS

A high resolution reconstruction from Atlantic sediment cores

M. Christl, J. Lippold[1], F. Steinhilber[2], F. Bernsdorff[1], A. Mangini[1]

The global ^{10}Be production rate over the past 250 kyr was extracted from three cores taken from highly accumulating Atlantic sediments (Fig. 1) [1]. A novel three-step correction procedure was applied to eliminate climate induced transport effects. To ensure high quality of the final reconstruction two strict data selection criteria had to be fulfilled for each individual record (average sedimentation rate > 10 cm/kyr and more than 100 ^{10}Be and ^{230}Th$_{ex}$ data points).

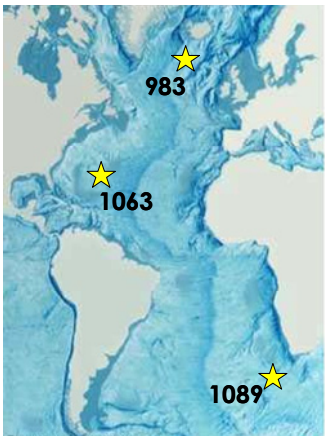

Fig. 1: *Location of the ^{10}Be records used for the reconstruction. The numbers identify the Ocean Drilling Program (ODP) sites.*

In the first correction step, Thorium-230 was employed as a constant flux tracer to calculate vertical accumulation rates of ^{10}Be at each location. In the second step, simple box model calculations were used to correct each individual record for the different scavenging behavior of Be and Th. In a third step, each single record was normalized by subtracting its mean value and by dividing with the respective standard deviation. Then, the three profiles were synchronized with the SINT800 record, which was chosen as an independent paleomagnetic reference signal. Finally, Principal Component Analysis (PCA) was applied to extract the signal (PC1) that explained most of the variance in all three records (Fig. 2). PC1 is interpreted as the normalized record of global ^{10}Be production rate over the past 250 kyr. It explains 85% of the variance in the synchronized and transport corrected ^{10}Be records.

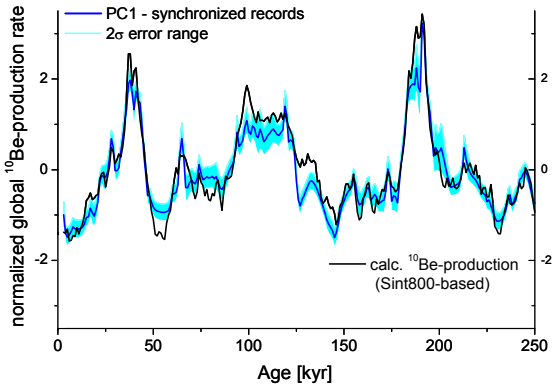

Fig. 2: *PC1 of the synchronized and transport corrected ^{10}Be records (blue, 2σ-error range: light blue) compared to the normalized SINT800-based ^{10}Be production rate (black).*

The reconstruction presented here is more precise than previous data from marine sediments because it is based on several highly resolved ^{10}Be-profiles and because PCA yielded robust results. The present record reflects past (long-term) variations of the flux of galactic cosmic rays on Earth. It can be used as an independent proxy for the strength of the geomagnetic dipole field, and it provides a tool to match marine archives with ice cores and terrestrial records (e.g. lake sediments).

[1] M. Christl et al., Quatern. Sci. Rev. 29 (2010) 2663

[1] *Heidelberg Academy of Sciences, Heidelberg, Germany*
[2] *EAWAG, Dübendorf*

PAST WATER MASS MIXING IN THE SW INDIAN OCEAN

Radiogenic isotope records of the past 20 million years in Fe-Mn crusts

L. Heuer[1], M. Frank[1], T. Stichel[1], B.A. Haley[1], M. Christl, G. Uenzelmann-Neben[2], M. Watkeys[3]

Hydrogenous ferromanganese crusts precipitate directly from ambient deep water and grow very slowly at rates of a few mm/Ma. They incorporate and record past variations of the isotope composition of dissolved trace elements, such as Be, Nd, Hf, and Pb, which have residence times in the ocean shorter than the global ocean mixing time (<1000 a). These records can be applied to reconstruct past changes in deep water circulation on million year time scales.

We examined three ferromanganese crusts from the Mozambique Ridge in the SW Indian Ocean recovered from water depths ranging from 1850 m to 3790 m. The shallowest crust MKW05-42 is currently bathed in Antarctic Intermediate Water, whereas at the deeper locations (crusts MKW05-85, MKW05-26) North Atlantic Deep Water (NADW) prevails today.

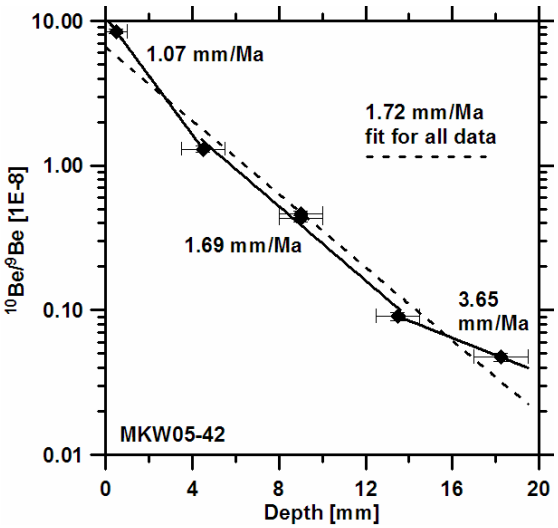

Fig. 1: *$^{10}Be/^{9}Be$ ratios of crust MKW05-42 versus profile depth.*

Ages and growth rates were derived from profiles of $^{10}Be/^{9}Be$ ratios applying the recently revised half-life of 1.387 million years. As an example, Figure 1 shows the $^{10}Be/^{9}Be$ data of MKW05-42 plotted against depth in the crust. Based on these data the crust grew with different rates between 3.65 mm/Ma in the oldest part and 1.07 mm/Ma in the top 4 mm. The uppermost $^{10}Be/^{9}Be$ value is close to $9 \cdot 10^{-8}$, which is similar to deep waters in the Indian Ocean.

Based on the dating, the εNd compositions of deep waters at MKW05-85 and MKW05-26 have been significantly more negative than those of MKW05-42 over the past 9 million years (Fig. 2). This is consistent with the admixture of NADW (which has a distinctly more negative εNd signature) at water depths between 2000 and 4000 m. Prior to 9 million years ago, the values are similar at 1850 m and 2780 m water depth, which can be either attributed to a reduced supply of NADW or more efficient vertical mixing at that time.

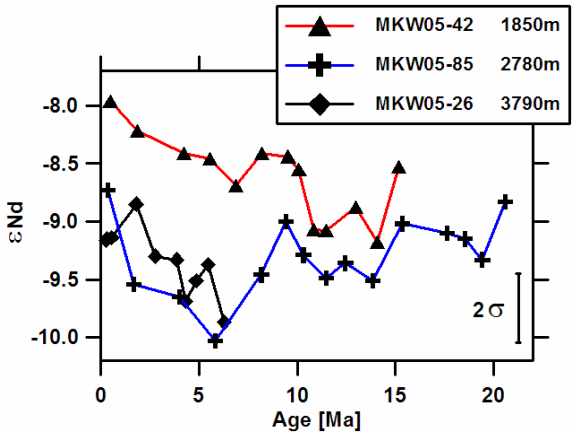

Fig. 2: *Time series of deep water Nd isotopes (given in εNd notation, which corresponds to deviations of the measured $^{143}Nd/^{144}Nd$ from that of the CHUR standard in tenths of ‰).*

[1] *IFM-GEOMAR, Kiel, Germany*
[2] *Alfred-Wegener-Institute, Bremerhaven, Germany*
[3] *Geological Sciences, KwaZulu-Natal University, Durban, South Africa*

URANIUM-236 IN THE ATLANTIC OCEAN

The vertical distribution of ^{236}U in the western Equatorial Atlantic

M. Christl, J. Lachner, O. Lechtenfeld[1], C. Vockenhuber, M. Rüttimann, I. Stimac[1], M. Rutgers v. d. Loeff[1]

During the Pelagia Geotraces cruise in July/August 2010, six 20 l water samples were collected in order to create the very first oceanic depth profile of Uranium-236 ($T_{½}$ = 23.4 Myr). At the selected locations it is expected to find the transition between the anthropogenic ^{236}U signal on top (mainly from global fallout) and the natural ^{236}U signal in the deep ocean (from eroded continental material that has been exposed to cosmic ray induced neutrons).

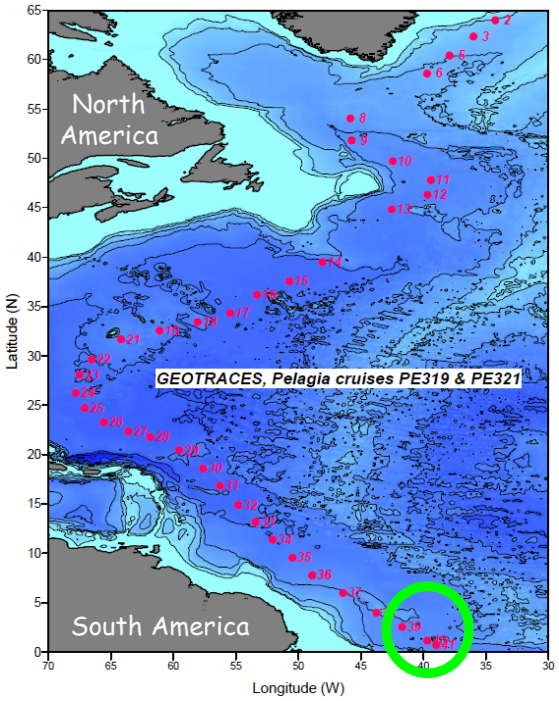

Fig. 1: *Cruise track of the Pelagia Geotraces expedition in 2010. The green circle marks the sampling locations for ^{236}U (stations 39 and 40).*

The measurements are being performed on the compact (0.6 MV) AMS system TANDY at background levels below 10^{-11} [1]. A ^{233}U spike is used to trace the yield of the chemical separation procedure. Our results (Fig. 2) show that ^{236}U/^{238}U ratios decrease from about 10^{-9} at the surface (in accordance with ^{236}U from global fallout) to about 10^{-10} at a depth of 4250 m. The deep ocean signal is about two orders of magnitude higher than expected from the sole input of natural sources.

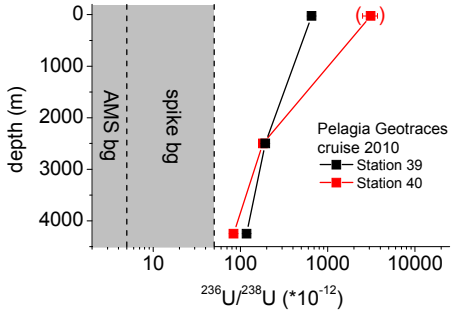

Fig. 2: *^{236}U/^{238}U depth profile in the western Equatorial Atlantic Ocean. The grey regions indicate the machine background and the unexpectedly high spike background for this particular measurement. There are indications that the bracketed data point was contaminated with ^{236}U during sample preparation.*

The level of detection during this particular AMS measurement was limited by ^{236}U present in the ^{233}U spike (Fig. 2). This however cannot explain the elevated ratios in the bottom waters. Whether the transport and the subsequent release of particle-bound U from the surface waters could be a quantitative explanation for the observed values, is currently being investigated. Box modeling results further indicate that also the advection of North Atlantic water masses from the Iceland-Shetland region containing anthropogenic ^{236}U from reprocessing might have contributed significantly to the elevated ratios observed at a depth of 2500 m.

[1] C. Vockenhuber et al., Nucl. Instr. & Meth. B, submitted

[1] *Alfred Wegner Institut, Bremerhaven, Germany*

ANTHROPOGENIC URANIUM-236 IN THE NORTH SEA

Creating the first comprehensive dataset

M. Christl, J. Lachner, I. Goroncy[1], C. Vockenhuber, M. Rüttimann, J. Herrmann[1], H.-A. Synal

Uranium-236 ($T_{½}$ = 23.4 Myr) is mainly produced by neutron capture of ^{235}U. It can be used as a tracer for U-containing materials that have been exposed to elevated neutron fluxes. Over the past ≈60 years, the North Sea has been continuously subjected to significant releases of man-made nuclear material. The main potential sources of anthropogenic ^{236}U in the North Sea are (i) releases from nuclear reprocessing, (ii) import of ^{236}U from the Chernobyl accident via the Baltic Sea, and (iii) atmospheric or riverine input of ^{236}U from atmospheric nuclear weapons tests.

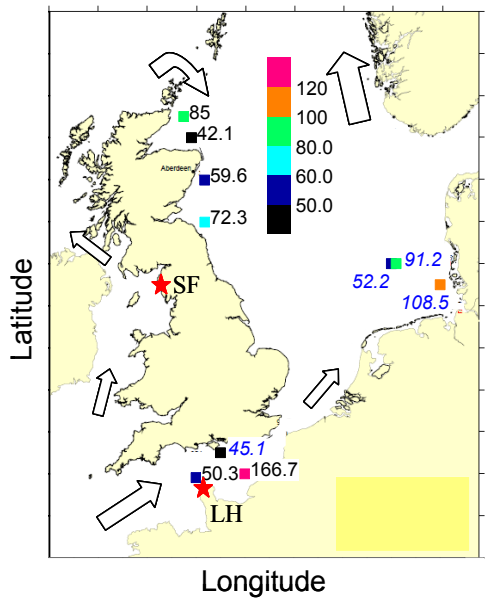

Fig. 1: *Concentration of ^{236}U (10^6 at/l) in the North Sea (sampled in 2009, italics: 2001 and 2002). The red stars show the reprocessing plants Sellafield (SF) and La Hague (LH). The arrows roughly indicate the surface water flow.*

In order to identify the sources of ^{236}U in the North Sea and to explore the potential of ^{236}U as a new oceanic tracer the first comprehensive dataset of ^{236}U in the North Sea is currently being produced. The measurements are performed on the compact (0.6 MV) AMS system TANDY [1] at background levels below 10^{-11} (see also "Detection limits of ^{236}U at TANDY" and "3+ molecules of actinides and hydrogen" in this report).

About 35 water mass samples collected in 2009 (Pelagia 311 cruise) and four samples from earlier cruises (2001 and 2002) are available for ^{236}U-analysis. Our first results (Fig. 1) show ^{236}U concentrations between about 40 x 10^6 and about 170 x 10^6 at/l (corresponding to ^{236}U/^{238}U ratios of 0.6 x 10^{-8} and 2.2 x 10^{-8}).

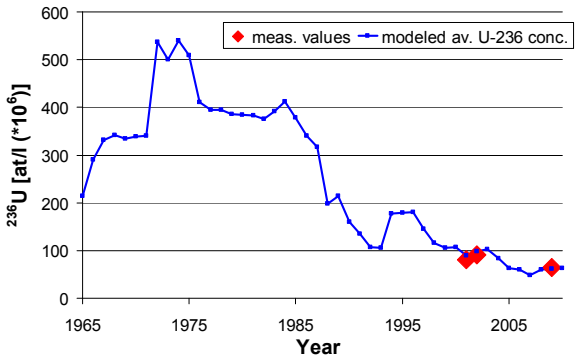

Fig. 2: *Measured ^{236}U concentrations (red) compared to box model results (blue).*

Box model results based on U-release data from Sellafield and La Hague indicate that no other source of ^{236}U than nuclear reprocessing is needed to explain the observed concentrations (Fig. 2). This preliminary result, in turn, suggests that ^{236}U input from Chernobyl or from global fallout was negligible at least between 2001 and 2009.

[1] C. Vockenhuber et al., Nucl. Instr. & Meth. B, submitted

[1] *Bundesamt f. Seeschifffahrt u. Hydrogr., Hamburg, Germany*

LONG-LIVED RADIONUCLIDES AT BIKINI ATOLL

^{41}Ca, ^{14}C and ^{10}Be concentrations in coral sand at a nuclear test site

J. Lachner, V. Alfimov, M. Christl, I. Hajdas, P.W. Kubik, M. Rüttimann, T. Schulze-König, L. Wacker

^{41}Ca, ^{14}C and ^{10}Be concentration were determined in several coral sand samples ($CaCO_3$) from the Bikini atoll (Fig. 1) using our low-energy AMS facilities TANDY and MICADAS. The measured values were compared to expected concentrations based on the relevant neutron capture cross-sections for their production from $CaCO_3$.

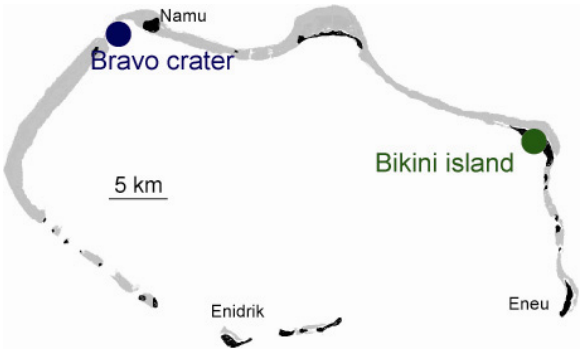

Fig. 1: *Sites sampled for the project*

In a sample from the crater of the nuclear explosion Castle Bravo (1954) all radionuclides showed increased concentrations (Fig. 2). Coral $CaCO_3$ might therefore be applied as a biogenic neutron flux dosimeter.

The high neutron flux of the large nuclear explosion could have produced those nuclides mainly via the nuclear reactions $^{40}Ca(n,\gamma)^{41}Ca$, $^{17}O(n,\alpha)^{14}C$ and $^{13}C(n,\alpha)^{10}Be$. The measured ^{41}Ca concentration was used to normalize the neutron flux because of the well-known production cross-section and the unique abundance of the target nuclide ^{40}Ca in coral sand.

The measured values for ^{14}C and ^{10}Be are much higher than expected from the calculations. This indicates a more complex scenario than simple $CaCO_3$ irradiation. Production processes in addition to the ones considered above might have played a role, e.g. $^{14}N(n,p)^{14}C$ or fallout of ^{10}Be from ternary fission, where in the fission of uranium one light particle is produced along with two heavier fragments.

Nitrogen as an additional target in coral $CaCO_3$ could explain the high ^{14}C production, as the reaction has a large cross section and nitrogen is abundant in the coral skeletons and moreover in living organic tissue. Irradiation of this tissue and subsequent bioproductivity in the crater could possibly explain the abnormally large $^{14}C/^{12}C$ ratios found in the crater sample.

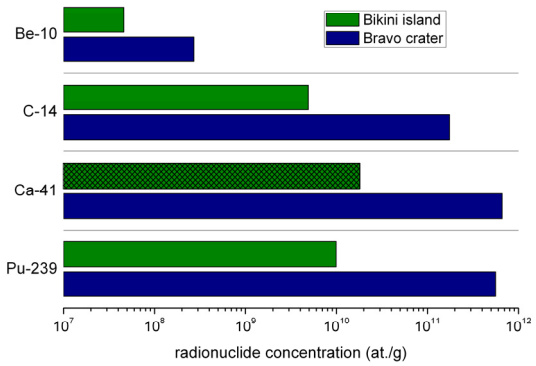

Fig. 2: *Measured radionuclide concentrations on Bikini Island and in Bravo Crater. The ^{41}Ca concentration from Bikini Island (hatched green) is at the level of the corresponding AMS blank sample. Measured Pu-239 concentrations at the Bikini test site are shown for completion [1].*

Although the concentration of ^{10}Be (2.7×10^8 at./g) found in the Bravo sample is higher than could be expected from the irradiation of the $CaCO_3$ target alone, it is low compared to concentrations of atmospheric (cosmogenic) ^{10}Be measured in natural archives like marine sediments. ^{10}Be was thus produced in a minor way during the bomb tests and a ^{10}Be bomb peak like those for ^{14}C and ^{36}Cl is not expected to be found in any natural archive.

[1] J. Lachner et al., Ion Beam Physics Annual report (2009) 82

BIOMEDICAL APPLICATIONS

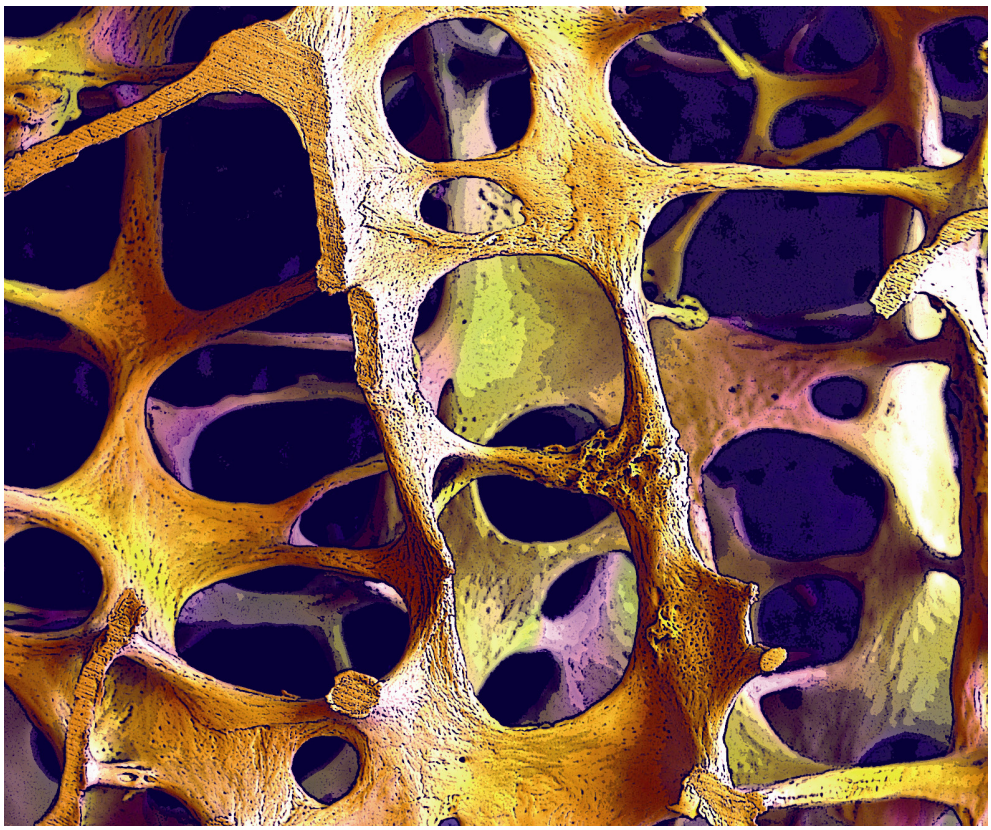

Semi-automated, high-throughput Bio-AMS

The impact of vitamin D on bone health

Isotopic labeling of a sheep skeleton

SEMI-AUTOMATED, HIGH-THROUGHPUT BIO-AMS

A concept for automated radiocarbon analysis of LC fractions

T. Schulze-König, L. Wacker, H.-A. Synal

Radiocarbon analysis does not provide information on the chemical structure or other properties of a sample. Biomedical samples are therefore often pre-analyzed with liquid chromatography (LC). There is general interest in linking such front-end analyzers with AMS.

A direct coupling is facilitated with CO_2 accepting ion sources, since CO_2 reduction to graphite and sample loading become superfluous. An effort has been made at ETH to couple a C-H-N analyzer system with a sputter ion source [1]. Here, samples are sequentially combusted and the C fraction, available as CO_2, is stored on a zeolite molecular sieve. At temperatures of 750 K, all the CO_2 is rapidly released and then flushed into a syringe using He as a carrier gas. The gas mixture is then injected into the AMS ion source at a well-defined flow rate. The C-H-N and subsequent AMS analyses are fully automated. This system will serve as a basis for a semi-automated analysis of LC fractions.

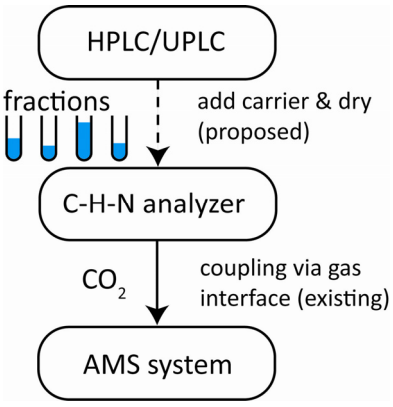

Fig. 1: *Schematic of the (proposed) workflow.*

In the workflow depicted in Fig. 1, the LC system and C-H-N analyzer are not linked directly. The LC fractions to which 10 to 20 µg carrier material have already been added are collected in capsules appropriate for the C-H-N analyzer. Chromatographic fractions must be dried prior to C-H-N analyses, which is also necessary for traditional combustion. This generates only a little extra bit of work. Samples can then be introduced into the C-H-N analyzer for automatic analysis.

Compared to the regular sample combustion method, the procedure has three major advantages: *First*, manual labor in the sample analysis process is drastically reduced. *Second*, the C-H-N analyzer measures also the total C content of the sample and thus eliminates a significant source of uncertainty caused by unlabeled carbon which comes either from the natural occurring carbon content of the fraction or from non-volatile LC eluates. *Third*, the amount of carrier material required is reduced by a factor of ~50. Consequently, the ^{14}C tracer signal increases and improves the lower limit of quantization (LLOQ), which is roughly 10^5 atoms ^{14}C (Tab. 1). The sample throughput for this setup is limited by the C-H-N analyzer to 7 min per sample. This time can be easily reduced with additional C-H-N analyzers.

Method	**Carrier**	**LLOQ**
Sample combustion, graphitization	0.5-1 mg	~10^6 atoms
C-H-N analyzer and CO_2 ion source	10-20 µg	~10^5 atoms

Tab. 1: *Comparison of the status quo and the proposed method.*

The implementation of the proposed procedure is planned in close collaboration with a pharmaceutical company. If successful, the new method will allow an almost completely automated analysis of chromatographic fractions with AMS.

[1] M. Ruff et al., Radiocarbon 52 (2010) 1645

THE IMPACT OF VITAMIN D ON BONE HEALTH

Using ^{41}Ca to study effects on postmenopausal bone health

K. Hotz[1], T. Schulze-König, M. Zimmermann[1]

Osteoporosis, a disease caused by accelerated bone loss in the elderly, is a major global public health concern. The availability of sensitive techniques to monitor the rate of bone loss prior to the onset of osteoporosis and associated fractures is therefore a crucial prerequisite for prevention-oriented research.

A promising methodology to monitor small changes in bone calcium fluxes in response to nutritional interventions is the ^{41}Ca technique. ^{41}Ca with a half-life of 10^5 years is virtually stable. The natural ^{41}Ca content of bone is extremely low, which permits labeling bone with very low doses of ^{41}Ca. Although ^{41}Ca is classified as radioactive, labeling bone with this isotope can be done at negligible health risk, since analysis by AMS requires administration of only minute amounts of ^{41}Ca.

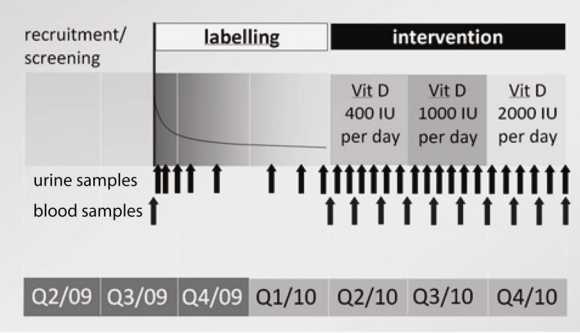

Fig. 1: *Design of the vitamin D intervention trial using the ^{41}Ca technique.*

In our current vitamin D trial (Fig. 1), ^{41}Ca methodology is used to investigate: 1) whether vitamin D doses higher than the current recommendations are favorable in terms of bone health; and 2) what is the serum 25(OU)-vitamin D associated with positive Ca bone flux. Apparently healthy (non-osteoporotic) women (n=25) were administered a single intravenous dose of 1.2 kBq ^{41}Ca. Subsequently, urinary ^{41}Ca/^{40}Ca isotope ratios were monitored via 24 h urine collections to establish the kinetics of urinary clearance of the isotopic label. At 6 months post-dosing, when excreted tracer mainly originated from bone, a 36 week intervention period was initiated. All subjects were sequentially supplemented with increasing amounts of vitamin D per day: 10 µg (current recommendation), 25 µg, and 50 µg (each for 12 weeks, see Fig. 1). In parallel to urine sampling and analysis of ^{41}Ca/^{40}Ca by AMS, serum 25(OH)-vitamin D concentrations were monitored by blood sampling and analysis by radioimmunoassay (RIA) at the University Hospital Zurich every 4 weeks.

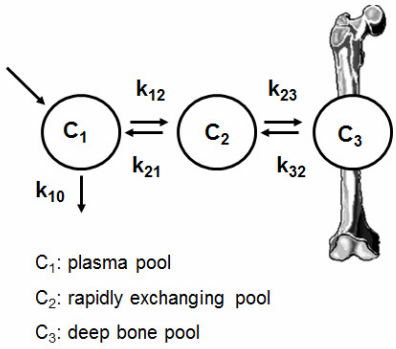

Fig. 2: *Linear three-compartment model used to evaluate urinary ^{41}Ca tracer excretion in human studies at ETH.*

Sample collection was completed at the end of 2010, while sample processing and analysis is on-going. The impact of vitamin D on the Ca transfer rates will be calculated from the three-compartment model shown in Fig. 2. Within-subject comparisons of individual parameters will be done during the intervention periods. The study outcome will help to identify serum 25(OH)-vitamin D levels optimal for bone health.

[1] *Institute of Food, Nutrition and Health, ETHZ*

ISOTOPIC LABELING OF A SHEEP SKELETON

Tracing bone calcium metabolism in a sheep with ^{41}Ca and ^{86}Sr

T. Schulze-König, M. Rüttimann, F. Dewi[1], A. Liesegang[2], G. Kuhn[3], C. Weigt[3], T. Walczyk[1], H.-A. Synal

Sensitive techniques for assessing changes in bone metabolism are needed for the evaluation of novel strategies for osteoporosis prevention and treatment. Existing limitations can be potentially overcome by the use of ^{41}Ca or ^{86}Sr as bone calcium tracers. Following administration, both isotopic tracers are partially incorporated into the bone matrix. After a labeling period of a few months, when most of the tracer has been cleared from compartments other than bone, excreted tracer material in urine originates mainly from bone and is supposed to reflect the bone Ca metabolism.

As reported last year, we designed a study to examine the incorporation of ^{41}Ca and ^{86}Sr into bone. For this reason, a 2-year-old female domestic sheep was labeled with a single dose of ^{41}Ca (2.85 kBq) and ^{86}Sr (40 mg). The tracer concentrations were then analyzed in urine over a time span of six months (Fig. 1). ^{86}Sr concentrations in urine must be normalized to Ca, because strontium levels in blood vary. Excreted tracer levels indicate a similar behavior with different time constants (Fig. 2).

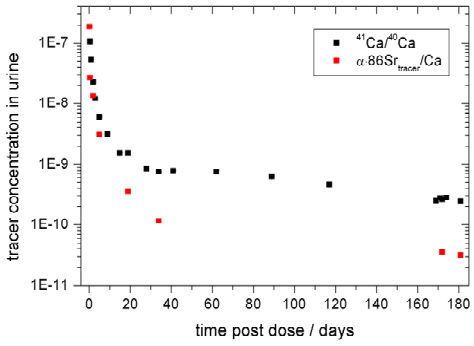

Fig 1: *Measured tracer concentrations in urine.*

Finally, the sheep was sacrificed and bone samples were taken. Overall, 19 bone samples have been prepared and analyzed so far (Fig. 3).

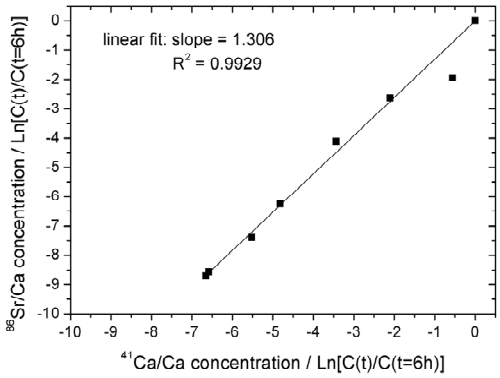

Fig 2: *Comparison of ^{41}Ca and ^{86}Sr excretion in urine.*

^{41}Ca/^{40}Ca and ^{86}Sr$_{tracer}$/Sr concentrations at different bone sites varied in the range of 10^{-10} to 10^{-9}, and $3{\cdot}10^{-3}$ to $3{\cdot}10^{-2}$, respectively. Except for three outliers, there is a good correlation between Sr and Ca tracer signals in bone (r>0.9).

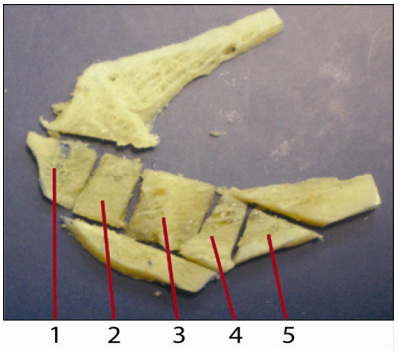

Fig 3: *Bone sampling sites at radius (distal).*

A detailed analysis of the data is in preparation. It is expected to highlight differences in the dynamics of these interesting bone metabolism tracers.

[1] *Chemistry and Biochemistry, NUS, Singapore*
[2] *Institute of Animal Nutrition, University of Zurich*
[3] *Institute for Biomechanics, ETHZ*

MATERIALS SCIENCES

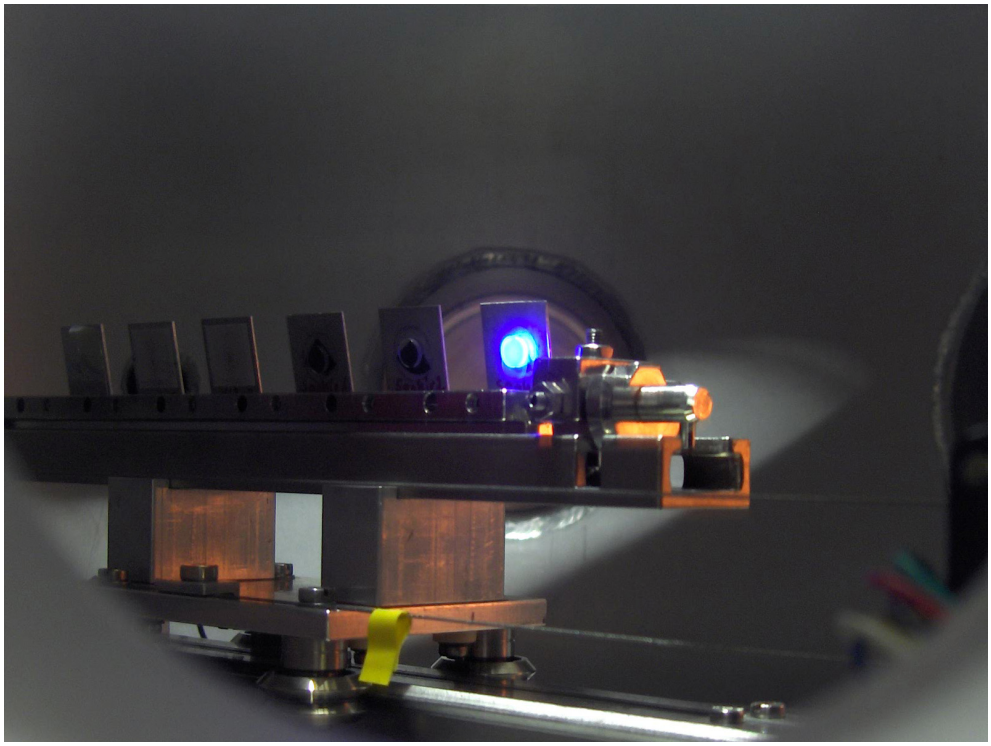

Ion transmission through glass capillaries

First STIM images with a capillary microprobe

Production of silicon nitride membranes

Surface damage during Ion Beam Analysis

Depth profiles in organic photovoltaic materials

Composition determination of thin nitride films

Evolution of nanoporosity in de-alloyed films

Tracing ruthenium in spent catalysts

ION TRANSMISSION THROUGH GLASS CAPILLARIES

Phase space measurements at the IRRSUD beam line (GANIL facility)

M.J. Simon, A. Cassimi[1], H. Shiromaru[2], C.L. Zhou[1], A. Müller, M. Döbeli

At the Laboratory of Ion Beam Physics, glass capillaries are being used to extract MeV ion beams for applications like Scanning Transmission Ion Microscopy (STIM) (see further articles in this annual report). It has been shown (e.g. [1]) that tapered glass capillaries have focusing properties, that is, the beam density after the capillary is enhanced. Either a charge build-up on the inner walls of the capillary, surface channelling, and/or small-angle Rutherford scattering are thought to be responsible for the focusing effect.

In June 2010, phase space measurements of transmitted heavy ions were made at the IRRSUD beam line of the GANIL facility (Caen, France) in collaboration with CEA (Commissariat à l' Énergie Atomique) to investigate the mechanism which leads to a beam density enhancement. A highly collimated beam of 70.95 MeV Xe^{+19} was transmitted through capillaries of 50, 22 and 7 microns outlet diameter and observed with a position sensitive detector. The capillaries were mounted on a 4-axis goniometer to align or to tilt them with respect to the incident beam. The diameter of the detector was 47 mm and located 65 cm away from the capillary, so only particles which leave the capillary with scatter angles below 2° were detected.

As can be seen in Fig. 1, the transmitted beam is divided into two parts, a core and a halo, which for the 50 microns capillary have a beam divergence of 1.3 and 7.8 mrad, respectively. The beam time structure provided by the cyclotron frequency allowed energy measurement of the particles hitting the detector through time-of-flight measurements. These measurements showed that the particles in the core have the full energy and pass the capillary without significant interaction. The halo particles suffer energy loss from scattering on the inner wall of the capillary. It is possible that these halo particles contribute to the focusing factor, which was also found in own transmission measurements. But at the moment it is not clear, whether the observed small-angle Rutherford scattering is the only process taking place.

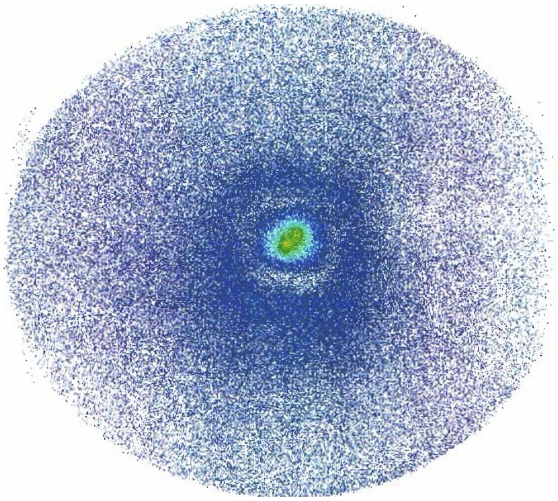

Fig. 1: *Image of the position sensitive detector for the 50 microns capillary which was well aligned to the beam. The particle counting rate in the detector increases from blue to green in the image shown.*

Unfortunately, no absolute input current and transmission normalization was possible at IRRSUD. Transmission and phase space measurements will be continued at our own facility.

[1] T. Nebiki et al., Journal of Vacuum Science & Technology A 21 (2003) 1671

[1] *CIMAP CEA/CNRS/ENSICAEN, France*
[2] *Chemistry, Tokyo Metropolitan University, Japan*

FIRST STIM IMAGES WITH A CAPILLARY MICROPROBE

Two-dimensional density maps on a microscopic scale

M.J. Simon, S. Roost, A.M. Müller, M. Döbeli

In STIM (Scanning Transmission Ion Microscopy) a focused ion beam is raster scanned across a thin sample and the residual energy of the transmitted particles is measured as a function of position. Since the energy loss of the ions is approximately proportional to the area density of the sample at each point, a density map of the specimen can be obtained (Fig. 1).

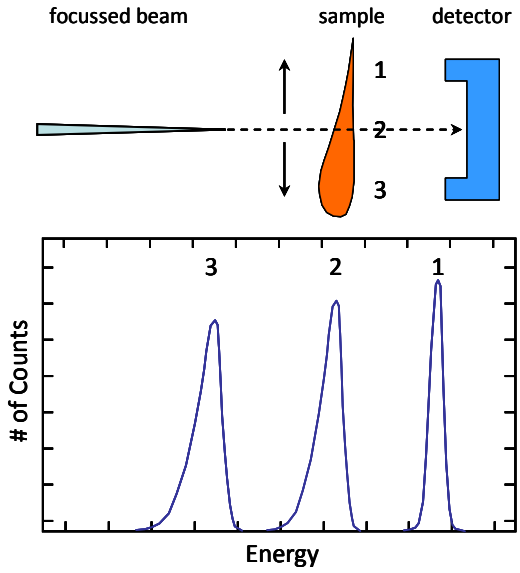

Fig. 1: *Principle of STIM: measured energy spectrum is shifted depending on sample thickness (positions 1 to 3).*

This technique has been implemented at the capillary ion microprobe of the LIP. Because the capillary cannot be moved laterally, the sample is raster scanned by a piezo XY-stage. The residual energy of transmitted particles is measured by a radiation hard, miniaturized gas ionization counter. To simplify its use the microprobe is operated in air. For STIM measurements the beam intensity is adjusted to several hundred particles per second. Fig. 2 shows a STIM image of a gold mesh acquired with a 1 MeV proton beam. The lateral resolution is slightly bigger than the tip opening of the capillary (8 μm diameter).

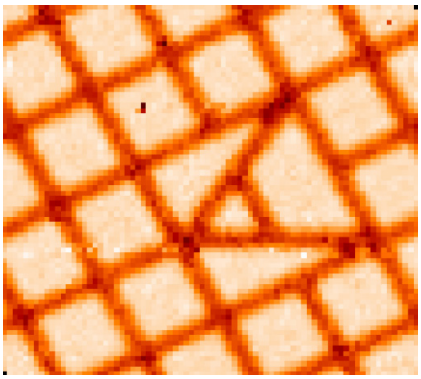

Fig. 2: *STIM image of a gold grid (mesh size 85 μm) taken with a 1 MeV proton beam.*

The STIM image of a mosquito wing section is presented in Fig. 3. The gray scale in the two-dimensional map is based on the centroid of the energy spectrum at each pixel (zero energy loss: white, maximum energy loss: black). The acquisition time for this scan was approximately 170 minutes. It is planned to speed up the raster process considerably.

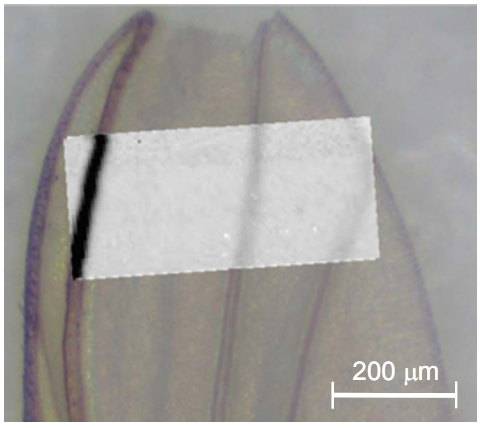

Fig. 3: *Density map of a mosquito wing overlaid on a photograph. The STIM scan was taken with a 1 MeV proton beam.*

PRODUCTION OF SILICON NITRIDE MEMBRANES

SiN_x membrane windows for gas detectors from FIRST Laboratory

M. Leibinger[1], A. Lücke[2], M. Bednarzik[2], O.J. Homan[1], A.M. Müller, M. Döbeli

Large silicon nitride entrance windows are key components for the construction of high resolution gas ionization detectors [1]. This type of membrane can be produced on native silicon frames by a MEMS (micro electro-mechanical system) process [2]. The carefully controlled deposition of stress-free silicon nitride on prime-grade silicon wafers is an absolute prerequisite for this process.

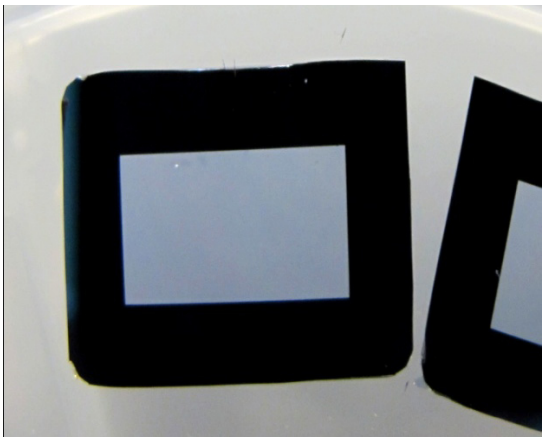

Fig. 1: *Photograph of a 8x12 mm^2 silicon nitride window with a thickness of 80 nm.*

In 2010, we have started our own production of large area membranes at ETH FIRST Center for Micro- and Nanoscience. 4" silicon nitride coated wafers with a pattern of 179 individual windows ranging from 3x3 up to 8x12 mm^2 in size can be processed (Fig. 1). After a run-in phase, the yield for intact membranes reached about 90%.

The stress-free silicon nitride films were deposited by LPCVD (Low Pressure Chemical Vapor Deposition) at the Laboratory for Micro- and Nanotechnology of the Paul Scherrer Institut. The composition and thickness of the material was determined with RBS. Fig. 2 shows the RBS spectrum of one of the films. The silicon nitride produced, which in theory should be Si_3N_4, is understoichiometric with a composition of $Si_3N_{3.4}H_{0.08}$ which is typical for very low-stress material. The hydrogen content was determined by elastic recoil detection with a 2 MeV He beam using the absorber foil technique.

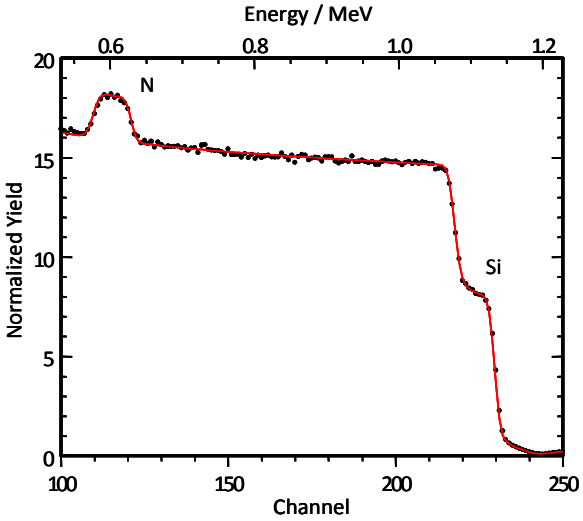

Fig. 2: *RBS spectrum of a 80 nm LPCVD silicon nitride film on silicon.*

The process can now be used to produce windows of custom designed shape and structure to further improve the performance of our in-house developed high resolution gas detectors.

[1] M. Döbeli et al., Nucl. Instr. and Meth. B219/220 (2004) 415

[2] D.R. Ciarlo, Biomedical Microdevices 4 (2002) 63

[1] *FIRST Laboratory, ETHZ*

[2] *Laboratory for Micro- and Nanotechnology, Paul Scherrer Institu, Villigen*

SURFACE DAMAGE DURING ION BEAM ANALYSIS

Heavy ion beams erode sample surface during HI-ERD and HIBS analysis

M. Döbeli, M. Mallepell, A.M. Müller

Standard 2 MeV ^{4}He Rutherford backscattering spectrometry (RBS) is often considered to be a virtually non-destructive analysis technique for many materials. If heavier MeV particles are used for ion beam analysis, like in heavy ion RBS (HIBS) or heavy ion elastic recoil detection analysis (HI-ERD), damage to the sample surface becomes much more important even for radiation hard materials.

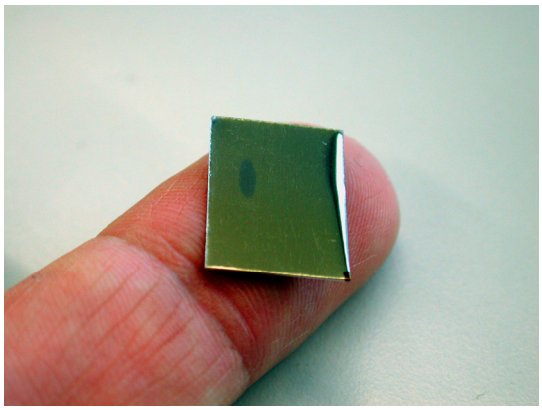

Fig. 1: *Visible beam damage on a diamond like carbon (DLC) coated aluminum sample analyzed with HI-ERDA.*

In order to judge the applicability of these heavy ion beam techniques, material removal during analysis has been examined. For this purpose, the thickness of thin metal films (Nb, Sb, Au) deposited on graphite was measured in-situ as a function of projectile beam fluence in both HIBS and HI-ERDA measurements using 15 MeV Si and 10 MeV Ti ions [1, 2].

For the majority of the studied cases, it was found that material removal from the surface takes place in two phases. At low fluences of up to 10^{15} ions/cm^2, the first 1 or 2 monolayers are eroded at a very fast rate of the order of 1 atom per impinging beam particle. In a second phase, erosion rates are reduced by one to two orders of magnitude depending on film composition and beam parameters (Fig. 2). Steady state erosion rates observed at high fluences (approx. 10^{16} ions/cm^2) are in fairly good agreement with surface sputtering rates calculated by SRIM.

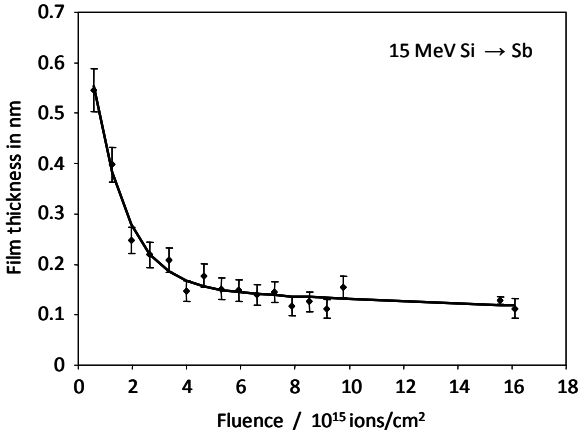

Fig. 2: *Remaining layer thickness versus beam fluence for a thin antimony film on a carbon substrate analyzed with HIBS.*

This implies that the slow film erosion is induced by collisional sputtering and is therefore relatively predictable. The origin of the fast removal phase, however, is still unclear. It might be due to desorption of the topmost atomic layer. It is also possible that the behavior is a consequence of the large roughness of the very thin metal films that probably show a large degree of islanding. Islands of different sizes might be removed at different rates.

As a consequence of these results, due care has to be exercised when analyzing films of only a few nm thickness by heavy ion beam techniques.

[1] M. Mallepell, ETH thesis 18394 (2009)
[2] M. Döbeli, M. Mallepell, A.M. Müller, Nucl. Instr. and Meth. B (2011) in press

DEPTH PROFILES IN ORGANIC PHOTOVOLTAIC MATERIALS

RBS/ERDA helps to trace counter-ion diffusion into fullerenes

J. Heier[1], R. Hany[1], F. Nüesch[1], M. Döbeli

Static p-n junctions in inorganic semiconducting materials are the basis of today's semiconductor technology. Current research on semiconducting organic materials uncovers opportunities beyond current state-of-the-art devices [1]. For instance, those materials can contain mobile counter ions that rearrange during operation enabling new device functionalities. Prominent examples are the light-emitting electrochemical cell [2] and improved charge injection by accumulation of ions near electrical contacts [3].

We have demonstrated that at organic hetero-interfaces between cationic dyes and fullerenes, ionic displacement can shift the electronic orbital energy level, which allows the direction of electron transfer processes to be controlled [4]. Little is known though about the diffusion process and ion distribution in these films. RBS and ERDA are techniques well-suited to analyze these processes.

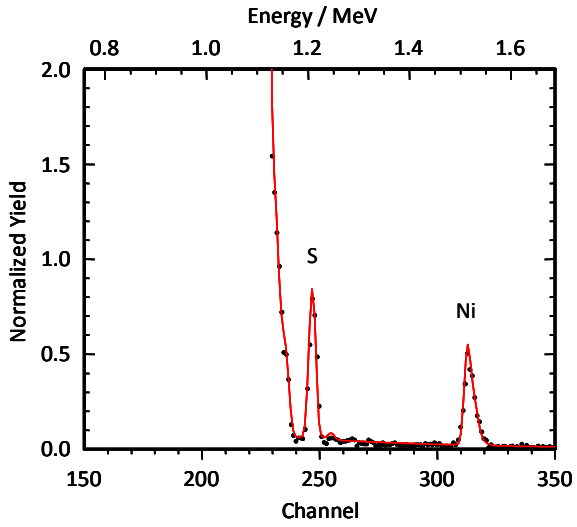

Fig. 1: *The total number of counter ions characterized here by Ni or S can be precisely determined with RBS.*

For example, thin films with blends of cationic dyes and PCBM (phenyl-C_{61}-butyric acid methyl ester) and bilayers of cationic dyes and C_{60} have been analyzed with 2 MeV He RBS (Fig. 1) and Heavy ion (^{127}I) ERDA (Fig. 2).

The results will help us to understand electronic interface properties due to ion diffusion.

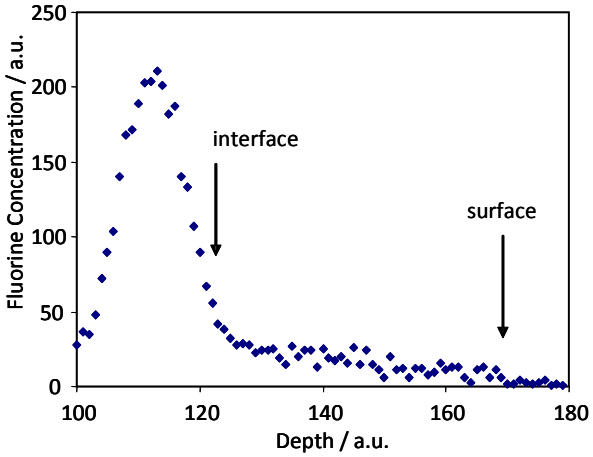

Fig. 2: *Fluorine diffusion profile in C_{60} acceptor layer measured with 13 MeV ^{127}I ERDA. Fluorine represents here the counter ion PF_6*

[1] J.M. Leger, Adv. Materials 20 (2008) 837
[2] Q. Pei et al., Science 269 (1995) 1086
[3] J.C. deMello et al., Phys. Rev. B 57 (1998) 12951
[4] H. Benmansour et al., Chimia 61 (2007) 787

[1] *Laboratory for Functional Polymers, EMPA Dübendorf*

COMPOSITION DETERMINATION OF THIN NITRIDE FILMS

Characterization of thin layers of TiN/Si_3N_4 films with RBS and ERDA

D. Jaeger[1], J. Patscheider[1], M. Döbeli

Many industrial products undergo a coating process as a last finish. An example is the hardness-enhanced protective coating that increases the durability of tools. The archetype of superhard coatings is a composite of nanocrystalline titanium nitride (TiN) and a silicon nitride (Si_3N_4) binder phase [1, 2]. In the Laboratory of Nanoscale Materials Science at EMPA in Dübendorf fundamental studies are performed on the chemistry of two-dimensional model interfaces of single-crystalline (sc) TiN films covered with Si_3N_4.

A number of materials analysis techniques are used to gain insight into the chemical bonding at the interface of such superhard coatings.

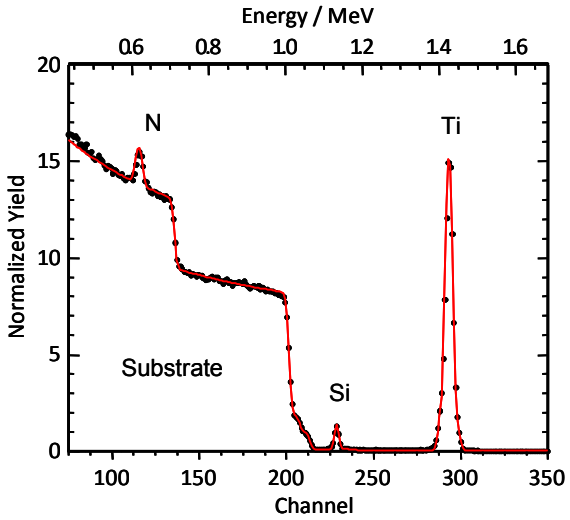

Fig. 1: *RBS spectrum (*2 MeV He) *of 20 nm silicon nitride on titanium nitride.*

The sc-TiN films are prepared by unbalanced magnetron sputtering at 800°C. As it is known that nitrogen deficient or oxidized films exhibit a reduced hardness [3], it is essential to determine the stoichiometry and thickness of such films, for which RBS and ERDA are the ideal analyzing techniques (Figs. 1 and 2). The oxygen to nitrogen ratio was measured by Heavy Ion ERDA using 13 MeV ^{127}I projectiles (Fig. 2).

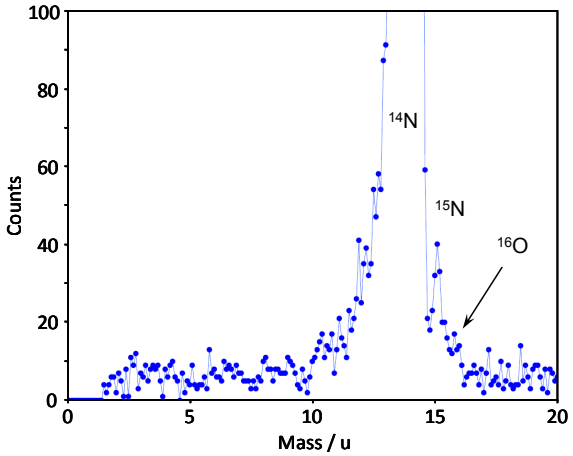

Fig. 2: *Heavy Ion ERDA mass spectrum of a Si_3N_4 layer on TiN. The O/N atomic ratio is smaller than 0.001.*

The measurements show that the analyzed films have very low oxygen concentrations of less than 0.02 at% in Si_3N_4 and below 0.2 at% in TiN. These films can therefore be considered oxygen-free, which is of great advantage to the XPS (X-ray Photoelectron Spectrometry) measurements performed at EMPA on these interfaces.

[1] S. Veprek, S. Reipric, Thin Solid Films 268 (1995) 64
[2] M. Disserens, J. Patscheider, F. Levy, Surf. Coat. Technol. 108/109 (1998) 241
[3] S. Veprek, M.G. Veprek-Hejman, Surf. Coat. Technol. 201 (2007) 6064

[1] *Nanoscale Materials, EMPA Dübendorf*

EVOLUTION OF NANOPOROSITY IN DE-ALLOYED FILMS

RBS analysis elucidates the de-alloying process in Pt-Al films

T. Ryll[1], H. Galinsk[1], F. Rechberger[1], S. Ying[1], L. Schlagenhauf[1], L.J. Gauckler[1], F. Mornaghini[1], R. Spolenak[1], M. Döbeli

Nanoporous platinum thin films show great promise for electrode applications. In this project the microstructural evolution of co-sputtered Pt-Al thin films during de-alloying is investigated. Aluminum atoms are preferentially removed from the initial Pt-Al alloy in the course of de-alloying, leaving a nanoporous network behind. Rutherford backscattering spectrometry (RBS) using 2 MeV ^{4}He ions is applied to a series of films, which have been de-alloyed for periods of 0 to 10 seconds in order to trace the time-dependency of this process.

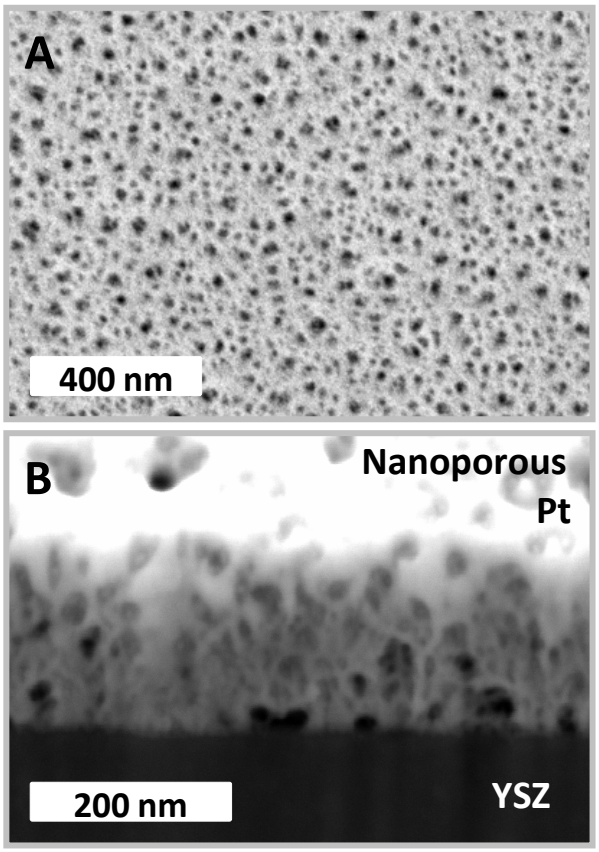

Fig. 1: *SEM images of a Pt-Al film de-alloyed for 10 s. (A) top-view, (B) cross-section; the substrate is yttria stabilized zirconia (YSZ).*

It was found that a well-defined de-alloying front develops passing perpendicularly through the thin film at a speed of around 30 nm/s. In Fig. 1, SEM images of a Pt-Al film after de-alloying for 10 s are shown. RBS spectra measured before and after de-alloying for 10 s are plotted in Fig. 2 showing that about 90 % of the Al atoms were removed.

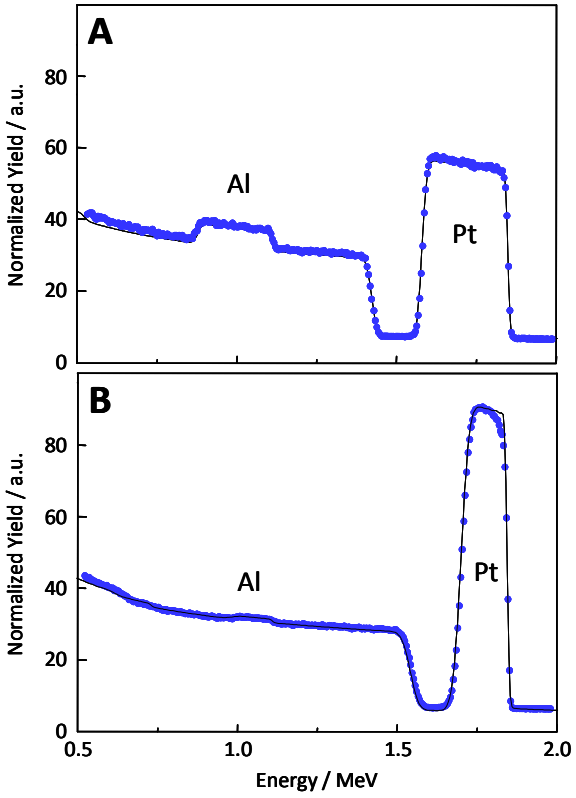

Fig. 2: *RBS spectra measured (A) before and (B) after de-alloying for 10 s.*

The electrode activity of the resulting nanoporous Pt thin films is determined by electrochemical impedance spectroscopy.

[1] *Dept. of Materials Sciences, ETHZ*

TRACING RUTHENIUM IN SPENT CATALYSTS

Depth profiles in Ru catalyst determined with RBS, ERDA and PIXE

M. Schubert[1], J. Wambach[1], M. Simon, M. Döbeli

Minor elements in a Ru loaded charcoal catalyst used for gasification of liquid biomass have been analyzed with RBS, ERDA and PIXE.

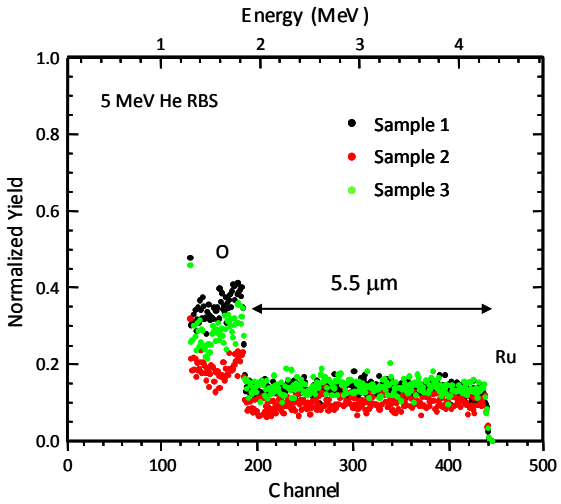

Fig. 1: *RBS concentration depth profiles of ground samples of the fresh (black) and spent (upstream (red) and downstream (green) of the catalyst bed) samples.*

Overall elemental concentrations in powder samples as well as Ru depth profiles were obtained by 2 and 5 MeV He RBS (Fig. 1).

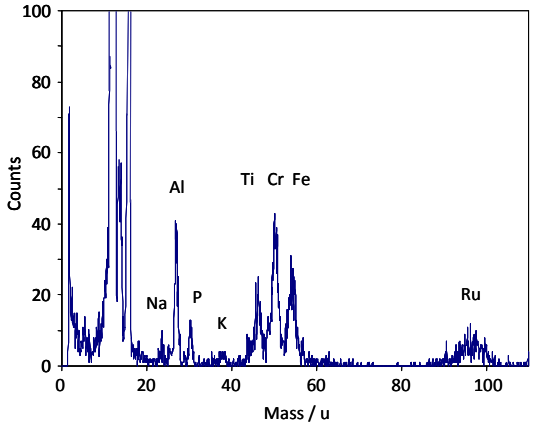

Fig. 2: *ERDA mass spectrum of topmost 100 nm of catalyst surface.*

Quantitative mass spectra of the material close to the surface of individual catalyst grains were measured with 13 MeV ^{127}I Heavy Ion ERDA (Fig. 2). For a more sensitive determination of trace elements, X-rays emitted during RBS analysis were recorded as well (PIXE measurement (Fig. 3).

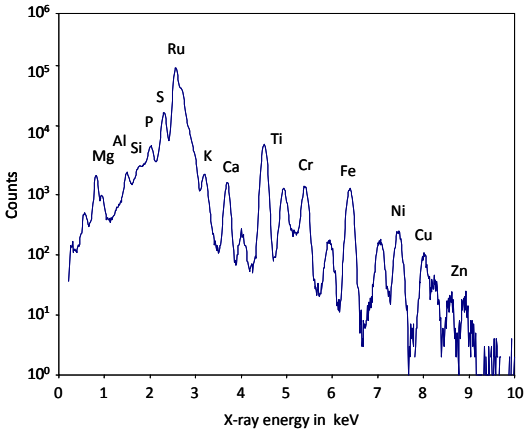

Fig. 3: *5 MeV He PIXE spectrum of a powder sample.*

The RBS measurements provide information on the ruthenium content and its distribution on the spent catalyst from different heights in the catalyst bed. The ERDA and PIXE measurements showed the deposition of corrosion products on the surface of the spent catalyst samples. These results were correlated to the observed catalyst deactivation [1].

[1] M. Schubert, Diss. ETH No. 19039 (2010)

[1] *Lab. for Energy and Materials Cycles, Paul Scherrer Institut, Villigen*

EDUCATION

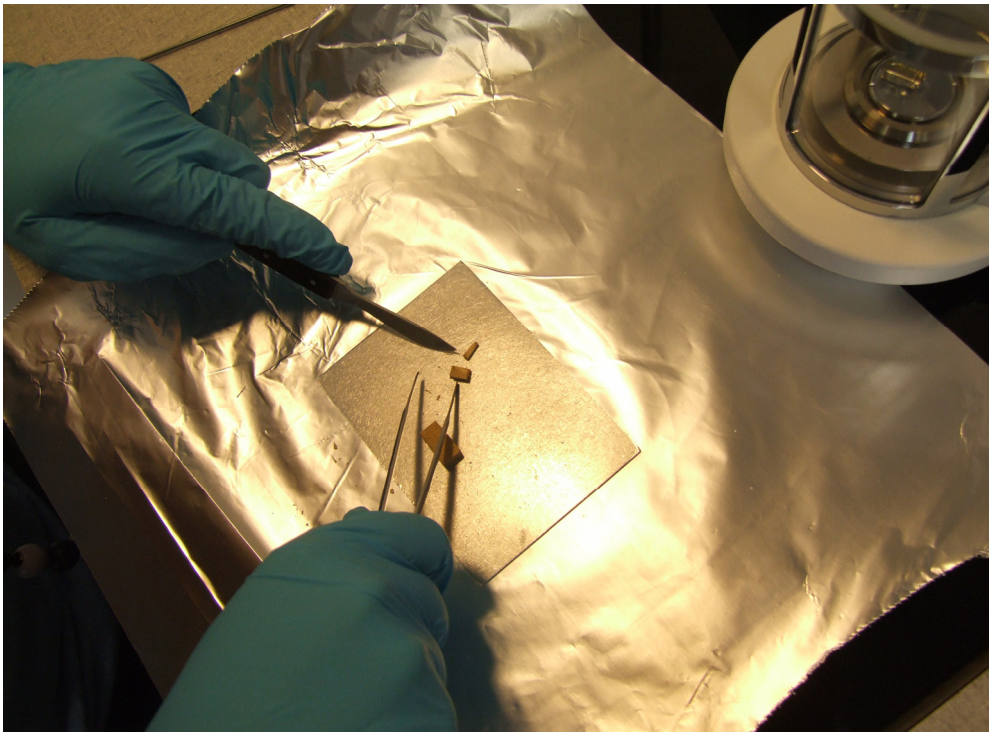

Radiocarbon dating for school projects

A gravitational capillary puller

RADIOCARBON DATING FOR SCHOOL PROJECTS

A one-week exchange between classroom and our AMS facility

I. Hajdas, G. Bonani, H.-A. Synal, C. Vockenhuber, L. Wacker

Each year, high-school students visit our laboratory and learn the basics of radiocarbon dating. The last year's visits included: two Matura projects, an ETH school project with 6 participants, and a project of the Kantonsschule Olten with 2 participants. During one week the participants completed the whole dating procedure (sampling and preparation as well measurement and data reduction).

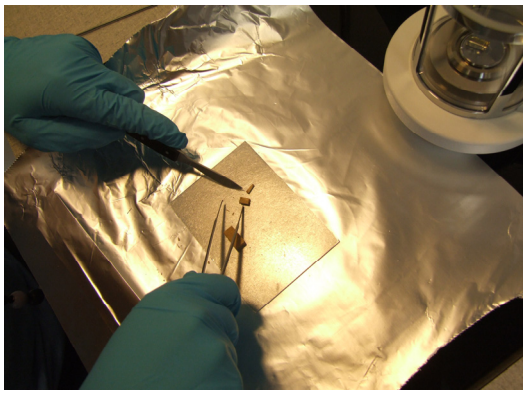

Fig. 1: *Samples of tree rings are cut and weighed for combustion and graphitization.*

During the ETH project week (June 2010) the team of 6 students sampled and prepared various materials. A slab of wood from a tree cut down in 2009 was cleaned and annual rings were counted back to 1939. Eleven annual samples were cut every 7 years for the reconstruction of the 'bomb peak'. Among the other prepared samples was an object presumably of historic origin, a piece of paper from a fan owned by the family of one of the students. According to the record, this fan was in the possession of the family in Riedlingen (Germany) where in the neighboring monastery of Obermarchtal **Marie Antoinette** rested in May 1770 AD during her travel to Paris to become Queen of France. This fan was probably a gift of the future queen or of someone close to her. The ^{14}C age of the paper supports the family story. Due to the complication of the calibration curve during the last 300 yrs ('wiggles'), calendar ages loose the precision of the ^{14}C measurements.

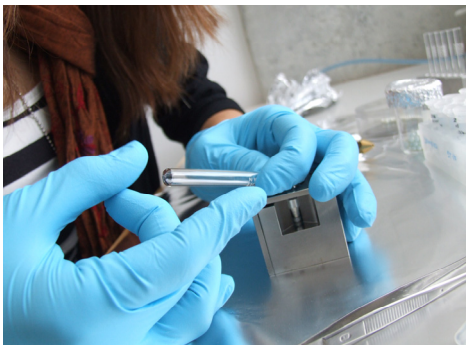

Fig. 2: *Graphite being pressed into the AMS target for measurement with MICADAS*

Using the known history of the sample (Terminus Ante Quem (TAQ) at 1770 AD) improves the calibration results. This example shows the importance of additional information (historical, other analyses) to constrain dating information of objects from 17th - 20th century. Although this will not proof authenticity, it can help to detect fraud.

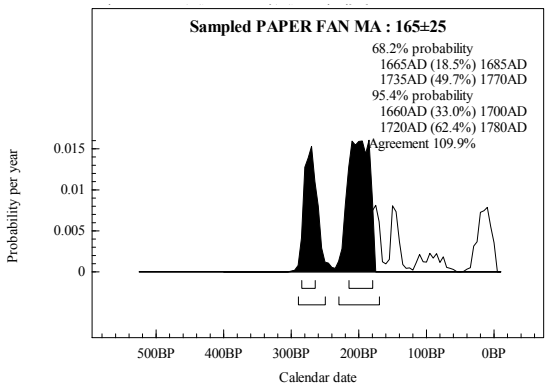

Fig. 3: *Calibration with OxCal 3.10 and TAQ shows that the most probable time for the material having been formed (grown) is between 1660 and 1780 AD.*

A GRAVITATIONAL CAPILLARY PULLER

Development of a puller for the capillary microprobe

M.J. Simon, J. Metzger, M. Döbeli, R. Gruber, A. Herrmann, S. Roost

To investigate the physics of the focusing effect of the glass capillaries in our microprobe (see further articles in this annual report), a variety of capillaries needs to be produced and tested. Commercially available capillary pullers offer only very limited possibilities to influence the shape of those capillaries. Therefore, a puller adapted to the specific needs of our capillary microprobe was developed as part of an apprenticeship final examination project.

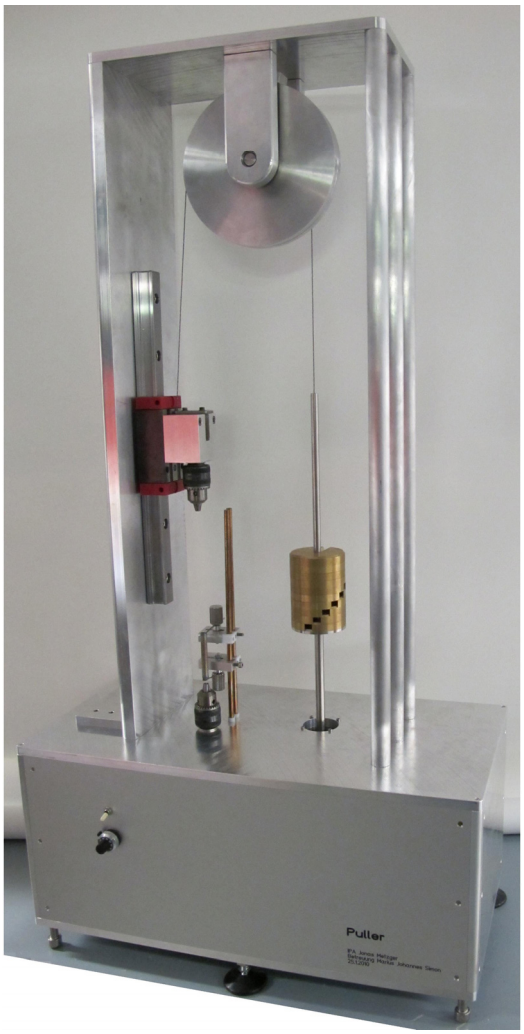

Fig. 1: *The gravitational capillary puller.*

The device (Fig. 1) uses gravitation as the pulling force. The advantage over e.g. a magnetic pulling force, which is utilized in most commercial pullers, is that long pulling distances can be achieved easily and at low cost. The force can be adjusted simply using different weights.

Most commercially available pullers work in the horizontal or pull the capillary downwards which often leads to bent capillary tips. To alleviate this problem, our device is designed to pull the capillaries upwards via a single pulley, which can be seen in the upper part of Fig. 1.

In addition, heating elements of different lengths and diameters can be used to soften the glass. A 500 W power supply was selected with heating elements of up to 10 cm lengths. The combination of a long heating element and the long pulling distance enable the production of very conical capillaries as can be seen in Fig. 2. Such capillaries cannot be produced with other pullers and are now often used with our microprobe.

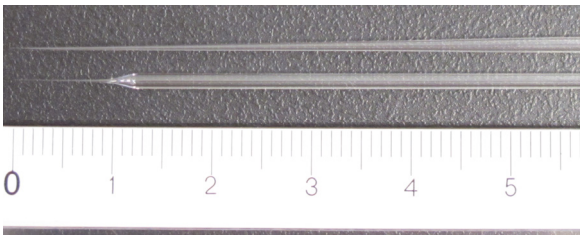

Fig. 2: *Capillaries of many different forms, e.g. cone- (top) or funnel-shaped (bottom) can be produced with the gravitational puller.*

PUBLICATIONS

V. Alfimov and H.-A. Synal
^{129}I AMS at 0.5 MV tandem accelerator
Nuclear Instruments and Methods B **268** (2010) 769-772

T. Bisinger, S. Hippler, R. Michel, L. Wacker and H.-A. Synal
Determination of plutonium from different sources in environmental samples using alpha-spectrometry and AMS
Nuclear Instruments and Methods B **268** (2010) 1269-1272

E. Chamizo, M. Garcia-Leon, S.M. Enamorado, M.C. Jimenez-Ramos and L. Wacker
Measurement of plutonium isotopes ^{239}P and ^{240}Pu in air-filter samples from Seville (2001-2002)
Atmospheric Environment **44** (2010) 1851-1858

M. Christl, J. Lippold, A. Hofmann, L. Wacker, Y. Lahaye and H.-A. Synal
^{231}Pa/^{230}Th: A proxy for upwelling off the coast of West Africa
Nuclear Instruments and Methods B **268** (2010) 1159-1162

M. Christl, J. Lippold, F. Steinhilber, F. Bernsdorff and A. Mangini
Reconstruction of global ^{10}Be production over the past 250 ka from highly accumulating Atlantic drift sediments
Quaternary Science Reviews **29** (2010) 2663-2672

M. Christl, C. Maden, P.W. Kubik, A.M. Müller, S. Ivy-Ochs, M. Suter and H.-A. Synal
Carrier-free measurements of natural ^{10}Be/^{9}Be ratios at low energies
Nuclear Instruments and Methods B **268** (2010) 726-729

L. de Abreu Vieira, M. Döbeli, A. Dommann, E. Kalchbrenner, A. Neels, J. Ramm, H. Rudigier, J. Thomas and B. Widrig
Approaches to influence the microstructure and the properties of Al-Cr-O layers synthesized by cathodic arc evaporation
Surface and Coatings Technology **204** (2010) 1722-1728

A. Dehnert, F. Preusser, J.D. Kramers, N. Akcar, P.W. Kubik, R. Reber and C. Schlüchter
A multi-dating approach applied to proglacial sediments attributed to the Most Extensive Glaciation of the Swiss Alps
Boreas **39** (2010) 620-632

M. Egli, D. Brandova, R. Böhlert, F. Favilli and P.W. Kubik
^{10}Be inventories in Alpine soils and their potential for dating land surfaces
Geomorphology **119** (2010) 62-73

L. Erikson, C. Ruiz, F. Ames, P. Bricault, L. Buchmann, A.A. Chen, J. Chen, H. Dare, B. Davids, C. Davis, C.M. Deibel, M. Dombsky, S. Foubister, N. Galinski, U. Greife, U. Hager, A. Hussein, D.A. Hutcheon, J. Lassen, L. Martin, D.F. Ottewell, C.V. Ouellet, G. Ruprecht, K. Setoodehnia, A.C. Shotter, A. Teigelhofer, C. Vockenhuber, C. Wrede and A. Wallner
First direct measurement of the Mg-23(p,γ)Al-24 reaction
Physical Review C **81** (2010) 045808-1 – 045808-12

S.M. Fahrni, H.W. Gäggeler, I. Hajdas, M. Ruff, S. Szidat and L. Wacker
Direct measurements of small ^{14}C samples after oxidation in quartz tubes
Nuclear Instruments and Methods B **268** (2010) 787-789

S.M. Fahrni, M. Ruff, L. Wacker, N. Perron, H.W. Gäggeler and S. Szidat
A preparative 2D-chromatography method for compound-specific radiocarbon analysis of dicarboxylic acids in aerosols
Radiocarbon **52** (2010) 752-760

I. Hajdas and A. Michczynski
Age-depth model of Lake Soppensee (Switzerland) based on ^{14}C chronology compared with varve chronology
Radiocarbon **52** (2010) 1027-1040

S. Harrison, N. Glasser, E. Anderson, S. Ivy-Ochs and P.W. Kubik
Late Pleistocene mountain glacier response to North Atlantic climate change in southwest Ireland
Quaternary Science Reviews **29** (2010) 3948-3955

S. Heiroth, T. Lippert, A. Wokaun, M. Döbeli, J.L.M. Rupp, B. Scherrer and L.J. Gauckler
Yttria-stabilized zirconia thin films by pulsed laser deposition: Microstructural and compositional control
Journal of the European Ceramic Society **30** (2010) 489-495

S. Ivy-Ochs and M. Schaller
Examining processes and rates of landscape change with cosmogenic radionuclides
In: Froehlich, K. (Editor) Environmental Radionuclides – Tracers and Timers of Terrestrial Processes. Elsevier, Amsterdam (2010) 232-294

P.W. Kubik and M. Christl
^{10}Be and ^{26}Al measurements at the Zurich 6 MV Tandem AMS facility
Nuclear Instruments and Methods B **268** (2010) 880-883

G. Kuri, C. Degueldre, J. Bertsch and M. Döbeli
Structural investigations in helium implanted cubic zirconia using grazing incidence XRD and EXAFS spectroscopy
Nuclear Instruments and Methods B **268** (2010) 2177-2180

J. Lachner, M. Christl, T. Bisinger, R. Michel and H.-A. Synal
Isotopic signature of plutonium at Bikini atoll
Applied Radiation and Isotopes **68** (2010) 979-983

A. Mangini, J.M. Godoy, M.L. Godoy, R. Kowsmann, G.M. Santos, M. Ruckelshausen, A. Schroeder-Ritzrau and L. Wacker
Deep sea corals off Brazil verify a poorly ventilated Southern Pacific Ocean during H2, H1 and the Younger Dryas
Earth and Planetary Science Letters **293** (2010) 269-276

D.J. Michczynska and I. Hajdas
Frequency distribution of ^{14}C ages for chronostratigraphic reconstructions: Alaska region study case
Radiocarbon **52** (2010) 1041-1055

A.D. Mueller, G.A. Islebe, F.S. Anselmetti, D. Ariztegui, M. Brenner, D.A. Hodell, I. Hajdas, Y. Hamann, G.H. Haug and D.J. Kennett
Recovery of the forest ecosystem in the tropical lowlands of northern Guatemala after disintegration of Classic Maya polities
Geology **38** (2010) 523-526

A.M. Müller, M. Christl, M. Döbeli, P.W. Kubik, M. Suter and H.-A. Synal
Boron suppression with a gas ionization chamber at very low energies (E < 1 MeV)
Nuclear Instruments and Methods B **268** (2010) 843-846

A.M. Müller, M. Christl, J. Lachner, M. Suter and H.-A. Synal
Competitive ^{10}Be measurements below 1 MeV with the upgraded ETH-TANDY AMS facility
Nuclear Instruments and Methods B **268** (2010) 2801-2807

M. Němec, L. Wacker and H.W. Gäggeler
Optimization of the graphitization process at AGE-1
Radiocarbon **52** (2010) 1380-1393

N. Němec, L. Wacker, I. Hajdas and H. Gäggeler
Alternative methods for cellulose preparation for AMS measurement
Radiocarbon **52** (2010) 1358-1370

K.P. Norton, F. von Blanckenburg and P.W. Kubik
Cosmogenic nuclide-derived rates of diffusive and episodic erosion in the glacially sculpted upper Rhone valley, Swiss Alps
Earth Surface Processes and Landforms **35** (2010) 651-662

T. Orlowski, O. Forstner, R. Golser, W. Kutschera, S. Merchel, M. Martschini, A. Priller, P. Steier, C. Vockenhuber and A. Wallner.
Comparison of detector systems for the separation of ^{36}Cl and ^{36}S with a 3-MV tandem
Nuclear Instruments and Methods B **268** (2010) 847-850

S. Orre, J.N. Smith, V. Alfimov and M. Bentsen
Simulating transport of I-129 and idealized tracers in the northern North Atlantic Ocean
Environmental Fluid Mechanics **10** (2010) 213-233

N. Perron, S. Szidat, S. Fahrni, M. Ruff, L. Wacker, A.S.H. Prévôt and U. Baltensperger
Towards on-line ^{14}C analysis of carbonaceous aerosol fractions
Radiocarbon **52** (2010) 761-768

M.K. Pham, M. Betti, P.P. Povinec, V. Alfimov, D. Biddulph, J. Gastaud, W.E. Kieser, J.M.L. Gutierrez, G. Possnert, J.A. Sanchez-Cabeza and T. Suzuki
Certified reference material IAEA-418: ^{129}I in Mediterranean seawater
Journal of Radioanalytical and Nuclear Chemistry **286** (2010) 121-127

J. Ramm, A. Neels, B. Widrig, M. Döbeli, L. de Abreu Vieira, A. Dommann, H. Rudigier
Correlation between target surface and layer nucleation in the synthesis of Al–Cr–O coatings deposited by reactive cathodic arc evaporation
Surface & Coatings Technology **205** (2010) 1356–1361

K. Rodrigo, S. Heiroth, M. Döbeli, N. Pryds, S. Linderoth, J. Schou and T. Lippert
Factors controlling the microstructure of $Ce_{0.9}Gd_{0.1}O_{2-\delta}$ films in pulsed laser deposition process
Journal of Optoelectronics and Advanced Materials **12** (2010) 511-517

M. Ruff, S. Szidat, H.W. Gäggeler, M. Suter, H.-A. Synal and L. Wacker
Gaseous radiocarbon measurements of small samples
Nuclear Instruments and Methods B **268** (2010) 790-794

A. Ruiz-Gómez, E. Chamizo-Calvo, J.M. López-Gutierrez, M. García-León, A.M. Müller and M. Christl
On the measurement of ^{10}Be on the 1 MV compact AMS system at the Centro Nacional de Aceleradores (Spain)
Nuclear Instruments and Methods B **268** (2010) 733-735

A.L. Sallaska, C. Wrede, A. Garcia, D.W. Storm, T.A.D. Brown, C. Ruiz, K.A. Snover, D.F. Ottewell, L. Buchmann, C. Vockenhuber, D.A. Hutcheon and J.A. Caggiano
Direct deasurements of ^{22}Na (p,γ) ^{23}Mg resonances and consequences for ^{22}Na production in classical novae
Physical Review Letters **105** (2010) 15025-1 – 15025-4

C.W. Schneider, M. Esposito, I. Marozau, K. Conder, M. Döbeli, Yi Hu, M. Mallepell, A. Wokaun and Th. Lippert
The origin of oxygen in oxide thin films - Role of the substrate
Applied Physics Letters **97** (2010) 192107

T. Schulze-König, S.R. Dueker, J. Giacomo, M. Suter, J.S. Vogel and H.-A. Synal
BioMICADAS: Compact next generation AMS system for pharmaceutical science
Nuclear Instruments and Methods B **268** (2010) 891-894

T. Schulze-König, C. Maden, E. Denk, S.P.H.T. Freeman, M. Stocker, M. Suter, H.-A. Synal and T. Walczyk
Comparison of ^{41}Ca analysis on 0.5 MV and 5 MV-AMS systems
Nuclear Instruments and Methods B **268** (2010) 752-755

C.D. Shen, J. Beer, P.W. Kubik, W.D. Sun, T.S. Liu and K.X. Liu
^{10}Be in desert sands, falling dust and loess in China
Nuclear Instruments and Methods B **268** (2010) 1050-1053

F. Simmen, T. Lippert, P. Novak, M. Horisberger, M. Döbeli, M. Mallepell and A. Wokaun
Influence of metal layer coated glassy carbon substrates on the properties of PLD deposited $Li_{1+x}Mn_2O_{4-\delta}$ films
Journal of Optoelectronics and Advanced Materials **12** (2010) 523-527

M. Suter
Challenging developments in three decades of accelerator mass spectrometry at ETH: from large particle accelerators to table size instruments
European Journal of Mass Spectrometry **16** (2010) 471-478

M. Suter, E. Chamizo, A.M. Müller and H.-A. Synal
The relevance of ion optics for the development of small AMS facilities
Nuclear Instruments and Methods B **268** (2010) 722-725

M. Suter, A.M. Müller, V. Alfimov, M. Christl, T. Schulze-König, P.W. Kubik, H.-A. Synal, C. Vockenhuber and L. Wacker
Are compact AMS facilities a competitive alternative to larger Tandem accelerators?
Radiocarbon **52** (2010) 319-330

P. Steier, O. Forstner, R. Golser, W. Kutschera, M. Martschini, S. Merchel, T. Orlowski, A. Priller, C. Vockenhuber and A. Wallner
^{36}Cl exposure dating with a 3-MV tandem
Nuclear Instruments and Methods B **268** (2010) 744-747

P. Steier, F. Dellinger, O. Forstner, R. Golser, K. Knie, W. Kutschera, A. Priller, F. Quinto, M. Srncik, F. Terrasi, C. Vockenhuber, A. Wallner, G. Wallner and E. M. Wild.
Analysis and application of heavy isotopes in the environment.
Nuclear Instruments and Methods B **268** (2010) 1045-1049

H.-A. Synal and L. Wacker
AMS measurement technique after 30 years: Possibilities and limitations of low energy systems
Nuclear Instruments and Methods B **268** (2010) 701-707

A. Tempez, S. Canulescu, I.S. Molchan, M. Döbeli, J.A. Whitby, L. Lobo, J. Michler, G.E. Thompson, N. Bordel, P. Chapon, P. Skeldon, I. Delfanti, N. Tuccitto and A. Licciardello
^{18}O/^{16}O isotopic separation in anodic tantala films by glow discharge time-of-flight mass spectrometry
Surface and Interface Analysis **41** (2010) 966–973

A. Trita, F. Bragheri, I. Cristiani, V. Degiorgio, D. Chrastina, D. Colombo, G. Isella, H. von Känel, F. Gramm, E. Müller, M. Döbeli, E. Bonera, R. Gatti, F. Pezzoli, E. Grilli, M. Guzzi, L. Miglio
Impact of misfit dislocations on wavefront distortion in Si/SiGe/Si optical waveguides
Optics Communications **282** (2010) 4716–4722

L. Wacker, G. Bonani, M. Friedrich, I. Hajdas, B. Kromer, M. Nemec, M. Ruff, M. Suter, H.-A. Synal and C. Vockenhuber
MICADAS: routine and high-precision radiocarbon dating
Radiocarbon **52** (2010) 252-262

L. Wacker, M. Christl and H.-A. Synal
Bats: A new tool for AMS data reduction
Nuclear Instruments and Methods B **268** (2010) 976-979

L. Wacker, M. Nemec and J. Bourquin
A revolutionary graphitisation system: Fully automated, compact and simple
Nuclear Instruments and Methods B **268** (2010) 931-934

A. Wallner, O. Forstner, R. Golser, G. Korschinek, W. Kutschera, A. Priller, P. Steier and C. Vockenhuber
Fluorides or hydrides? - ^{41}Ca performance at VERA's 3-MV AMS facility
Nuclear Instruments and Methods B **268** (2010) 799-803

H. Wittmann, F. von Blanckenburg, J.L. Guyot, A. Laraque, C. Bernal and P.W. Kubik
Sediment production and transport from in situ-produced cosmogenic ^{10}Be and river loads in the Napo River basin, an upper Amazon tributary of Ecuador and Peru
Journal of South American Earth Sciences **31** (2010) 45-53

C. Zahno, N. Akcar, V. Yavuz, P.W. Kubik and C. Schlüchter
Chronology of Late Pleistocene glacier variations at the Uludag Mountain, NW Turkey
Quaternary Science Reviews **29** (2010) 1173-1187

J. Zech, R. Zech, J.H. May, P.W. Kubik and H. Veit
Lateglacial and early Holocene glaciation in the tropical Andes caused by La Nina-like conditions
Palaeogeography Palaeoclimatology Palaeoecology **293** (2010) 248-254

TALKS AND POSTERS

V. Alfimov, S. Ivy-Ochs, P.W. Kubik, J. Beer and H.-A. Synal
^{36}Cl concentration in 100-m long limestone core from Vue des Alpes, Switzerland
Germany, Hannover, 10.03.2010, DPG Conference

V. Alfimov, N. Akcar, S. Ivy-Ochs and C. Schlüchter
Dating earthquake faults with cosmogenic ^{36}Cl
Switzerland, Biel, 13.08.2010, Federal Nuclear Safety Commission

M. Christl
Anwendung moderner Massenspektrometer zum Verständnis von Klimaarchiven
Germany, Heidelberg, 25.-26.01.2010, Symposium: Physik der Umweltarchive, Uni-Heidelberg

M. Christl, J. Lippold, F. Steinhilber, F. Bernsdorff and A. Mangini
Geomagnetic modulation extracted from cosmogenic ^{10}Be in highly accumulating Atlantic drift deposits
Austria, Vienna, 2.–7.05.2010, EGU General Assembly 2010

M. Christl, C. Münsterer and A. Mangini
An investigation of the evapotranspiration at Bunker Cave (NW Germany) with ^{36}Cl
Austria, Innsbruck/Kranebitten, 30.06.-02.07.2010, Daphne II international workshop

M. Christl
AMS an den Enden der Nuklidkarte - Anwendungsbeispiele aus dem Ozean
Germany, Cologne, 10.07.2010, 2nd User Workshop Cologne-AMS

M. Christl, J. Lachner, C. Vockenhuber and H.-A. Synal
U-236 in ocean water samples
Italy, Rome, 25.-28.10.2010, International Conference on Environmental Radioactivity

M. Döbeli
Ionisierende Strahlung
Switzerland, Zurich, 14.04.2010, Seminar Series Ion Beam Physics ETH Zurich

M. Döbeli
Radiation-hard gas ionization detectors for IBA
USA, Fort Worth, 11.08.2010, Conference on the Application of Accelerators in Research and Industry

M. Döbeli
Gas ionization detectors for ERDA, RBS and STIM
Plitvice, Croatia, 24.10.2010, European workshop on new detector technologies

M. Egli, D. Brandova, R. Böhlert, F. Favilliand and P.W. Kubik
10Be inventories in Alpine soils and their potentiality for dating land surfaces
Austria, Vienna, 2.-7.05.2010, EGU General Assembly 2010

C.R. Fenton, R. Hermanns, L. Blikra, P.W. Kubik, C.Bryant, S. Niedermann, A. Meixner and M. Goethals
Regional ^{10}Be production rate calibration for the past 12 ka deduced from two radiocarbon-dated rock avalanches at 69° N, Norway
Austria, Vienna, 2.-7.05.2010, EGU General Assembly 2010

R. Frauenfelder, H. Farbrot, K. Isaksen, D. Brandova, M. Egli and P.W. Kubik
Surface exposure dating of a rock glacier in the Gaissane Mountains, northern Norway: Shedding new light on the regions glacial history?
Norway, Svalbard, 2.-4.06.2010, 3rd European Permfrost Conference

I .Hajdas
Radiocarbon chronologies of lake sediments—an overview
Austria, Vienna, 28.01.2010, Seminar at VERA

I. Hajdas and A. Michczynski
Varve chronology of Lake Soppensee (CH) compared with the age-depth model based on the high resolution ^{14}C chronology
Estonia, Tallin, 7.-9.04.2010, 1st Meeting of PAGES Varve Chronologies Working Group

I. Hajdas and A. Michczynski
Closed tubes preparation of graphite for high-precision AMS radiocarbon analysis
Poland, Gliwice, 22.-25.04.2010, 10th Absolute Chronologies Meeting

I. Hajdas and A. Michczynski
Varve chronology of Lake Soppensee (CH) compared with the age-depth model based on the high resolution ^{14}C chronology
Poland, Gliwice, 22.-25.04.2010, 10th Absolute Chronologies Meeting

R. Hebenstreit, S. Ivy-Ochs, P.W. Kubik and M. Böse
Latest Pleistocene and early Holocene surface exposure ages of glacial boulders in the Taiwanese high mountain range
Austria, Vienna, 2.-7.05.2010, EGU General Assembly 2010

K. Hippe, F. Kober, G. Zeilinger, S. Ivy-Ochs, P.W. Kubik, C. Maden and R. Wieler
Evaluating processes and rates of surface denudation at the Eastern Altiplano margin, Bolivia
Austria, Vienna, 2.-7.05.2010, EGU General Assembly 2010

A. Hormes, N. Akçar and P.W. Kubik
Ice sheet configurations during MIS-4 and MIS-2 on Nordaustlandet, Svalbard
Austria, Vienna, 2.-7.05.2010, EGU General Assembly 2010

S. Ivy-Ochs
Glaciations of the Alps
Switzerland, Zurich, 17.03.2010, Seminar Series Ion Beam Physics ETH Zurich

S. Ivy-Ochs
Deciphering landscape change in the Alps after the LGM with cosmogenic nuclides
France, Grenoble, 22.06.2010, Seminar Department of Geology, University of Grenoble

S. Ivy-Ochs
Post-LGM landscape change in the Alps
Switzerland, Zurich, 20.09.2010, Seminar Department of Geography, University of Zurich

D. Kiselev, Y. Dai, S. Lüthi, J. Neuhausen, D. Schumann, V. Alfimov, P.W. Kubik and H.-A. Synal
Nuclide inventory in proton irradiated lead - comparison of simulation and measurement
Switzerland, Geneva, 2.-4.06.2010, NEA Workshop on Shielding of Accelerators, Targets and Irradiation Facilities (SATIF-10), CERN

J. Kuhlemann, M. Pfähler, I. Krumrei, C. Schuster, S. Ivy-Ochs and P.W. Kubik
Late Holocene rockfall in Corsica: Causes and triggers
Germany, Frankfurt/Darmstadt, 10.-13.10.2010, Jubiläumstagung der Geologischen Vereinigung

J. Lachner
Direkte Bestimmung von natürlichen $^{10}Be/^{9}Be$-Verhältnissen am Tandy
Germany, Hannover, 10.03.2010, DPG Conference

J. Lachner
Aktinide-Messungen am „upgraded" Tandy
Germany, Hannover, 10.03.2010, DPG Conference

J. Lachner and M. Christl
The ^{10}Be isotopic signature of the Brunhes/Matuyama field reversal from marine sediments
Austria, Vienna, 2.-7.05.2010, EGU General Assembly 2010

J. Lachner, V. Alfimov, M. Christl, P.W. Kubik, T. Schulze-König, I. Hajdas, L. Wacker and H.-A. Synal
Ca-41, C-14, and Be-10 concentration in coral $CaCO_3$ from the nuclear test site Bikini Atoll determined with low energy AMS
Italy, Rome, 25.-28.10.2010, International Conference on Environmental Radioactivity

A.M. Müller
Das 600 kV AMS System mit zusätlichem 130° Ablenkmagneten
Germany, Hannover, 10.03.2010, DPG Conference

A.M. Müller
Mini gas ionization chambers for IBA applications
Greece, Athens, 17.09.2010, ECAART-10 Conference

A.M. Müller and M. Döbeli
Surface ersosion during heavy ion backscattering analysis
Greece, Athens, 17.09.2010, ECAART-10 Conference

T.M. Rosenberg, F. Preusser, D. Fleitmann, A. Schwalb, K. Penkman, I. Hajdas, M. Alshanti, K. Khadi and A. Matter
Humid periods on Arabia - time windows for out of Africa migration of modern humans
United Kingdom, Oxford, 8.-10.09.2010, TL/OSL/ESR Meeting

I. Schindelwig, N. Akcar, S. Lukas, P.W. Kubik and C. Schlüchter
Glacier activity at the Lateglacial/Holocene transition inferred from the Swiss Alps
Austria, Vienna, 2.-7.05.2010, EGU General Assembly 2010

M. Seiler
Zerstörungswirkungsquerschnitte von Kohlenstoffmolekülen in Stickstoff
Switzerland, Zurich, 3.03.2010, Seminar Series Ion Beam Physics ETH Zurich

M. Seiler, T. Schulze-König and H.-A. Synal
Zerstörungswirkungsquerschnitte von Kohlenstoffmolekülen in Stickstoff
Germany, Hannover, 10.03.2010, DPG Conference

M. Seiler
Low Energy AMS and Helium Stripping
Switzerland, Zurich, 30.08.2010, PhD Seminar ETHZ

T. Schulze-König
Direct Radiocarbon Analysis of CO_2 samples
Germany, Hannover, 10.03.2010, DPG Conference

M.J. Simon, M. Döbeli and A.M. Müller
Capillary Microprobe
Germany, Leipzig, 26.-27.07.2010, ICNMTA 2010

M.J. Simon
Capillary Microprobe
Switzerland, Zurich, 30.08.2010, PhD Seminar ETHZ

M.J. Simon
Development of a Capillary Microprobe
Switzerland, Zurich, 15.12.2010, Seminar Series Ion Beam Physics ETH Zurich

M. Suter
High precision radiocarbon dating: From large AMS facilities to table size instruments
France, Aix-en-Provence, 26.05.2010, Seminar

M. Suter
How can we optimize AMS facilities?
Greece, Athens, 17.09.2010, ECAART-10 Conference

H.-A. Synal
Perspectives of Accelerator Mass Spectrometry (AMS)
Denmark, Copenhagen, 8.10.2010, Kick-off meeting: The Danish Green Magent Project, Danfysik

H.-A. Synal
Accelerator Mass Spectrometry and its Potential for Applications in Biomedical Sciences
Italy, Florence, 9.11.2010, Mass Spectrometry Europe Conference

C. Vockenhuber, M. Döbeli and A. Wallner
The potential of Accelerator Secondary Ion Mass Spectrometry for astrophysical applications
Germany, Hannover, 10.03.2010, DPG Conference

C. Vockenhuber
Astrophysics with ion beams
Switzerland, Basel, 16.04.2010, Doctoral Research Group Basel-Graz-Tübingen

C. Vockenhuber, M. Christl, J. Lachner, D. Meister, A.M. Müller and H.-A. Synal
Accelerator Mass Spectrometry of ^{236}U at low energies
Greece, Athens, 17.09.2010, ECAART-10 Conference

C. Vockenhuber and D. Güttler
The use of AMS for isotopic analysis of pre-solar materials and for the search of SN-produced r-process nuclides ^{182}Hf and ^{244}Pu
Croatia, Dubrovnik, 25.11.2010, First EUROGENESIS Workshop

C. Vockenhuber
Measurements of energy-loss straggling and its relevance for Accelerator Mass Spectrometry
Denmark, Odense, 29.11.2010, Mini-Symposium on Particle Penetration and Radiation Effects

L. Wacker
Pushing the limits of high-precision radiocarbon measurements
Austria, Vienna, 15.04.2010, Seminarvortrag at VERA

H. Wiesel, G. Delisle, B. Kuczewski, P.W. Kubik, U. Otto, U. Herpers
Glaciation history of Queen Maud Land (Antarctica) - new exposure ages from nunataks
Austria, Obergurgl, 6.-10-9.2010, 24. International Polar Meeting

H. Wittmann, F. von Blanckenburg, L. Maurice, J.-L. Guyot and P.W. Kubik
Old sediment in young rivers – a multiple cosmogenic nuclide study in the Amazon basin
Austria, Vienna, 2.-7.05.2010, EGU General Assembly 2010

J. Zech, R. Zech, P.W. Kubik and H. Veit
A high-altitude calibration site for 10Be surface exposure dating at Tres Lagunas, NW-Argentina
Austria, Vienna, 2.-7.05.2010, EGU General Assembly 2010

SEMINAR 'AKTUELLE THEMEN AUS DER BESCHLEUNIGERMASSEN-SPEKTROMETRIE UND DEREN ANWENDUNGEN'

Spring semester

24.02.2010
V. Levchenko (ANSTO, Australia), *A bright future for accelerator science at ANSTO*

03.03.2010
Martin Seiler (ETHZ, Switzerland), *Molekülzerstörung bei tiefen Energien*
Daniel Meister (ETHZ, Switzerland), *U-236 am Tandy - erste Daten*

17.03.2010
Susan Ivy-Ochs (ETHZ/University of Zurich), *Glaciation of the Alps*

24.03.2010
Lukas Emmenegger (EMPA, Switzerland), *Quantum cascade laser spectroscopy for CO_2 and N_2O isotopes in environmental research*

31.03.2010
Kevin Norton (University of Bern, Switzerland), *Do mountains really accelerate weathering? Insights from ^{10}Be and Zr in stream sediments and soils*

07.04.2010
Sebastian Raeder (Unversity of Mainz, Germany), *Isotopenselektiver Nachweis von Uran mit hochauflösender Resonanzionisations-Massenspektrometrie*

14.04.2010
Max Döbeli (ETHZ, Switzerland), *Ionisierende Strahlung*

21.04.2010
Irka Hajdas (ETHZ, Switzerland), *Development of timescales*

28.04.2010
Fortunat Joos (University of Bern, Switzerland), *CO_2 und ^{14}C im Klimasystem: einige Beispiele*

12.05.2010
Werner Aeschbach-Hertig (University of Heidelberg, Germany), *Paläoklima aus Grundwasser in China*

26.05.2010
Dirk Hoffmann (University of Bristol, Great Britain), *Radiocarbon calibration and stalagmites*

02.06.2010
Lukas Wacker (ETHZ, Switzerland), *Verbesserung der C-14 Kalibrierkurve*

09.06.2010
Caglar Özkaymak (University of Bern, Switzerland), *Active tectonics of western Anatolia; examples from Manisa Fault Zone*

Fall semester

22.09.2010
Benny Guralnik (ETHZ, Switzerland), *Constraining rift margin subsidence and young fluvial phases in the hyperarid Negev Desert using ^{10}Be*

29.09.2010
Raimund Muscheler (Lund University, Sweden), *Reconstruction of past changes in galactic cosmic ray intensity based on cosmogenic radionuclides - on influencing factors and reliability*

06.10.2010
Hella Wittmann (GFZ Potsdam, Germany), *The Amazon basin: Deciphering sediment transport from in-situ and meteoric 10Be measured in river sand*

13.10.2010
Cornelia Hofmann (ETHZ, Switzerland), *Untergrunduntersuchung von U-236 am Tandy mittels ToF*
Johannes Lachner (ETHZ, Switzerland), *Über die Existenz von ThH^{3+} und UH^{3+} Molekülen*

20.10.2010
Dimitri Tikhomirov (University of Bern, Switzerland), *Ratio of ^{36}Cl/Cl in ground ice of east Siberia and its application for chronometry*

27.10.2010
Negar Haghipour (ETHZ, Switzerland), *Temporal-spatial correlation of fluvial terraces in Makran accretionary wedge (SE-IRAN) using cosmogenic nuclides*

03.11.2010
Caroline Münsterer (University of Heidelberg, Germany), *Eine Untersuchung der Evapotranspiration an der Bunkerhöhle mittels Chlor-36*

10.11.2010
Martin Seiler (ETHZ, Switzerland), *AMS mit He-Stripping*

17.11.2010
Naki Akcar (University of Bern, Switzerland), *^{10}Be production rate from 1717 AD rock avalanche in Val Ferret (Mont Blanc Massif, Italy)*

24.11.2010
James Kirchner (WSL, Switzerland), *Exploring the geochemistry of landscape dynamics using cosmogenic nuclides*

01.12.2010
Colin Maden (ETHZ, Switzerland), *Sofie, a charged particle optics software designed for thermal ionisation simulations*

02.12.2010
Karel Schrijver (Lockheed Martin Solar and Astrophysics Laboratory, USA), *Solar magnetic activity: the global view with the latest instrumentation, and lessons from the stars*

08.12.2010
Tim Schulze-König (ETHZ, Switzerland), *Ca-41 Markierung eines Schafskelett*

15.12.2010
Marius Simon (ETHZ, Switzerland), *Development of a capillary microprobe*

22.12.2010
Marcus Christl (ETHZ, Switzerland), *U-236 im Atlantischen Ozean*

THESES (INTERNAL)

Term papers

Cornelia Hofmann
Background analysis for AMS of ^{236}U at the ETH Tandy facility using time-of-flight detectors
ETH Zurich

Diploma/Master theses

Martin Seiler
Wirkungsquerschnitte für die Molekülzerstörung von $^{12}CH_2$ und ^{13}CH Molekülen im Energiebereich zwischen 80 und 250 keV
ETH Zurich

Doctoral theses

Tim Schulze-König
Advancements in Radiocarbon Mass Spectrometry
ETH Zurich, ETH No. 19285

Habilitation theses

Susan Ivy-Ochs
Surface exposure dating of glacial and periglacial landforms, and mass movements in the European Alps
ETH Zurich

THESES (EXTERNAL)

Term Papers

Luca Delacrétaz
Low Energy Ion Detectors
EPF Lausanne

Diploma/Master theses

Nadine Dannhaus
Erosionsraten und Sedimentverweilzeiten anhand von meteorischem, kosmogen-produziertem 10Be an Flusssediment des Amazonasbeckens
University of Hannover (Germany)

Michael Graf
Altersbestimmungen an neuzeitlichen Moränen mit Hilfe physisch-geographischer Datierungsmethoden am Berninapassgebiet
University of Zurich (Switzerland)

Reto Grischott
Environmental history of Lake Canova
ETH Zurich

Caroline Münsterer
Messung von ^{36}Cl in Regen- und Höhlentropfwässern
University of Heidelberg (Germany)

Katia Sanhueza-Pino
Datierung von Bergstürzen in Kirgisistan, nördlicher Tien Shan, mittels kosmogener Nuklide
University of Münster (Germany)

Ruedi Seiler
Stabile und labile organische Substanz in den Böden des Ätna (Sizilien) und ihre Beziehung zum Klima und zur Häufigkeit von Wald- und Buschbränden
University of Zurich (Switzerland)

Julian Wiesinger
Rekonstruktion der spätpleistozänen Vergletscherungsgeschichte des nordwestlichen Tian Shan
University of Bayreuth (Germany)

Stephan Wohlwend
Shoreline deposits around Lej da Segl (Upper Engadine, Switzerland) - Traces of a Prehistoric Tsunami?
ETH Zurich

Doctoral theses

Ralph Böhlert
Reconstructing Lateglacial and Early Holocene landscape evolution using a combination of numerical and relative dating methods - Examples from eastern Switzerland and eastern France
University of Zurich (Switzerland)

Filippo Favilli
Soil and Alpine landscape evolution since the Lateglacial and early/mid Holocene in Val di Sole (Trentino, Italy)
University of Zurich (Switzerland)

Sebastian Heiroth
Pulsed laser deposition of functional electroceramic thin films for micro solid oxide fuel cell applications
ETH Zurich, ETH No. 18885

Muhamed Niklaus
Metal-ion implanted elastomers: Analysis of microstructures and characterization and modeling of electrical and mechanical properties
EPF Lausanne, EPFL No. 4798

Nolwen Peron
Radiocarbon-supported source apportionment of carbonaceous aerosols
University of Bern (Switzerland)

Verma Rajneesh
Vacuum evaporated In_2S_3 buffer layer for Cu(In, Ga)Se_2 thin-film solar cell
ETH Zurich, ETH No. 19283

Inga Schindelwig
The Last glacial-Interglacial transition: An interval of high Alpine-glacier dynamics in the Central and Western Swiss Alps
University of Bern (Switzerland)

Schubert Martin
Catalytic hydrothermal gasification of biomass: Salt recovery and continuous gasification of glycerol solutions
ETH Zurich, ETH No. 19039

Franziska Simmen
Pulsed laser deposition zur Herstellung von Modellphasengrenzen für elektrochemische Untersuchungen
ETH Zurich, ETH No. 19092

COLLABORATIONS

Austria

AlpS - Zentrum für Naturgefahren- und Riskomanagement GmbH, Geology and Mass Movements, Innsbruck

Geological Survey of Austria, Sedimentary Geology, Vienna

University of Natural Resources and Life Sciences, Institute for Applied Geology, Vienna

University of Innsbruck, Institute of Geography, Innsbruck

University of Innsbruck, Institute of Geology, Innsbruck

University of Vienna, VERA, Faculty of Physics, Vienna

University of Vienna, Department of Geodynamics and Sedimentology, Vienna

Vienna University of Technology, Institute for Geology, Vienna

Belgium

University of Louvain, Department of Geography, Louvain

Royal Institute for Cultural Heritage, Brussels

Canada

Bedford Institute of Oceanography, Marine Environmental Sciences Division, Dartmouth

Chalk River Laboratories, Dosimetry Services, Ottawa

TRIUMF, Vancouver

Denmark

Syddansk Universitet, Department of Physics and Chemistry, Odense

France

University of Aix-Marseille, CEREGE, Aix-en-Provence

Germany

Albert-Ludwigs-Universität Freiburg, Freiburg

Alfred Wegener Institute of Polar and Marine Research, Department of Periglacial Research, Potsdam

Alfred Wegener Institute of Polar and Marine Research, Marine Geochemistry, Bremerhaven

BSH Hamburg, Radionuclide Section, Hamburg

Deutsches Bergbau Museum, Bochum

Federal Institute for Geosciences and Natural Resources, Hannover

General Direktion Kulturelles Erbe Rheinland-Pfalz, Direktion Landesarchäologie, Speyer

German Research Centre for Geosciences (GFZ), Potsdam

Hydroisotop GmbH, Schweitenkirchen

IFM-GEOMAR, Paleoceanography, Kiel

Max-Planck-Institut für Chemie, Abt. Geochemie, Mainz

Reiss-Engelhorn-Museum, Klaus-Tschira-Labor, Mannheim

Regierungspräsidium Stuttgart, Landesamt für Denkmalpflege, Esslingen

Research Center Dresden-Rossendorf, Dresden

TU Munich, Maier-Leibnitz-Laboratory, Munich

University of Bayreuth, Institute of Soil Science and Soil Geography, Bayreuth

University of Cologne, Geology, Cologne

University of Cologne, Theoretical Chemistry, Cologne

University of Cologne, Institute for Nuclear Chemistry, Cologne

University of Cologne, Institute of Geography, Cologne

University of Hannover, Center for Radiation Protection and Radioecology, Hannover

University of Heidelberg, Institute of Environmental Physics, Heidelberg

University of Hohenheim, Institute of Botany, Stuttgart

University of Kiel, Leibniz Institute for Marine Sciences, Kiel

University of Münster, Institute of Geology and Paleontology, Münster

University of Potsdam, Institute for Geosciences, Potsdam

University of Tuebingen, Department of Geosciences, Tübingen

Hungary

Hungarian Academy of Science, Institute of Nuclear Research (ATOMKI), Debrecen

Israel

Hebrew University, Geophysical Institute of Israel, Jerusalem

Italy

Geological Survey of the Provincia Autonoma di Trento, Landslide Monitoring, Trentino

University of Padua, Department of Geology and Geophysics, Padua

Universtiy of Turin, Department of Earth Sciences, Turin

Liechtenstein

Hochbauamt Triesen, Denkmalpflege / Archäologie, Triesen

OC Oerlikon AG, Balzers

Norway

Nansen Environmental and Remote Sensing Center & Bjerknes Centre for Climate Research, Bergen

The University Centre of Svalbard, Quaternary Geology, Longyearbyen

University of Bergen, Department of Earth Science, Bergen

Russia

St. Petersburg State Polytechnic University, Faculty of Physical Science and Technology, St. Petersburg

Singapore

National University of Singapore, Department of Chemistry, Singapore

South Africa

North-West University, School of Physics, Potchefstroom

Spain

University of Seville, National Center for Accelerators, Sevilla

Sweden

Lund University, Department of Earth and Ecosystem Sciences, Lund

Onsala Space Obervatory, Onsala

University of Stockholm, Department of Geological Sciences, Stockholm

Uppsala University, Department of Geology, Uppsala

Uppsala University, Tandem Laboratory, Uppsala

Switzerland

ABB Semiconductors AG

Dendrolabor Wallis, Brig

Empa, Dübendorf, High Performance Ceramics

Empa, Dübendorf, Functional Polymers

Empa, Dübendorf, Nanoscale Materials

Empa, Dübendorf, Thin Films

EPFL, Lausanne, Institute de Physique de la Matière Condensée

ETH Zurich, Institute of Geology, Zurich

ETH Zurich, Institute of Isotope Geochemistry and Mineral Resources, Zurich

ETH Zurich, Institute of Geochemistry and Petrology, Zurich

ETH Zurich, Institute of Food, Nutrition, and Health, Zurich

ETH Zurich, Geschäftsstelle Geotechnische Kommission, Zurich

Kanton Aargau, Kantonsarchäologie, Brugg

Kanton Bern, Achäologischer Dienst, Berne

Kanton Graubünden, Archäologischer Dienst, Chur

Kanton Solothurn, Kantonsarchäologie, Solothurn

Kanton St. Gallen, Kantonsarchäologie, St. Gallen

Kanton Zug, Kantonsarchäologie, Zug

Kanton Zürich, Kantonsarchäologie, Dübendorf

Labor für quartäre Hölzer, Affoltern a. Albis

Laboratiore Romand de Dendrochronologie, Moudon

Office et Musée d'Archéologie Neuchâtel, Neuchatel

Paul Scherrer Institut (PSI), Laboratory for Radiochemistry and Environmental Chemistry, Villigen

Paul Scherrer Institut (PSI), Laboratory for Atmospheric Chemistry, Villigen

Professeur d'archéologie préhistorique, Laténium - Parc et Musée d'archéologie, Hauterive

Research Station Agroscope Reckenholz-Tänikon ART, Air Pollution / Climate Group, Zurich

Stadt Zürich, Amt für Städtebau, Zurich

Swiss Federal Institute for Forest, Snow and Landscape Reseach (WSL), Landscape Dynamics, Dendroecology, Birmensdorf

Swiss Federal Institute for Forest, Snow and Landscape Reseach (WSL), Soil Sciences, Birmensdorf

Swiss Federal Institute of Aquatic Science and Technology (Eawag), SURF, Dübendorf

University of Basel, Department of Physics, Basel

University of Basel, Institut für Prähistorische und Naturwissenschaftliche Archäologie (IPNA),

University of Berne, Oeschger Center for Climate Research, Berne

University of Berne, Department of Chemie and Biochemistry, Berne

University of Berne, Climate and Environmental Physics, Berne

University of Berne, Institute of Geography, Berne

University of Berne, Institute of Geology, Berne

University of Fribourg, Department of Geosciences Earth Sciences, Fribourg

University of Geneva, Department of Anthropology and Ecology, Geneva

University of Geneva, Department of Geology and Paleontology, Geneva

University of Lausanne, Institute of Geomatics and Risk Analysis, Lausanne

University of Neuchatel, Department of Geology, Neuchatel

University of Zurich, Institute of Geography, Zurich

University of Zürich, Paläontologisches Institut und Museum, Zurich

University of Zurich, Abteilung Ur- und Frühgeschichte, Zurich

Turkey

Istanbul Technical University, Faculty of Mines, Istanbul

Middle East Technical University, Geological Engineering Department, Ankara

United Kingdom

Durham University, Department of Geography, Durham

University of Bristol, Department of Earth Sciences, Bristol

USA

Columbia University, Lamont Doherty Earth Observatory, New York

VISITORS AT THE LABORATORY

Shavkat Akhmadaliev
Research Center Dresden-Rossendorf, Germany

Javier Santos Arévalo
Centro Nacional de Aceleradores, University of Seville, Spain

Christopher Binz
Kantonsschule Küsnacht, Switzerland

Patrik Caspar
Schweiz. Alpine Mittelschule Davos, Switzerland

Luca Delacrétaz
EPFL, Lausanne, Switzerland

Arnaud Du Pasquier
Lyceum Alpinum Zuoz, Switzerland

Hilde De Clercq
Royal Institute for Cultural Heritage, Brussels, Belgium

Olivier Fässler
Deutsches Gymnasium Biel, Germany

Engin Güzel
Kantonsschule Olten, Switzerland

Michael Hotchkis
Institute for Environmental Research, ANSTO, Lucas Heights, Australia

Daniel Hanf
Research Center Dresden-Rossendorf, Germany

Wan Hong
Korean Institute of Geology, Mining and Materials, Korea

Robert Janovics
ATOMKI, Debrecen, Hungary

Doug Jensen
Idaho National Laboratory, Idaho Falls, USA

Steffen Klare
Research Center Dresden-Rossendorf, Germany

Joon Kon Kim
Korean Institute of Geology, Mining and Materials, Korea

Vladimir Levchenko
Institute for Environmental Research, ANSTO, Lucas Heights, Australia

Bettina Lanfranchi
Lyceum Alpinum Zuoz, Switzerland

Joëlle Linggi
Theresianum, Switzerland

Caroline Münsterer
Institute of Environmental Physics, University of Heidelberg

Frans Munnik
Research Center Dresden-Rossendorf, Germany

Theo Marquardt
Gymnasium Isny, Germany

Alice Motschi
Kantonsschule Olten, Switzerland

Silvana Martin
Dipartimento di Geoscienze, Università degli Studi di Padova, Italy

Isabel Gomez Martinez
Centro Nacional de Aceleradores, University of Sevilla, Spain

John Olson
Idaho National Laboratory, Idaho Falls, USA

Marc Ostermann
Department of Geology, University of Innsbruck, Austria

Ulrike Patt
Institute of Geology and Mineralogy, University of Cologne, Germany

Janet Rethemeyer
Institute of Geology and Mineralogy, University of Cologne, Germany

Cristina Recasens
Department of Geology and Paleontology, University of Geneva, Switzerland

Laszlone Sandor
ATOMKI, Debrecen, Hungary

Peter Schürch
Department of Geography, Durham University, Durham, England

Mark Van Strydonck
Royal Institute for Cultural Heritage, Brussels, Belgium

Axel Weise
Research Center Dresden-Rossendorf, Germany

Matthew G. Watrous
Idaho National Laboratory, Idaho Falls, USA